

# Magneto-Thermoelectric Effects in Co/Pt Layered Systems

Dissertation  
zur Erlangung des Doktorgrades  
an der Fakultät für Mathematik, Informatik und Naturwissenschaften  
Fachbereich Physik  
der Universität Hamburg

vorgelegt von  
**AXEL FRAUEN**  
aus Eckernförde

Hamburg  
2017

Gutachter der Dissertation:	Prof. Dr. Hans Peter Oepen Prof. Dr. Robert Heinrich Blick
Zusammensetzung der Prüfungskommission:	Prof. Dr. Michael Alexander Rübhausen Prof. Dr. Hans Peter Oepen Prof. Dr. Robert Heinrich Blick Prof. Dr. Michael Thorwart Prof. Dr. Andreas Stierle
Vorsitzender der Prüfungskommission:	Prof. Dr. Michael Alexander Rübhausen
Datum der Disputation:	12.01.2018
Vorsitzender des Fach-Promotionsausschusses PHYSIK:	Prof. Dr. Wolfgang Hansen
Leiter des Fachbereichs PHYSIK:	Prof. Dr. Michael Potthoff
Dekan der Fakultät MIN:	Prof. Dr. Heinrich Graener

## Abstract

The magnetoresistance and magneto-thermoelectric effects of Pt/Co/Pt layered systems are investigated. The wire shaped films are prepared by means of photolithography varying the cobalt thickness  $t_{\text{Co}}$  in the range of 0.8 nm to 50 nm. Measurements of the resistivity  $\rho$  and the thermopower (Seebeck coefficient)  $S$  in dependence on external magnetic field and magnetization orientation, respectively, are performed. The thickness dependent evaluation enables to disentangle effects that are superimposed in the measurements and to correct for the shunting influence of the Pt layers on the electrical current and thermovoltage in the Co layer. The latter is essential for a quantitative determination of the genuine magnetization dependent magnitudes of the effects originating in the Co bulk and Co/Pt interfaces.

Beyond reproducing the known results of the anisotropic magnetoresistance (AMR) and anisotropic interface MR (AIMR) effects their thermoelectric analogs, namely, the anisotropic magneto-thermoelectric power (AMTEP) and the interface AMTEP are revealed whereat the latter was firstly reported in literature as part of this thesis. The existence of these effects were anticipated due to the Mott formula which describes the proportionality between the thermopower  $S$  and the electrical conductivity  $\sigma$  ( $= \rho^{-1}$  if scalar) in the form of  $S = C \cdot \sigma^{-1}$  with  $C$  being proportional to the energy derivative of the conductivity at the Fermi energy.

The AMR and AIMR results are adapted regarding the current shunting with an existing correction model, considering the layered sample structure, yielding the genuine effect sizes. For the AMTEP and interface AMTEP another model is developed to determine the pure effect sizes in the thermopower, too. The comparison of the bulk and interface effects reveals a different scaling in the resistivity and thermopower as  $C_{\text{bulk}} \neq C_{\text{interf.}}$ . In consequence to the dependence of  $C$  on the mentioned derivative, this leads to the conclusion that in the regions where the effects originate (bulk and interface, respectively) a different electronic band structure is present.

To validate the integrity of this finding numerous additional investigations are performed, e.g., the consideration of the three dimensional temperature gradient in the sample and its impact (Nernst effects) on the thermoelectric measurements. It is found to be the source of parasitic contributions to the longitudinal thermopower which are successfully eliminated from the measurement data.



## Zusammenfassung

Es werden die Magnetowiderstands- und magnetothermoelektrischen Effekte von Pt/Co/Pt-Schichtsystemen untersucht. Die drahtförmigen Filme werden per Photolithographie hergestellt, wobei die Cobalt-Dicke  $t_{\text{Co}}$  im Bereich von 0.8 nm bis 50 nm variiert wird. Der spezifische Widerstand  $\rho$  und die Thermokraft (Seebeck-Koeffizient)  $S$  wird in Abhängigkeit eines externen Magnetfeldes bzw. der Magnetisierungsorientierung gemessen. Die dickenabhängige Untersuchung erlaubt es, Effekte, die in den Messungen überlagert auftreten, zu trennen und den Kurzschluss-Einfluss der Pt-Schichten auf den elektrischen Strom und die Thermospannung in der Co-Lage zu korrigieren. Letztgenanntes ist unerlässlich für eine quantitative Bestimmung der unverfälschten magnetisierungsabhängigen Größen der Effekte, welche im Co-Volumenfestkörper und den Co/Pt-Grenzflächen ihren Ursprung finden.

Neben der Reproduktion der bekannten Ergebnisse des anisotropen Magnetowiderstandseffekts (AMR) und des anisotropen Grenzflächen-Magnetowiderstandseffekts (AIMR) werden deren thermoelektrischen Gegenstücke, der anisotrope Magneto-Thermokrafteffekt (MTEP) und anisotrope Grenzflächen-Magneto-Thermokrafteffekt (interface AMTEP), aufgedeckt, wobei der letztgenannte erstmalig im Rahmen dieser Arbeit in der Literatur veröffentlicht wurde. Die Existenz besagter Effekte wurde anhand der Mott-Formel erwartet, welche die Proportionalität zwischen Thermokraft  $S$  und der elektrischen Leitfähigkeit  $\sigma$  ( $= \rho^{-1}$  falls skalar) in der Form  $S = C \cdot \sigma^{-1}$  beschreibt.  $C$  ist dabei proportional zur Ableitung der spezifischen Leitfähigkeit nach der Energie an der Fermi-Energie.

Die AMR- und AIMR-Ergebnisse werden bezüglich des Kurzschluss-Einflusses auf den Strom mit einem bestehenden Korrekturmodell, welches das Schichtsystem berücksichtigt, angepasst, was zu den unverfälschten Effektgrößen führt. Für den AMTEP und den Grenzflächen-AMTEP wird ein weiteres Modell entwickelt um auch für die thermoelektrischen Messungen die reinen Effektgrößen zu bestimmen. Der Vergleich der Volumenfestkörper- und Grenzflächeneffekte enthüllt eine unterschiedliche Skalierung in Widerstands- und thermoelektrischen Messungen, da  $C_{\text{bulk}} \neq C_{\text{interf.}}$  beobachtet wird. Wegen der Abhängigkeit von  $C$  von der vorher erwähnten Ableitung führt dies zu dem Schluss, dass in den Entstehungsgebieten (Volumenfestkörper bzw. Grenzflächen) der Effekte eine unterschiedliche elektronische Bandstruktur vorliegt.

Um die Aussagekraft dieses Ergebnisses zu verifizieren, werden zahlreiche zusätzliche Untersuchungen durchgeführt, z. B. die Berücksichtigung des dreidimensionalen Temperaturgradienten in der Probe und dessen Einfluss (Nernst-Effekte) auf die thermoelektrischen Messungen. Es wird festgestellt, dass dieser die Quelle parasitärer Beiträge zur Längs-Thermokraft darstellt, welche erfolgreich von den Messdaten entfernt werden können.



# Contents

1	Introduction	1
2	Theoretical background	3
2.1	Magnetoresistance effects . . . . .	3
2.1.1	Longitudinal magnetoresistance effects . . . . .	3
2.1.2	Transverse magnetoresistance effects . . . . .	5
2.2	Thermoelectricity & magneto-thermoelectric effects . . . . .	6
2.2.1	Mott formula . . . . .	8
2.2.2	Magneto-thermoelectric effects . . . . .	10
3	Experimental details	13
3.1	Pt/Co/Pt sample system . . . . .	13
3.1.1	Deposition of layered film system . . . . .	14
3.1.2	Sample layout and electrical contacting . . . . .	15
3.1.3	Magnetic anisotropy . . . . .	18
3.2	Measurement principles . . . . .	22
3.2.1	Measurement setup . . . . .	23
3.2.2	Measurement scheme . . . . .	23
3.2.3	Temperature calibration . . . . .	25
3.3	Field-dependent measurements . . . . .	28
3.3.1	Field sweep measurements . . . . .	29
3.3.2	Rotation measurements . . . . .	31
3.3.3	Electrical resistivity vs thermopower . . . . .	33
3.3.4	Hall and Nernst effects . . . . .	34
3.4	Supplementary investigations . . . . .	39
3.4.1	Temperature dependence of thermopower . . . . .	40
3.4.2	Dependence of thermopower on temperature difference . . . . .	41
3.4.3	Relation between electrical conductivity and resistivity . . . . .	44
3.4.4	Separation of Nernst contributions from the longitudinal magneto-thermopower . . . . .	45
4	Longitudinal magnetoresistance & magneto-thermoelectric power	51
4.1	Thickness dependence of magnetoresistance effects . . . . .	51
4.1.1	Correction for shunting (MR) . . . . .	53
4.2	Thickness dependence of magneto-thermoelectric effects . . . . .	54
4.2.1	Modeling of magneto-thermoelectric effects . . . . .	55

## Contents

4.2.2	Correction for shunting (MTEP) . . . . .	59
4.2.3	Comparison of shunt-corrected anisotropic MR & MTEP effects . . . . .	61
4.3	Spin-disorder effects in MR & MTEP . . . . .	63
5	Conclusion and outlook	67
	Erratum	71
	Bibliography	73
	Publications	83

# 1 Introduction

In the early 1820s T. J. Seebeck first observed the phenomenon that in a closed circuit of dissimilar metals a current will flow if one of the junctions is heated [1, 2]. In case that this circuit, being exposed to a temperature gradient, is left open a voltage drop, the so-called thermovoltage, can be detected. These and related effects came to be known as thermoelectricity. Some years later, in 1856, W. Thomson discovered a change of the electrical resistivity associated with the magnetization orientation in ferromagnetic 3d metals [3] which was termed anisotropic magnetoresistance (AMR) effect. Today, magnetoresistance is the general term that collectively characterizes all phenomena where the charge carrier transport of a system changes due to the influence of a magnetic field or the magnetization. At nearly the same time of observing the AMR Thomson was also able to show a similar impact of magnetization orientation on the thermodiffusion current or thermovoltage [4], see also Fig. 1.1. This is the anisotropic magnetothermopower (anisotropic MTEP) effect. Further investigations on the MR and MTEP in a variety of metallic systems were performed hand in hand till the early 1920s [5].

After that the MTEP effects in metals played only a minor role and were investigated rather sporadically whereas the MR effects were intensively studied, especially the AMR which had its booming period in the 1960s to 80s [6]. With the advances in preparation techniques yielding thin films with good quality interfaces the age of spintronics began when the giant magnetoresistance (GMR) was found [7]. To some extent the corresponding MTEP measurements were performed in the GMR systems [8].

In 2008 the spin-Seebeck effect was discovered<sup>1</sup> by Uchida *et al.* [9] which led to the birth of spin caloritronics. This field is concerned with the generation, detection, and quantification of spin currents in thin films arising from thermal gradients [10, 11, 12]. It is possible to electrically detect the spin currents via the anomalous Hall [13] (or Nernst [14]) effect or inverse Spin Hall effect due to spin-dependent scattering processes. The Fig. 1.1 illustrates the different connections of spin, heat and charge which define the research topics of spintronics (interplay of charge and spin flow), spin caloritronics (interplay of heat and spin flow) and thermoelectrics (interplay of heat and charge flow) [15]. The anisotropic magnetothermoelectric power (MTEP) effect touches all three areas as it is connected with

---

<sup>1</sup>Later some issues regarding the quantification due to parasitic planar Nernst effects were uncovered.

## 1 Introduction

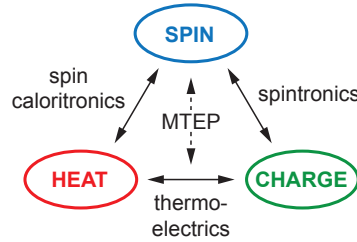


**Figure 1.1:** Connections of spin, heat and charge flow defining the research topics of spintronics (interplay of charge and spin flow), spin caloritronics (interplay of heat and spin flow) and thermoelectrics (interplay of heat and charge flow). The magneto-thermoelectric power (MTEP) effects characterize magnetization-dependent thermodiffusion currents.

the heat generated charge flow under consideration of the magnetization of the sample.

In thin Pt/Co/Pt layered systems which amongst others gained importance in context with the investigations on perpendicular magnetic anisotropy (PMA) [16] interface contributions to the AMR were found by members of the research team of H. P. Oepen in 2011 [17]. This newly discovered effect is called anisotropic interface magnetoresistance (AIMR) [17, 18, 19, 20] and is a consequence of a magnetization dependent scattering probability of the electrons at the interfaces. As there is a connection between the electrical resistivity and the thermopower described by N. F. Mott [21] which in addition was also shown to be valid for MR and MTEP effects [22, 23, 24, 25] the question was raised if and how the AIMR effect would show up in magneto-thermoelectric measurements. Answering this question is the main purpose of this work.

After giving the theoretical background on the performed investigations in Ch. 2 the experimental basics are discussed in the first sections of Ch. 3 including the sample layout and the temperature calibration for the thermoelectric measurements. In Sec. 3.3 the exemplary results of the investigations on the longitudinal and transverse resistivity and thermopower of the Pt/Co/Pt samples in dependence on the magnetization are given. The Sec. 3.4 is concerned with supplementary investigations needed to correctly evaluate the measurement data. Before concluding this work in the last chapter, in Ch. 4 the MR and MTEP results in dependence on the Co thickness are discussed including the presentation of a modeling of the MTEP results to account for shunting effects of the non-ferromagnetic Pt layers.

## 2 Theoretical background

In this chapter the theoretical fundamentals of the investigations and its evaluation performed in the course of this work are presented. Regarding the essentials of the theory of magnetism, be referred to Refs. [26, 27, 28, 29, 30, 31]. If it is convenient some of the theory will be given in direct context with the discussion of the measurements, e.g., the explanation of the magnetic anisotropy. Starting with Sec. 2.1, the major magnetoresistance (MR) effects that occur in the measurements are discussed, including the longitudinal (2.1.1) and transverse (2.1.2) MR effects. The Sec. 2.2 is concerned with some insights on the thermoelectricity whereat the Mott formula (2.2.1) is discussed and, in Sec. 2.2.2, the longitudinal and transverse magneto-thermoelectric (MTEP) effects are explained.

### 2.1 Magnetoresistance effects

This section deals with the dominating magnetoresistance (MR) effects that occur in the Pt/Co/Pt sample systems investigated in the course of this thesis. Generally, they describe the influence of the external magnetic field  $\mathbf{H}$  and the magnetization  $\mathbf{M}$  on the electrical resistivity tensor  $\overleftrightarrow{\rho}$ . According to Ohm's law the tensor connects the electrical field  $\mathbf{E}$  and the electrical current  $\mathbf{j}$  in the following manner [32]

$$\mathbf{E} = \overleftrightarrow{\rho} \cdot \mathbf{j} . \quad (2.1)$$

The effects can be categorized into the ones that affect the diagonal elements of the resistivity tensor (influencing the longitudinal voltage drop along the current direction  $\mathbf{j}$ ) and the ones that alter the off-diagonal elements (influencing the transverse voltage regarding  $\mathbf{j}$ ). For the sake of simplicity a current impressed in the film plane ( $xy$ -plane) along a distinct direction ( $x$ -direction) is assumed (like fulfilled in the experiments) which leaves the longitudinal resistivity  $\rho_x$  and the transverse resistivities  $\rho_y$  and  $\rho_z$  whereby the last mentioned quantity is not experimentally accessible due to the planar sample layout.

#### 2.1.1 Longitudinal magnetoresistance effects

According to Onsager's law [33, 34] the longitudinal MR effects exhibit even functions of the resistivity  $\rho_x$  in dependence on  $\mathbf{M}$  and  $\mathbf{H}$ :  $\rho_x(\mathbf{M}, \mathbf{H}) = \rho_x(-\mathbf{M}, -\mathbf{H})$ .

The probably most famous MR effect in ferromagnetic metals is the anisotropic magnetoresistance (AMR) effect discovered by W. Thomson in 1856 [3, 4]. It was

## 2 Theoretical background

found that the resistivity is maximal<sup>1</sup> when the current and magnetization direction are in parallel ( $\mathbf{j} \parallel \mathbf{M}$ ) and minimal when they are oriented perpendicularly ( $\mathbf{j} \perp \mathbf{M}$ ), so that a possible maximum change of resistivity is given by  $\Delta\rho_{\text{AMR}} = \rho_{\parallel} - \rho_{\perp}$ . The underlying mechanism of the AMR originates from the spin orbit interaction [35, 6, 36, 37]. In a simple picture it is argued that the  $s$ - $d$  scattering probability depends on the relative orientation of magnetization and current direction [35].

In any investigation designated to determine the magnitude of the MR effect it is a good experimental proceeding to not only measure the extreme values but also the angular dependence of the effect. This prevents a distortion of the result for example caused by contributions of additional present effects with different symmetries. For polycrystalline materials like in the case of the used Co/Pt systems the angular dependence is given by

$$\rho(\varphi) = \rho_{\perp} + \Delta\rho_{\text{AMR}} \cdot \cos^2\varphi \quad (2.2)$$

where the angle  $\varphi \angle(\mathbf{M}, \mathbf{j})$  is altered in the sample/substrate plane with  $\rho_{\parallel}$  at  $\varphi = 0^\circ$  and  $\rho_{\perp}$  at  $\varphi = 90^\circ$ .

Normally, the magnitude of the AMR effect is expected to be nearly independent of the thickness of the investigated material [38, 39]. For the same layered Co/Pt systems used in the course of this work, however, it was shown that the interfaces of the individual layers provide an additional AMR contribution of different magnitude than the one of the bulk material which leads to a thickness dependence of the overall detected AMR effect for thin films where a large interface to bulk ratio is present [20].

Another crucial effect regarding this thesis is the anisotropic interface magnetoresistance (AIMR) effect. It was first discovered by Kobs *et al.* in Co/Pt layered systems [17, 40, 19] and subsequently a phenomenological model considering an  $\mathbf{M}$ -dependent electron scattering probability at the interfaces, was developed [20]. In addition, a fully relativistic description of the magneto-transport where the spin-orbit interaction is inherently included could reproduce the experimental findings [18]. As the magnitude of the AIMR is relatively small, it is only detectable for thin films ( $\lesssim 50$  nm) where the fraction of the probe for the MR effects, i.e., the impressed electrical current, at the interfaces is sufficiently large compared to the fraction in the bulk. Since the discovery of the AIMR in Co/Pt it has been found for other material compositions, too [41, 42, 43], pointing to a general behavior in thin layered structures.

The minimum resistivity due to the AIMR effect is present for the magnetization oriented in the plane of the thin film while it is maximal when  $\mathbf{M}$  is parallel to the film/interface normal ( $\rho_{\mathbf{n}}$ ), yielding an effect size of  $\Delta\rho_{\text{AIMR}}$  labeling the difference between these two values. When rotating the magnetization in the plane perpendicular to the current direction where changes of the resistivity due

---

<sup>1</sup>In some materials a negative sign for the AMR effect is found [6].

## 2.1 Magnetoresistance effects

to bulk-like AMR does not occur, i.e., tuning the angle  $\theta \angle(\mathbf{M}, \mathbf{j})$  with  $\rho_{\parallel}$  at  $\theta = 0^\circ$  and  $\rho_{\perp}$  at  $\theta = 90^\circ$ , the angular dependence of the AIMR effect looks like

$$\rho(\theta) = \rho_{\perp} + \Delta\rho_{\text{AIMR}} \cdot \cos^2\theta . \quad (2.3)$$

In the context with the AIMR it is worth mentioning the geometrical size effect (GSE) [44, 45, 46] originating from the texture in polycrystalline ferromagnets. The mechanism is the same like for the AMR effect (crystalline AMR [47]) which leads to varying contributions to the resistivity due to anisotropic scattering depending on how  $\mathbf{M}$  is oriented with respect to the crystalline texture. As the here used Co/Pt systems exhibit an isotropic growth in the film plane but develop an out-of-plane texture, the GSE shows the same functional dependence like the AIMR effect (Eq. 2.3). While  $\Delta\rho_{\text{AIMR}}$  is positive for Co/Pt  $\Delta\rho_{\text{GSE}}$  was determined to be of opposite sign. Furthermore, it was found that (opposed to the thus misleading name) the GSE is a bulk effect not depending on thickness as expected as it originates from the texture. In consequence, the GSE contributes as a constant negative offset to the AIMR effect in the measurements (see Sec. 4.1).

The last effect to be mentioned explicitly in this section is the magnon MR, also known as spin-disorder MR (SMR) effect. It describes the decrease of the resistivity  $\rho$  of a ferromagnetic system due to an increase of the magnetization over the saturation value at a certain temperature with an applied magnetic field  $\mathbf{H}$  (disregarding single spin excitation). It can be understood looking at the impact of the field on the magnon spectrum. The magnetic field reduces the number of magnons, i.e., the quasiparticles of the spin waves, which leads to a reduced resistivity as the number of scattering events of magnons and electrons decreases. It was found that the SMR effect exhibits a linear change of  $\rho$  in dependence on  $\mathbf{H}$  independent of orientation of the field in a wide range of temperature and high field strengths up to 40 T [48, 49].

### 2.1.2 Transverse magnetoresistance effects

According to Onsager's law [33, 34] the transverse MR effects exhibit uneven functions of the resistivity  $\rho_y$  in dependence on  $\mathbf{M}$  and  $\mathbf{H}$ :  $\rho_y(\mathbf{M}, \mathbf{H}) = -\rho_y(-\mathbf{M}, -\mathbf{H})$ .

The two effects of concern within this work are the Hall effects. The normal or ordinary Hall effect (OHE) [50] characterizes the influence of a perpendicular magnetic field  $H_z$  on the transverse voltage  $U_y$  when a current is flowing in  $x$ -direction which can be written as

$$U_y = R_0 \mu_0 H_z \frac{I_x}{t} \quad (2.4)$$

where  $R_0$  is the material-dependent normal Hall constant. The OHE scales inversely with the thickness  $t$  of the investigated specimen. The origin of the effect

## 2 Theoretical background

is the Lorentz force. In ferromagnets another contribution arises in  $U_y$  depending on the perpendicular magnetization orientation  $M_z$  described as extraordinary or anomalous Hall effect (AHE) [13]. It is caused by the spin orbit interaction [51, 52] and exhibits a similar functional dependence like the ordinary effect:

$$U_y = R_S \mu_0 M_z \frac{I_x}{t} \quad (2.5)$$

with  $R_S$  being the anomalous Hall constant.

### 2.2 Thermoelectricity & magneto-thermoelectric effects

When the investigated system is exposed to a temperature gradient and contacted by other materials like in the case of the magneto-thermoelectric measurements conducted in context with this work, Ohm's law has to be extended as follows

$$\mathbf{E} = \overleftarrow{\rho}(\mathbf{M}) \cdot \mathbf{j} + \overleftarrow{S}(\mathbf{M}) \cdot \nabla T - \frac{1}{e} \cdot \nabla \mu . \quad (2.6)$$

While the first term is zero in the MTEP investigations as no current is applied the temperature gradient  $\nabla T$  introduces a contribution to the generated electric field proportional to the thermopower  $S$  (Seebeck coefficient) of the materials. The last term characterizes the occurring field due to the gradient of the chemical potential  $\mu$  at the material transitions.

First, the thermopower shall be discussed. It describes the generation of an electric field due to the phenomenon of thermodiffusion of charge carriers. For metals this is depicted in the sketch given in Fig. 2.1(a). In the case of an existing temperature gradient along a wire the electrons moving from the hot to the cold wire end possess a higher velocity everywhere in the wire compared to the ones moving in opposite direction. The resulting directed movement creates an electric field along the wire which in turn disrupts the net thermodiffusion current, meaning that after this equilibrium state is reached the number of moving electrons from hot to cold end and vice versa is the same. This is valid for the wire not being implemented in a closed circuit.

However, experimentally the field is not directly detectable in the form of a measurement of a thermovoltage drop  $dU = -S dT$  along an isolated wire. Only if the wire is brought into contact with another material, shown in Fig. 2.1(b) as an open-circuit diagram, it is possible to measure a voltage which then represents the difference of the thermovoltages (relative thermovoltage) of the materials. In

## 2.2 Thermoelectricity & magneto-thermoelectric effects

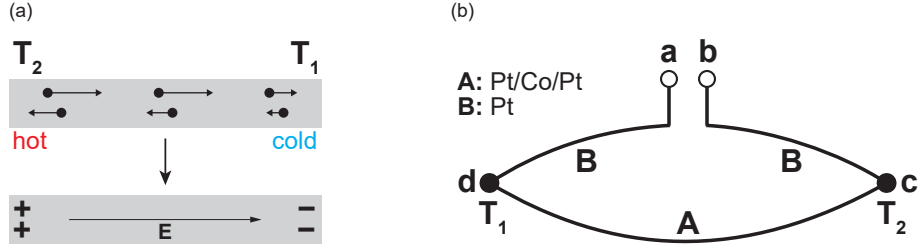


**Figure 2.1:** (a) Sketch of a metal wire with an applied temperature gradient depicting the thermodiffusion of electrons. The electrons moving from hot to cold wire end possess a higher velocity everywhere in the wire compared to the ones moving in opposite direction. The resulting directed movement creates an electric field along the wire. This field disrupts the thermodiffusion current (open circuit). (b) Diagram of an open circuit composed of material A and B. The two material transition are at different temperatures  $T_1$  and  $T_2$  for thermoelectric measurements. The Pt/Co/Pt wires (A) investigated in the course of this work are contacted by Pt leads (B) on both ends as indicated.

the following this is explained for the circuit given in Fig. 2.1(b) [1, 53]:

$$\begin{aligned}
 \Delta U_{\text{th}} &= U_b - U_a = (U_b - U_c) + (U_c - U_d) + (U_d - U_a) \\
 &= \int_c^b dU + \int_d^c dU + \int_a^d dU \\
 &= - \int_c^b S_B dT - \int_d^c S_A dT - \int_a^d S_B dT \\
 &= - \int_c^d S_B dT - \int_d^c S_A dT \\
 &= \int_{T_1}^{T_2} (S_B - S_A) dT
 \end{aligned} \tag{2.7}$$

The material A with the thermopower  $S_A$  and the contacting material B with  $S_B$  each contribute a thermovoltage, see first line of Eq. 2.7, as  $T_1 \neq T_2$  is valid. The last line of the equation reveals that the measured thermovoltage  $\Delta U_{\text{th}}$  (between points a and b) is determined by the different thermopowers of the materials. Moreover, it is clear that the integral becomes zero, i.e., no voltage drop, if the temperatures are the same or if the circuit is composed of only one material meaning that  $S_A = S_B$ .

In consequence of Eq. 2.7 the relative thermopower can be calculated from the measured  $\Delta U_{\text{th}}$  via division by the temperature difference  $\Delta T = T_2 - T_1$ . As the Seebeck coefficient generally is temperature-dependent it is defined for the limiting case of  $\Delta T \rightarrow 0$  to be valid for an arbitrary temperature difference [54, 1, 55]:

$$S_{\text{meas}} = \lim_{\Delta T \rightarrow 0} \left( \frac{-\Delta U_{\text{th}}}{\Delta T} \right) = S_A - S_B. \tag{2.8}$$

Note the (unusual) negative sign of the expression. For the investigations presented in this thesis the circuit setup was initially arranged in a way to measure a positive

## 2 Theoretical background

thermovoltage. To meet the convention in literature on the sign of thermopowers the minus was added to achieve the correct result.

The third term of Eq. 2.6 describes the generation of a field due to  $\nabla\mu$  at the material transitions as already stated above. The gradient is present because the chemical potential  $\mu$  differs for material A and B yielding a diffusion of electrons and consequently a contact voltage  $U_c = -1/e \cdot (\mu_B - \mu_A)$  similar to the description of the thermovoltage. However, these voltage contributions are fully compensated along the circuit which, especially, is also valid in the presence of a temperature difference between the material transitions. It is argued that  $\mu$  indeed locally varies in the (homogenous) contacting materials due to the temperature dependence on the distance to the heated transition but is equal at the circuit ends which are of the same material at the same temperature [56]. Hence, the thermovoltage is only caused by the thermodiffusion.

Supposing a layered sample system the Eq. 2.8 can generally be rewritten [2] to describe the shunting effects in the sample composed of materials A and B:

$$S = S_{A/B} - S_B = \frac{\sum_i S_i \sigma_i}{\sum_i \sigma_i} - S_B \quad (2.9)$$

with  $i = (A, B)$  and the electrical conductivities  $\sigma_i$ . The samples investigated in the course of this work are composed of Co and Pt layers. Minding Kirchhoff's first law  $I = I_A + I_B$  assuming the material layers as conductors connected in parallel and with  $I = U/R = S\Delta T/R$  the dimensions of the single layers are introduced in the above equation by writing the resistance for each layer as  $R = \sigma^{-1} \cdot l/(w \cdot t)$  with the length, width and thickness of the layers (for details see Ref. [57]). In case of the investigated wire-shaped Co/Pt samples the lateral dimensions are the same for all layers so that only the thickness  $t$  will occur as parameter:

$$S = \frac{\sum_i S_i \sigma_i t_i}{\sum_i \sigma_i t_i} - S_{Pt} \quad (2.10)$$

with  $i = (Co, Pt)$ . More information on the consideration of the layered structure are given in Sec. 4.2.1.

### 2.2.1 Mott formula

As stated above (Eq. 2.6) both an electric current and a temperature gradient in a system are proportionally connected to a corresponding electric field by the resistivity  $\rho$  (or conductivity  $\sigma$ ) and thermopower  $S$ , respectively. The knowledge that these two parameters are not isolated but connected with each other was reached by N. F. Mott [21, 58]. Based on the Boltzmann equation in relaxation time approximation with the assumption of non-interacting electrons that scatter at randomly distributed defects of the crystal lattice [59, 1] Mott was able to derive a formula for the Seebeck coefficient. For a temperature gradient  $\partial T/\partial x$

## 2.2 Thermoelectricity & magneto-thermoelectric effects

along the (long)  $x$ -axis of a rod he obtained the following relation between *absolute* thermopower (Seebeck coefficient)  $S$  and *differential* conductivity  $\sigma^*$

$$\begin{aligned} S &= \frac{\pi^2 k_B^2 T}{3 e} \left[ \frac{\partial \ln \sigma^*(E)}{\partial E} \right]_{E=\xi} \\ &= \frac{\pi^2 k_B^2 T}{3 e} \left[ \frac{1}{\sigma^*(E)} \frac{\partial \sigma^*(E)}{\partial E} \right]_{E=\xi} \end{aligned} \quad (2.11)$$

which came to be known as Mott's formula ( $\xi$ : chemical potential). The second expression follows from the identity for the derivative of the logarithm. The *differential* conductivity  $\sigma^*$  is defined as

$$\sigma^*(E) = \frac{2e^2}{\hbar^2} \int \left( \frac{\partial E}{\partial k_x} \right)^2 \tau(\mathbf{k}) \frac{dA_E}{|\nabla E|} \quad (2.12)$$

where  $\tau$  is the relaxation time and  $dA_E$  represents the integration over the energy surface  $E$  in  $\mathbf{k}$ -space. The electrical conductivity  $\sigma$  is

$$\sigma = \int \sigma^*(E) \frac{\partial f_0}{\partial E} dE \quad , \quad (2.13)$$

where  $f_0$  is the Fermi distribution function in thermal equilibrium without electric field.

In many experimental investigations a linear relationship between  $S$  and  $\sigma$  is found [60, 1, 61, 62, 63]. Using Mott's formula (Eq. 2.11) this means that

$$\frac{\sigma}{\sigma^*(E)|_{E=\xi}} \left[ \frac{\partial \sigma^*(E)}{\partial E} \right]_{E=\xi} = \text{const.} \quad (2.14)$$

This (obviously general) finding can be understood in the limit of low temperatures ( $T \ll T_F$ ), where the chemical potential equals the Fermi energy  $\xi \approx E_F$  and  $\frac{\partial f_0}{\partial E} = -\delta(E - E_F)$  is valid in a good approximation. Hence,  $\sigma^*(E)|_{E=\xi=E_F} = \sigma$  is obtained from Eq. 2.13 and from Eq. 2.14 it follows:

$$\left[ \frac{\partial \sigma^*(E)}{\partial E} \right]_{E=E_F} = \text{const.} \quad (2.15)$$

The latter approximation ( $\sigma^*(E)|_{E=\xi=E_F} = \sigma$ ) is the reasoning for the frequently used (though questionable) expression of the Mott formula [21, 64, 65, 1]:

$$S = \frac{\pi^2 k_B^2 T}{3 e \sigma} \left[ \frac{\partial \sigma(E)}{\partial E} \right]_{E=E_F} \quad (2.16)$$

## 2 Theoretical background

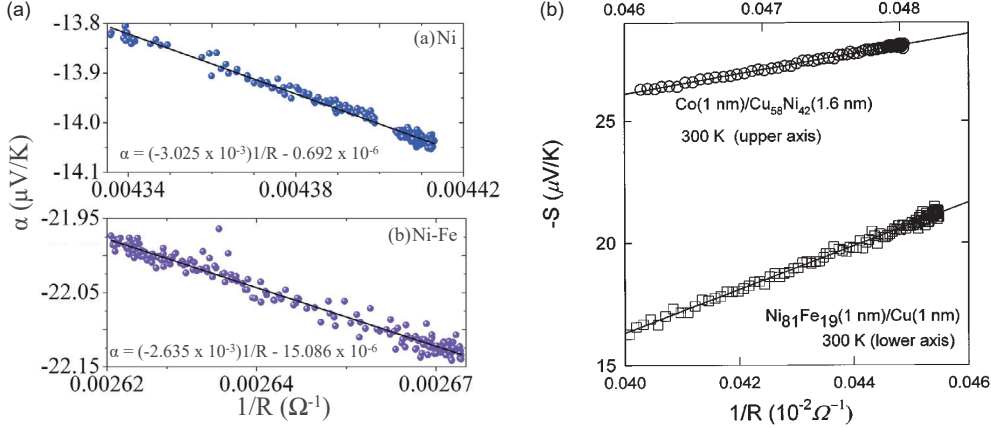


**Figure 2.2:** (a) From Ref. [66]. Thermopower  $S$  (plot:  $\alpha$ ) in dependence on the inverse resistance  $1/R$  visualizing the planar Nernst effect (PNE) vs planar Hall effect (PHE) (i.e., impact of AMTEP and AMR, respectively, in transverse voltage) for Ni and Ni-Fe films. (b) From Ref. [8].  $S$  over  $1/R$  for Permalloy/copper and Co/Cu-Ni multilayers representing the impact of the giant MR (GMR) and its thermoelectric analog.

Sometimes this expression is given in terms of the resistivity, e.g., Ref. [66]. If in Eq. 2.11 the conductivity is substituted by  $\sigma = \rho^{-1}$ , valid for scalars (see also Sec. 3.4.3), and minding  $\partial \ln x / \partial x = -\partial \ln x^{-1} / \partial x$  this yields

$$S \propto -\frac{1}{\rho} \left[ \frac{\partial \rho(E)}{\partial E} \right]_{E=E_F} . \quad (2.17)$$

Starting instead from Eq. 2.16, the following expression is obtained:

$$S \propto \rho \left[ \frac{\partial \sigma(E)}{\partial E} \right]_{E=E_F} . \quad (2.18)$$

### 2.2.2 Magneto-thermoelectric effects

In experiments the validity of the Mott formula (Eq. 2.16) has been numerously demonstrated, see Sec. 2.2.1, even for ferromagnetic systems where magnetoresistance (MR) and magneto-thermoelectric power (MTEP) effects are present. In particular, in case of the AMR [24, 66, 67], magnon MR [22, 68, 67], giant MR (GMR) [23, 69, 8, 70], tunneling MR (TMR) [25], and their corresponding magneto-thermoelectric equivalents, linear dependencies of the Seebeck coefficient  $S$  on the inverse electrical conductivity  $\sigma^{-1}(\mathbf{M})$  are found with the magnetization  $\mathbf{M}$  as an implicit variable. This implies for the Mott formula to be written as

$$S(\mathbf{M}) = \frac{\pi^2 k_B^2 T}{3 e \sigma(\mathbf{M})} \left[ \frac{\partial \sigma(E, \mathbf{M})}{\partial E} \right]_{E=E_F} . \quad (2.19)$$

## 2.2 Thermoelectricity & magneto-thermoelectric effects

Note that the notation of the above expression in terms of the resistivity  $\rho$  (see Eqs. 2.17 & 2.18) or resistance  $R$  qualitatively has the same outcome. Exemplary, the results for two investigations published in literature are presented. For the impact of the AMR and anisotropic MTEP (AMTEP) effects in different systems the linear  $S(1/R)$  curves are given in Fig. 2.2(a) while a plot for the GMR and its thermoelectric analog in the same representation is displayed in (b). The linear functional dependence of each of the depicted curves reveals that the derivative in Eq. 2.19 is constant for the single measurements. For the transverse conductivity/thermopower depending on  $\mathbf{M}$  due to the anomalous Hall and Nernst effect, respectively, a similar behavior was found [71, 72, 73].

Obviously, the important MTEP effects regarding this thesis are the analogs to the MR effects discussed in Sec. 2.1. The AMTEP was more or less simultaneously discovered with the AMR and described by W. Thomson [4] in 1856. The in-plane magnetization dependence of the thermopower  $S$  due to the AMTEP effect can be written as

$$S(\varphi) = S_{\perp} + \Delta S_{\text{AMTEP}} \cdot \cos^2 \varphi \quad (2.20)$$

with the definition of the angle  $\varphi$  being the same as in the case of the AMR while replacing the current direction with the direction of the temperature gradient. Another longitudinal MTEP effect is the thermoelectric counterpart [74, 8] to the spin-disorder MR (SMR) which will be termed spin-disorder MTEP (SMTEP) in this work. The main transverse MTEP effects concerning this thesis are the field-dependent ordinary Nernst effect (ONE)

$$\mathbf{E}_{\text{ONE}} = -N_0 \mu_0 \mathbf{H} \times \nabla T \quad (2.21)$$

and the magnetization-dependent anomalous Nernst effect (ANE)

$$\mathbf{E}_{\text{ANE}} = -N_S \mu_0 \mathbf{M} \times \nabla T \quad (2.22)$$

with  $N_0$  and  $N_S$  as material-dependent Nernst coefficients [14]. They show the same characteristics like the OHE and AHE (2.1.2), respectively, but are experimentally more challenging to quantify. While the Hall effects are linearly dependent on the impressed current which is the same within an investigated sample the Nernst effects scale with the temperature gradient  $\nabla T$  which naturally is harder to determine or control in the measurements than simply applying an electric current.



## 3 Experimental details

This chapter deals with the experimental essentials of this work. In the first section (3.1) the investigated Pt/Co/Pt layered system is presented, including the deposition by means of sputter techniques (3.1.1), the sample layout and electrical contacting for the magnetoresistance (MR) and magneto-thermoelectric power (MTEP) measurements (3.1.2), and the brief summary of structural and magnetic properties focusing on the magnetic anisotropy of the film system (3.1.3).

Thereafter (Sec. 3.2) the measuring principles are explained by introducing the superconducting magnet setup which provides the external magnetic field (3.2.1) followed by the definition of the main measurement geometries for the MR and MTEP investigations (3.2.2). The Section 3.2.3 deals with the temperature calibration for the samples necessary to quantify the results of the MTEP measurements.

The following part, Section 3.3, is concerned with the presentation of exemplary results of the conducted longitudinal MR and MTEP experiments. This covers the field-dependent (field sweeps: Sec. 3.3.1) and angle-dependent (rotations: Sec. 3.3.2) investigations while for the latter a preliminary comparison of MR and MTEP effects is given in Sec. 3.3.3. The qualitative nature of the transverse Hall and Nernst effects, including the additional information they can provide on the investigated samples, are discussed thereafter (3.3.4).

In the last section of this chapter (3.4) the properties of the samples which are important to correctly interpret the results from the measurements are presented in more detail. The Sec. 3.4.1 gives a brief insight on how the base temperature influences the thermovoltage for the investigated samples, followed by the focus on the dependence of the thermopower on the present temperature difference along the Co/Pt wires (3.4.2). Furthermore, it is investigated if the tensorial properties of the electrical resistivity/conductivity are of importance for the utilized sample system (3.4.3). In Sec. 3.4.4 the very important identification and elimination of occurring parasitic effects in the magneto-thermoelectric measurements are discussed, as without this the correct quantification of MTEP effects cannot be accomplished.

### 3.1 Pt/Co/Pt sample system

In the following the preparation (3.1.1) and the layout including the electrical contacting (3.1.2) of the investigated Pt/Co/Pt samples are described. Further-

### 3 Experimental details

more the structural and magnetic properties of the film system are presented, see Sec. 3.1.3.

#### 3.1.1 Deposition of layered film system

The standard samples discussed in this thesis consist of a Pt/Co/Pt layered film system grown on a glass substrate. While the platinum layers are of a constant thickness, namely 5 nm for the seed layer and 3 nm for the cap layer, the ferromagnetic cobalt layer thickness varies from 0.8 nm to 50 nm (see Fig. 3.1).

To meet the substrate requirements for the preparation and the resistance and thermoelectric measurements glass is the material of choice. It fulfills the criteria of being electrically insulating (see Sec. 3.1.2), having a smooth surface for proper film growth, and having a relatively low thermal conductivity [75] in order to achieve a laterally widespread thermal gradient within the metallic film for the thermoelectric measurements. The used polished borosilicate glass is a commercial cover slip for a microscope slide manufactured by *Schott AG, Germany*. The dimensions of the glass slip are 18 mm  $\times$  18 mm  $\times$  0.16 mm, which allows the simultaneous preparation of four wire samples before cutting the substrate down to a lateral size of roughly 6 mm  $\times$  6 mm after the preparation to fit the used chip carrier. The root mean square (RMS) roughness of the glass surface was determined by means of atomic force microscopy to be 0.2 nm.

Before the deposition of the ferromagnetic film system in the shape of the desired sample wire (see Sec. 3.1.2) in a first step a mask of a positive photoresist is created on top of the substrate by means of UV lithography with a laser direct writing system<sup>1</sup>. Subsequently, the Pt/Co/Pt layers are grown on the glass in a UHV sputter chamber. As this chamber has been a core element of our working group for many years this thesis will not provide a thorough discussion of its assembly, mode of operation, etc. More details can be found in older works like Refs. [76, 77, 78, 40, 79]. The film deposition is performed at room temperature and a base pressure in the chamber of  $<2 \times 10^{-9}$  mbar. The first 4 nm of the Pt seed layer are grown via electron-cyclotron resonance (ECR) at a working pressure of the argon gas of  $5 \times 10^{-4}$  mbar with a rate of  $0.3 \text{ nm s}^{-1}$ . The main purpose of using the ECR technique with its relatively high mobility of sputtered atoms is to achieve a Pt(111) texture in crystalline growth. The rest of the seed layer, as well as the Co layer (growth rate of  $0.028 \text{ nm s}^{-1}$ ) and the Pt cap layer (growth rate of  $0.058 \text{ nm s}^{-1}$ ), serving as protection of the Co against oxidation and providing a second Co/Pt interface, are then applied by the use of direct current magnetron sputtering. Compared to the ECR, with magnetron sputtering the atoms are deposited at a lower energy which leads to less interdiffusion at the Pt/Co interfaces and hence to a higher perpendicular magnetic anisotropy of the films. For both the

---

<sup>1</sup>The work concerning the lithography was conducted by staff members of the working group of Prof. Dr. K. Nielsch, INF, Hamburg, Germany.

### 3.1 Pt/Co/Pt sample system

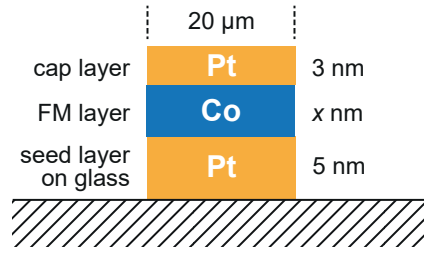


**Figure 3.1:** Schematic cross section of the Pt/Co/Pt layered system grown on a glass substrate in shape of a  $510\ \mu\text{m} \times 20\ \mu\text{m}$  wire by means of UV lithography (3.1.2). The seed layer is composed of 4 nm electron-cyclotron resonance (ECR) deposited Pt and 1 nm DC magnetron sputtered Pt. The ferromagnetic layer is magnetron sputtered Co with a variable thickness of  $t_{\text{Co}} = 0.8\ \text{nm}$  to 50 nm. As cap layer 3 nm of magnetron sputtered Pt are used.

Pt and the Co the Ar working pressure was  $3.4 \times 10^{-3}$  mbar with an ion current at the sputter target of 30 mA and 50 mA, respectively. Simultaneously to the creation of the main sample, the same layered system was deposited as a plain film on several other substrates (Si,  $\text{SiO}_2$ ,  $\text{Si}_3\text{N}_4$ , glass) as well as in the shape of a wire ( $0.5\ \text{mm} \times 6\ \text{mm}$ ; see Sec. 5.2.3 in Ref. [40]) on  $\text{Si}_3\text{N}_4$  to serve as reference samples for possible additional investigations and error checking.

After the beforehand described process the photomask is removed from the sample and a second mask defining the shape of the contacting structure including thermometers and heating wires (see Sec. 3.1.2) is applied. Then a Pt layer of 60 nm is deposited by means of ECR sputtering. On the one hand, this technique allows for a precise control of the thickness to achieve a similar electrical resistance and shape/volume of the wire thermometers and heating wires (see Sec. 3.1.2) for different samples. Especially in the case of the heating wires, this is of importance to obtain a comparable heating behavior for the same applied heating power (3.2.3). On the other hand, the ECR technique provides a relatively high adhesion of the sputtered Pt film on the glass substrate which is advantageous regarding the wire bonding of the contacting pads (see Sec. 3.1.2). If instead a simple sputter coater was used for creating the Pt, an underlying adhesion layer like Ti or Cr would be necessary to prevent a tear-off during bonding. However, as the contacting structure also serves as reference material for the thermoelectric measurements (see Sec. 3.1.2 and 3.3) it is preferable to use plain Pt to preserve the easiest possible comparability of the Seebeck coefficient to literature values.

#### 3.1.2 Sample layout and electrical contacting

The layout of the completed sample is exemplary depicted as microscope photograph in Fig. 3.2. The vertically oriented Pt (5 nm)/Co ( $t_{\text{Co}}$ )/Pt (3 nm) wire is located in the center and is colored implying the temperature gradient dur-

### 3 Experimental details

ing thermoelectric measurements to delimit its boundaries in the picture. The wire measures  $510\ \mu\text{m} \times 20\ \mu\text{m}$  whereat it is important for the wire to possess a certain length to obtain a sufficiently high and for different samples simultaneously minimal varying temperature difference between the hot and cold end in the thermoelectric measurements. Of course, a defined and fixed wire geometry knowing the length  $l$ , the width  $w$ , and the thickness  $t$  should be used to be able to calculate and compare the specific quantities like for example the electrical resistivity

$$\rho_x = R_x \cdot \frac{w \cdot t}{l} \quad (3.1)$$

between samples. At half of the length of the wire there is a small horizontal Pt/Co/Pt wire for measurements of the transverse voltage.

The rest of the depicted sample structure consists of Pt with a thickness of 60 nm providing the pads (numbered in the picture) for external electrical contacting, the wire/resistance thermometers at the ends of the Co/Pt wire, as well as the heating wires. All of the mentioned features are needed in the course of the later performed measurements with the exception of one of the heaters serving as a redundancy for possible manufacturing faults of the sample.

For the external electrical contacting and the mounting to the manipulator of the used magnet (see 3.2.1) the sample on the glass substrate is glued to a chip carrier. The pads of the sample are then connected by means of wire bonding with Al wires to the pads of the chip carrier. A photograph of a chip carrier with an installed sample is shown in Fig. 3.2(b).

The pads 3 and 4 (9 and 10) are used to impress a current  $I_h$  in the heating wire on the top (bottom) and to measure the voltage drop  $U_h$  to be able to calculate the heating power  $P_h = U_h \cdot I_h$ . This is done without the use of a four-point probe measurement as the relatively large pads, and the short and wide leads connecting the heating wire only add a negligible error/offset.

During the temperature calibration of the sample (for details see 3.2.3), needed for the thermoelectric investigations, the electrical resistance of the wire thermometers is measured with a four-point probe method. For this a non-invasive current is impressed and the voltage drop is recorded via the pads 1, 2, 5, and 6 (8, 9, 11, and 12) in the upper (lower) thermometer. As example for one of the thermometers the circuit diagram is shown in the bottom of Fig. 3.2.

When performing the MTEP investigations the thermovoltage  $U_{th}$  along the Co/Pt wire is determined between the pads 1 and 12 (and/or pads 6 and 7) while a heating power  $P_h$  is applied. For the MR investigations ( $P_h = 0\ \text{mW}$ ) a constant, non-invasive current of 0.2 mA is impressed on the one side of the wire (pads 1 or 2 to 11 or 12) and the voltage is measured on the other side (5 or 6 to 7 or 8) and vice versa. If the current and voltage leads were connected on the same side, the thermometer wire would distort the determination of the resistance of the Co/Pt wire. The devices utilized for both the MR and MTEP measurements are a *Keithley 6221* current source and a *Keithley 2182A* nanovoltmeter.

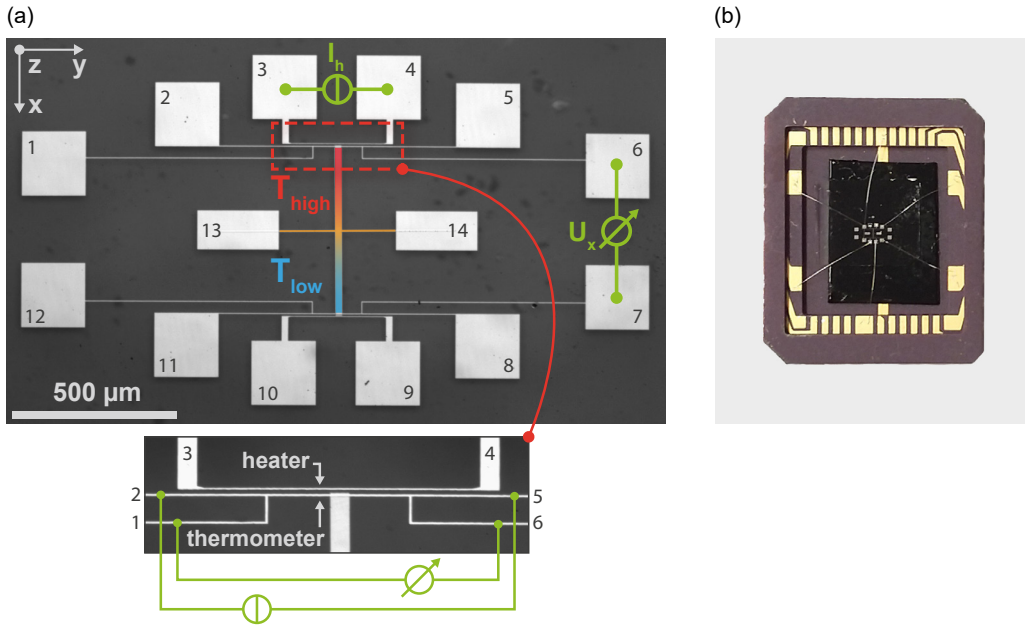


**Figure 3.2:** (a) Microscope photograph of the sample layout. For the MR measurements the voltage drop along the vertically oriented Co/Pt wire is measured, e.g., via contacts 6, 7 for a constant current applied to the Pt pads 1, 12. For the MTEP measurements a temperature gradient along the Co/Pt wire is generated by driving a current through the Pt heater via contacts 3, 4. The resulting thermovoltage  $U_{th}$  is measured via pads 6, 7 (or 1, 12). The upper heater and resistance thermometer including the circuit diagram for the temperature calibration are seen in the zoom in the lower panel. (b) Photograph of the sample on the glass substrate glued into the chip carrier. The electrical contacting is realized by means of Al wire bonding.

The pads 13 and 14 are intended for the measurements of Nernst (MTEP) or Hall (MR) effects, respectively.

To check for an undesired creeping current in the thermoelectric measurements between the heating wire and the rest of the structure the resistance between the two mentioned elements was measured. As the result was higher than  $1\text{ G}\Omega$  it is safe to say that the heating current has no direct influence regarding the determination of the thermovoltage.

Note that the MR investigations described above are for the use of a fixed current which is the conventional (and easy) procedure. As the tensorial properties of resistivity and conductivity may be of importance regarding the Mott formula (Sec. 2.2.1) the MR measurements were also performed by using a fixed voltage, see Sec. 3.4.3. It was found that there is no measurable difference between the both mentioned methods for the used Co/Pt systems.

While all the main measurements presented in this thesis were performed using the above described layout a new layout was developed for ongoing and future

### 3 Experimental details

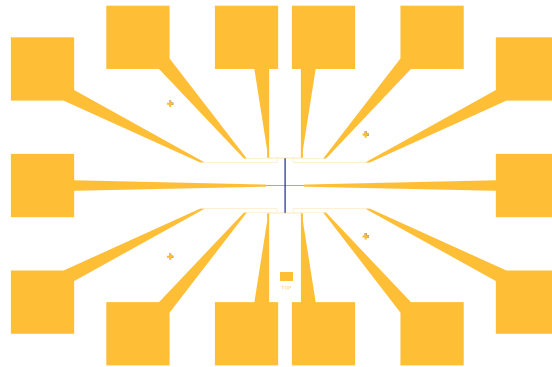


**Figure 3.3:** Sketch of a new sample layout for ongoing and future investigations. The dimensions of the Co/Pt wire and thermometers are the same as in Fig. 3.2. Compared to the old layout the Pt pads and, consequently, the transitions from the platinum to the Al bonding wires are in further distance to the heating source to prevent undesired contributions to the thermovoltage in the MTEP measurements. Apart from the depicted one, additional contacting structures are available, e.g., with multiple thermometers along the sample wire.

investigations, see Fig. 3.3. As the dimensions of the core elements like the Co/Pt wire, the thermometers and the heating wires are not changed, the focus lies on the outer contacting structure which features larger pads located at higher distance to the center area. First, this serves a practical purpose because in the course of some measurements it is necessary to change the wire bonding of the sample which partially leads to a reduction of the pad area when the bond is removed. In an extreme case this may render the sample useless but can be prevented by the use of much larger pads like in the new layout. Second, and more importantly regarding the results of the thermoelectric investigations, the Pt pads and, consequently, the transitions from the Pt pads to the Al bonding wires are at further distance to the heating source. In this way it can be avoided that the Pt/Al transitions heat up to a different extent depending on their position (as approx. no heating at all) which would cause an additional undesired contribution to the measured thermovoltage as sometimes detected, see Fig. 3.9 in Sec. 3.2.3.

Apart from the new layout shown in Fig. 3.3 some other contacting structures were designed, for example with multiple wire thermometers along the Co/Pt wire to determine the longitudinal temperature profile of the sample (not shown).

#### 3.1.3 Magnetic anisotropy

In this section the magnetic and structural properties of used the Pt/Co/Pt sample system are presented. This especially serves the purpose to check for the expected film growth in comparison to other works where the same deposition techniques were used. It was found that the Co/Pt films are of polycrystalline

### 3.1 Pt/Co/Pt sample system

nature with, generally, a *fcc*(111) out-of-plane texture which labels a random distribution of the crystal grain orientations in the film plane but a net orientation of the hexagonal *c*-axis parallel to the film normal [40, 79]. The interfaces between Co and Pt exhibit a rather distinguished interdiffusion zone of two to three atomic monolayers [40, 79].

Due to the urge of energy minimization the overall magnetic anisotropy determines the direction of spontaneous magnetization  $\mathbf{M}$  and thus also influences the behavior regarding the reversal of  $\mathbf{M}$  with the external field  $\mathbf{H}$ . The dominating contributions to the anisotropy constant  $K$  for the here used film systems are the shape anisotropy  $K_{\text{shape}}$ , the magnetocrystalline volume anisotropy  $K_{\text{mca},V}$  and the magnetocrystalline surface anisotropy  $K_{\text{mca},S}$ . The constant  $K_{\text{shape}}$  characterizes the maximum  $\mathbf{M}$ -dependent difference in stray field energy of the film and is  $K_{\text{shape}} = -\frac{\mu_0}{2}M_S^2 = -1.23 \text{ MJ/m}^3$  with the saturation magnetization of  $M_S = 1.4 \text{ MA/m}$  for Co [80], favoring an in-plane magnetization of the thin system. The magnetocrystalline volume anisotropy term describes the dependence of the energy caused by the spin-orbit coupling regarding the magnetization orientation relative to the crystal lattice. In the case of the hexagonal Co crystal the energy is only depending on the orientation of  $\mathbf{M}$  in respect to the *c*-axis, i.e., the easy axis of magnetization, and therefore exhibits a uniaxial anisotropy with a preferred perpendicular (out-of-plane) magnetization due to the texture of the films investigated in the course of this work. The energy density of the magnetocrystalline volume anisotropy can be represented as a power series expansion whereby for Co normally only the first and second order terms  $K_{1V}$  and  $K_{2V}$  are of significant impact [27], however, being of smaller magnitude than the shape anisotropy. The third mentioned contribution, the surface anisotropy, is a consequence of the spin-orbit coupling and the symmetry breaking of the crystal at the interfaces [81].  $K_{\text{mca},S}$  also favors the perpendicular orientation of the magnetization and can overcome  $K_{\text{shape}}$  for thin Co layer thicknesses, see last term of Eq. 3.3.

In summary, the interplay of the presented anisotropy contributions for the Co/Pt samples will lead to two different outcomes, namely, an easy axis of magnetization perpendicular to the sample plane or an easy plane (with no preferred direction) of  $\mathbf{M}$ , depending on the Co volume to Co/Pt interface ratio, i.e., depending on the Co thickness  $t_{\text{Co}}$ .

Experimentally, for each sample the superposition of the different anisotropy constants can be determined and, subsequently, disentangled by evaluating the thickness dependence, as it contains information on the relative impact of the single contributions. This is done by looking at the hard axis magnetization reversal behavior where a coherent rotation of  $\mathbf{M}$  with field can be assumed. In the case of the only investigated sample with perpendicular magnetic anisotropy ( $t_{\text{Co}} = 0.8 \text{ nm}$ ) the anisotropy was extracted from the in-plane field sweep measurements (3.3.1). Further details of the used method are not discussed here and can be found in Ref. [82]. For the samples with an easy plane of magnetization it is convenient

### 3 Experimental details

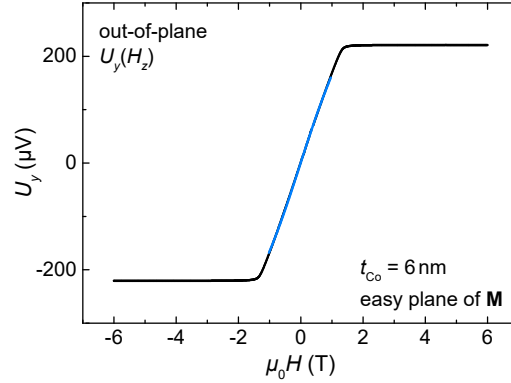


**Figure 3.4:** Transverse voltage  $U_y$  depending on the perpendicular field strength  $\mu_0 H$  for a sample with  $t_{\text{Co}} = 6$  nm and an easy plane of magnetization. The plot, representing a hard axis reversal of the magnetization, reveals the impact of the AHE. The influence of the OHE was removed from the measurement. The normalized perpendicular component of the magnetization  $m_{\perp}$  is proportional to  $U_y$ . Above  $\mu_0 |H| \approx 2$  T the system is in magnetic saturation. The anisotropy constants are obtained by fitting Eq. 3.2 to the data in the regime of magnetization reversal (blue curve).

to use the anomalous transverse MR and/or MTEP effects which are sensitive to  $M_z$ , i.e., the AHE (2.1.2) and ANE (2.2.2). In the standard measurement geometry the external field  $\mathbf{H}$  is aligned with the hard axis (film normal) and the effect signal (transverse voltage  $U_y$ ) is proportional to  $m_{\perp} = M_{\perp}/M_S$  which defines the perpendicular component of  $\mathbf{M}$  normalized to the saturation magnetization. The competing of the anisotropy and Zeeman energy is then described in second order approximation with the first and second order anisotropy constants  $K_1$  and  $K_2$  by the following relation [40]:

$$-\left(\frac{2K_1}{M_S} + \frac{4K_2}{M_S}\right)m_{\perp} + \frac{4K_2}{M_S}m_{\perp}^3 = \mu_0 H(m_{\perp}) . \quad (3.2)$$

Depending on the availability<sup>2</sup> of measurements, the AHE, the ANE, and the parasitic ANE (see Sec. 3.4.4) are evaluated for each sample by fitting Eq. 3.2 to the data to determine the anisotropy constants. As an example, Fig. 3.4 depicts the transverse voltage  $U_y$  over the external perpendicular field strength  $\mu_0 H$  for  $t_{\text{Co}} = 6$  nm, revealing the impact of the AHE. The influence of the ordinary Hall effect was removed from the measurement. Above  $\mu_0 |H| \approx 2$  T the system is in magnetic saturation with a maximum voltage of  $\pm U_S$  while in the range between the magnetization reversal takes place. The blue curve in this segment represents the fit using  $m_{\perp} \propto U_y$  which gives as a result for the anisotropy constants. As it was found before [40] that  $K_2$ , influencing the curvature, is more

<sup>2</sup>For some samples the Hall/Nernst bars of the Co/Pt wire were corrupted during fabrication or in the course of the measurements.

### 3.1 Pt/Co/Pt sample system

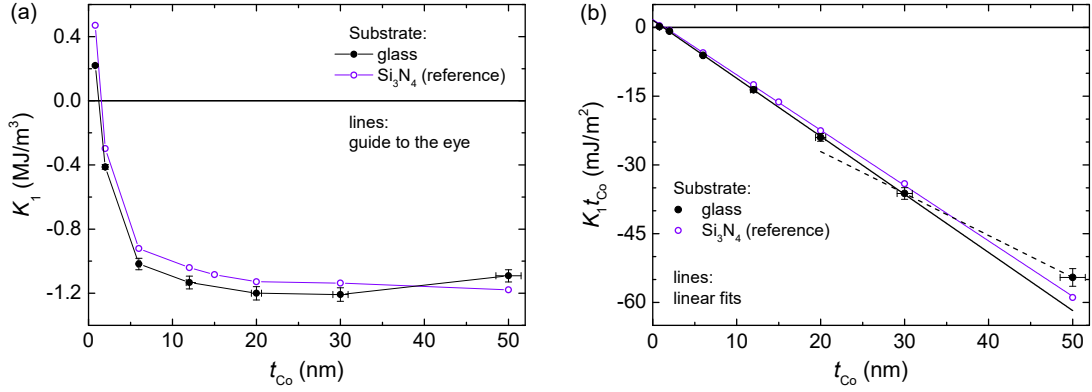


**Figure 3.5:** (a) Thickness dependence of the anisotropy constant  $K_1$  (Eq. 3.3) for Pt/Co/Pt on glass substrate and Si<sub>3</sub>N<sub>4</sub> (reference samples), respectively, in the range of  $t_{Co} = 0.8$  nm up to 50 nm. The values for samples with an easy plane (substrate plane) of magnetization ( $K_1 < 0$ ) are obtained from the measurements exemplary depicted in Fig. 3.4. Only for  $t_{Co} = 0.8$  nm the film exhibits a perpendicular easy axis of magnetization. The gradual decrease of the curve is due to the reduced impact of the surface anisotropy on the overall anisotropy with increasing Co thickness. (b)  $K_1 \cdot t_{Co}$  versus  $t_{Co}$  representation (see Eq. 3.4) of the data from (a). Here, the slope of the curve represents  $K_{1V,eff}$ , including volume and shape anisotropy, and the  $y$ -intercept gives the value for  $2K_{1S}$ . For  $t_{Co} \leq 30$  nm (glass substrate)  $K_{1V,eff}^{fcc} \approx -1.25$  MJ/m<sup>3</sup> and  $K_{1S} \approx 0.73$  mJ/m<sup>2</sup> are obtained. The deviation at  $t_{Co} = 50$  nm is addressed in the text.

or less independent of thickness it was set to  $K_2 = 70$  kJ/m<sup>3</sup> in the evaluation for all samples with different  $t_{Co}$ .

In the further analysis only the anisotropy terms of first order are considered. The constant  $K_1$  from Eq. 3.2 can be expressed as

$$K_1 = \underbrace{K_{1V} - \frac{\mu_0}{2} M_S^2}_{K_{1V,eff}} + \frac{2K_{1S}}{t_{Co}} . \quad (3.3)$$

The effective volume term  $K_{1V,eff}$  is defined as the sum of the magnetocrystalline volume anisotropy and the shape anisotropy. The influence of the surface anisotropy decreases with rising  $t_{Co}$  which is a consequence of the decreasing interface to volume ratio. The Figure 3.5(a) shows the thickness dependence of  $K_1$  for Pt/Co/Pt on glass substrate in the range of  $t_{Co} = 0.8$  nm up to 50 nm. Additionally, the results for the reference samples produced simultaneously on Si<sub>3</sub>N<sub>4</sub> (3.1.1) are plotted. The curves reveal that for  $t_{Co} = 0.8$  nm the film exhibits a perpendicular easy axis of magnetization ( $K_1 > 0$ ) while for the remaining samples an easy plane behavior is found where  $K_1$  levels off to a constant negative value at approx. 20 nm which is slightly lower in case of the glass substrate compared to Si<sub>3</sub>N<sub>4</sub>. The gradual decrease is due to the reduced impact of the surface anisotropy on the overall anisotropy. The divergent value at 50 nm for the

### 3 Experimental details

sample on glass will be addressed later on.

When modifying Eq. 3.3 by multiplication with  $t_{\text{Co}}$  it is transferred into the following relation:

$$K_1(t_{\text{Co}}) \cdot t_{\text{Co}} = K_{1V,\text{eff}} \cdot t_{\text{Co}} + 2K_{1S} . \quad (3.4)$$

As a consequence, in the  $K_1 \cdot t_{\text{Co}}$  versus  $t_{\text{Co}}$  plot (see Fig. 3.5(b) including linear fits of Eq. 3.4 to the data) the slope of the curve represents  $K_{1V,\text{eff}}$ , including volume and shape anisotropy, and the  $y$ -intercept gives the value for  $2K_{1S}$ . Under the valid assumption of *fcc* growth, the results for  $\text{Si}_3\text{N}_4$  are  $K_{1V,\text{eff}}^{\text{fcc}} \approx -1.20 \text{ MJ/m}^3$  and  $K_{1S} \approx 0.85 \text{ mJ/m}^2$  which is in good agreement with other works where similar samples are used (e.g. Ref. [40]). In the case of the glass substrate (comparable to  $\text{SiO}_2$ ) the following values are obtained for  $t_{\text{Co}} \leq 30 \text{ nm}$ :  $K_{1V,\text{eff}}^{\text{fcc}} \approx -1.25 \text{ MJ/m}^3$  and  $K_{1S} \approx 0.73 \text{ mJ/m}^2$ . Again, these results are very reasonable for *fcc* Co/Pt. The slight deviations for the different substrates can be explained among other things by different relaxation of crystalline strain [83, 84, 85]. When looking at the slope between  $t_{\text{Co}} = 30 \text{ nm}$  and  $50 \text{ nm}$  for the use of glass substrate (only two data points) a value of  $K_{1V,\text{eff}} \approx -0.90 \text{ MJ/m}^3$  is received. As the effective value for *hcp* Co growth  $K_{1V,\text{eff}}^{\text{hcp}}$  was found to be  $-0.73 \text{ MJ/m}^3$  [40] it can be argued that in this regime a coexistence of *fcc* and *hcp* is present, gradually tending towards *hcp* growth for higher  $t_{\text{Co}}$ . However, further investigations are needed to confirm this assumption.

It is worth mentioning that also for small Co thicknesses (approx.  $t_{\text{Co}} \leq 4 \text{ nm}$ ) a change of the slope takes place, resulting in different  $K_{1V,\text{eff}}$  and  $K_{1S}$  values [40]. From the available data this behavior cannot be resolved and, therefore, will not be discussed here.

When performing the MTEP measurements the sample underlies a temperature gradient with a typical maximum temperature difference of  $50 \text{ K}$  (see Sec. 3.2.3). From investigations regarding the temperature dependence of the anisotropy [40] it is expected that this will not generate a significant change in anisotropy along the Co/Pt wire. This could be confirmed by comparing the results obtained from the AHE and ANE as they do not show deviations that exceed the error margins.

## 3.2 Measurement principles

This section deals with the measurement principles of the MR and MTEP investigations. After introducing the measurement setup (3.2.1) and defining the main measurement geometries (3.2.2), the temperature calibration necessary to quantify the results of the magneto-thermoelectric measurements is presented in Sec. 3.2.3.

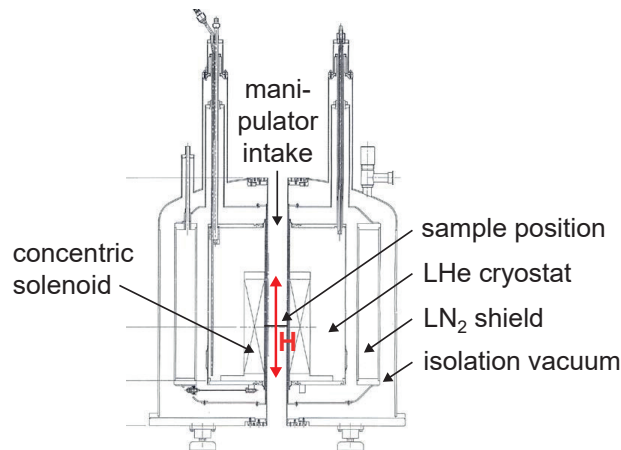


**Figure 3.6:** Cross sectional technical drawing of the superconducting electromagnet. The main features and position of the sample mounted on the manipulator are labeled in the picture. Adapted from Ref. [40].

### 3.2.1 Measurement setup

A core requirement for the MR and MTEP measurements is a specific manipulation of the magnetization of the investigated samples. This is achieved by means of an external magnetic field provided by a superconducting electromagnet from *Oxford Instruments*, see Fig. 3.6. The used device features a solenoid embedded in a helium cryostat which surrounds the cylindrical chamber in which the sample manipulator is located. Apart from the necessary vacuum isolation of the helium cryostat the magnet is also equipped with a liquid nitrogen radiation shield in order to diminish the liquid helium consumption. The magnet is able to provide a field (oriented vertically relative to the floor plane) up to  $\pm 11$  T in the center of the concentric coils, i.e., the sample position. A sample mounted on the manipulator and inserted into the magnet can be rotated within two planes which allows an alteration of the magnetization within or perpendicular to the substrate plane of the specimen. In the course of the measurements the sample position may slightly vary from the center axis of the solenoid but deviations from the desired field strength at the sample position are extremely small and can be neglected [40].

The inserted sample is exposed to ambient conditions of the lab but due to a naturally imperfect isolation of the cryostat the temperature in the chamber is slightly lower than room temperature so that the base temperature for the measurements performed with this device is about 290 K.

### 3.2.2 Measurement scheme

In this section the main measurement geometries for the MR and MTEP investigations are explained based on a simplified scheme depicted in Fig. 3.7. The

### 3 Experimental details

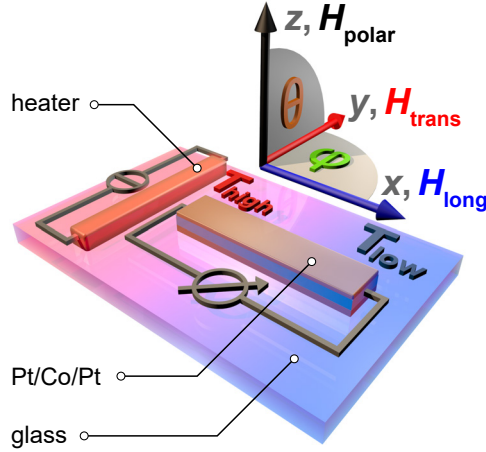


**Figure 3.7:** Sketch of the Pt/Co/Pt wire and Pt heating wire on the glass substrate including the denotation of the main measuring geometries. While the wiring is depicted for the MTEP investigations, the scheme is also valid for MR measurements. The surface of the substrate is located in the  $xy$ -plane. The long axis of the sample wire is parallel to the  $x$ -axis, the short wire edge is parallel to the  $y$ -axis, and the stacking direction of the film system is parallel to the  $z$ -axis. In case of the field sweep measurements (Sec. 3.3.1) the external magnetic field is individually aligned along one of the three generic directions and denoted as follows: longitudinal ( $\mathbf{H} \parallel \mathbf{x}$ ), transverse ( $\mathbf{H} \parallel \mathbf{y}$ ), polar ( $\mathbf{H} \parallel \mathbf{z}$ ). During the rotation measurements (Sec. 3.3.2) the angle of a constant high external field keeping  $\mathbf{M} \parallel \mathbf{H}$  is varied in the substrate plane (in-plane:  $\varphi$ ) or in the plane perpendicular to the current / voltage drop direction (out-of-plane:  $\theta$ ), respectively.

scheme shows the Pt/Co/Pt wire and the heating wire on the glass substrate including the circuit diagram for the thermoelectric measurements. The case for MR is not presented as the focus lies on the orientation of the wire relative to the coordinate system also shown in the picture.

The surface of the substrate is located in the  $xy$ -plane whereby the long axis of the sample wire, i.e., the direction of the impressed current (MR) or of the thermovoltage drop (MTEP), is parallel to the  $x$ -axis, the short wire edge is parallel to the  $y$ -axis, and the stacking direction of the film system is parallel to the  $z$ -axis.

The main types of measurements to characterize the MR and MTEP effects are on the one hand the variation of the external magnetic field  $\mathbf{H}$  at a fixed position of the sample, and on the other hand the variation of angle between the magnetic field and the sample at a constant field strength. The field variation measurements, also called sweep measurements, are mostly used to investigate the behavior of the system at high magnetic fields but also to gain information on the magnetization reversal. In order to do so, the magnetic field is aligned with one of the three generic directions of the wire which are denoted longitudinal for  $\mathbf{H} \parallel \mathbf{x}$ ,

transverse for  $\mathbf{H} \parallel \mathbf{y}$ , and polar for  $\mathbf{H} \parallel \mathbf{z}$ . In each case the field is varied from +6 T to -6 T (or vice versa) and back to the starting value at a typical rate of 0.2 T/min to 0.4 T/min. The primary reason of measuring the whole loop instead of only one direction is the identification of possible thermal drift in the recorded curves.

The other type of measurements (rotation measurements) has the purpose to study the angular dependence of the magnetization  $\mathbf{M}$  on the current or voltage drop direction. Here, a constant high external field of +6 T or -6 T which is sufficient to always keep the magnetization aligned with  $\mathbf{H}$  is used (for more details see Sec. 3.3.2) to be able to directly map the recorded data with the angle set at the magnet. As the sample mounted on the manipulator cannot be rotated by 360° the measurements are performed in two consecutive steps using both polarities of the external field to receive the full information on the angular dependence. As shown in the scheme for the so-called in-plane rotation the magnetization is varied like  $-95^\circ \leq \varphi \leq +95^\circ$  approximately starting from the transverse direction ( $\varphi = \pm 90^\circ$ ) and being aligned with the longitudinal direction at  $\varphi = 0^\circ$ . The out-of-plane rotation in the plane perpendicular to the current or voltage drop direction describes the angular dependence between  $-95^\circ \leq \theta \leq +95^\circ$  where  $\theta = \pm 90^\circ$  is the transverse and  $\theta = 0^\circ$  is the polar direction.

### 3.2.3 Temperature calibration

In order to gain the possibility to make a quantitative analysis of the thermovoltage  $U_{\text{th}}$  in the form of the Seebeck coefficient  $S = \lim_{\Delta T \rightarrow 0} \frac{-U_{\text{th}}}{\Delta T}$  a temperature calibration for the investigated samples is required. The method presented here gives as a result the temperature at the hot and cold end of the Co/Pt wire, respectively, and, therefore, the temperature difference  $\Delta T = T_{\text{hot}} - T_{\text{cold}}$ .

The calibration is a two-step-process performed by means of a *Quantum Design PPMS DynaCool*. In each step the electrical resistance of the upper and lower wire thermometer is monitored by a four-point measurement technique using a non-invasive current of 0.2 mA. At first, the whole sample is slowly heated from 290 K to 360 K (at heating power  $P_{\text{h}} = 0$  mW) to obtain the resistance of the wire thermometers  $R_{\text{t}1}$  and  $R_{\text{t}2}$  in dependence on the temperature  $T$ . This happens in an air atmosphere, on the one hand, to ensure a preferably uniform heating of the sample, and on the other hand, to account for the convection as the magnetothermoelectric measurements are performed under ambient conditions of the lab. In a second step at the base temperature of the MTEP experiments of about 290 K the heating power  $P_{\text{h}}$  is ramped up while  $R_{\text{t}1}$  and  $R_{\text{t}2}$  are recorded. The correlation of the received  $R_{\text{t}}(T)$  and  $R_{\text{t}}(P_{\text{h}})$  curves (see Fig. 3.8) results in the dependence  $T(P_{\text{h}})$  for each thermometer so that the temperature difference along the Co/Pt wire  $\Delta T(P_{\text{h}})$  is easily obtained (see Fig. 3.8(c)). For the investigated range of 0 mW to about 20 mW (reached at an impressed heating current of

### 3 Experimental details

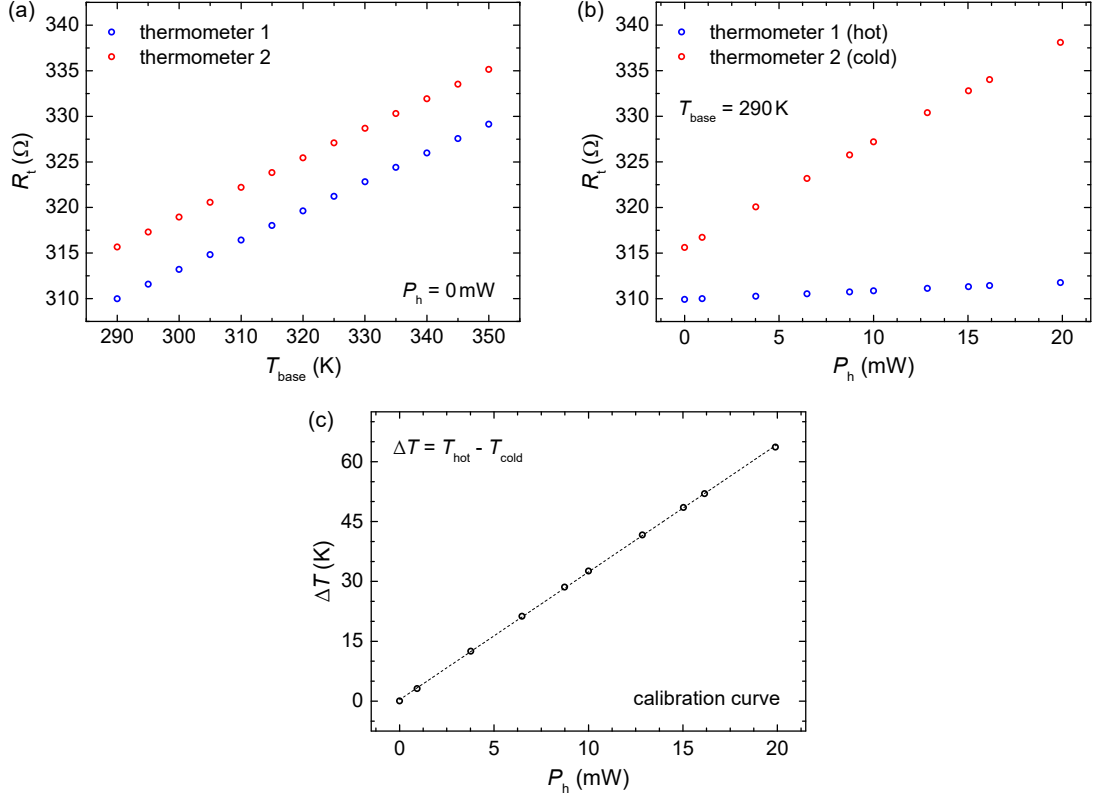


**Figure 3.8:** Temperature calibration curves for a sample with  $t_{\text{Co}} = 2$  nm. (a) Electrical resistance  $R_{t1}$  and  $R_{t2}$  of the two wire thermometers (Sec. 3.1.2) in dependence on the base temperature  $T_{\text{base}}$  ranging from 290 K to 360 K (at heating power  $P_h = 0$  mW). (b) Resistance  $R_{t1}$  and  $R_{t2}$  at  $T_{\text{base}} = 290$  K for ramping up the heating power  $P_h$  to approx. 20 mW.  $R_{t1}$  increases stronger than  $R_{t2}$  as it corresponds to the thermometer closer to the heating source. (c) Temperature difference  $\Delta T = T_{\text{hot}} - T_{\text{cold}}$  between the hot and cold wire end in dependence on the applied heating power  $P_h$ . The curve is obtained from the correlation of the  $R_t(T)$  and  $R_t(P_h)$  curves, see (a) and (b), and yields a linear dependence with a deviation smaller than 3%.

approx. 5 mA) this curve is linear with a deviation smaller than 3%. At the maximum heating power the temperature difference is  $\Delta T = (63.7 \pm 0.5)$  K with  $T_{\text{cold}} \approx 295.5$  K for the shown curves received for the sample with  $t_{\text{Co}} = 2$  nm.

Regarding the reversibility of the experiments it is important to ensure that no structural changes in the wire thermometers and Co/Pt wire occur while the described process. Therefore, an annealing of the heating wire is performed beforehand using a heater power which is slightly higher than the values used during the calibration or any of the following measurements. Within the measuring resolution the highest achieved temperature in the Co/Pt wire has no influence concerning the anisotropy (see Sec. 3.1.3).

The temperature calibration was conducted for three different samples with

## 3.2 Measurement principles

cobalt thicknesses of  $t_{\text{Co}} = 0.8 \text{ nm}$ ,  $2 \text{ nm}$  and  $50 \text{ nm}$ . It was found that the results show only small deviations, thus it can be concluded that the heat transfer is carried mostly by the glass substrate. Further evidence supporting this assumption is that the Nernst signal, i.e., the transverse voltage at the half length of the wire is equal for two samples with the same Co thickness of  $t_{\text{Co}} = 6 \text{ nm}$  but different widths of  $10 \mu\text{m}$  and  $20 \mu\text{m}$  and therefore different volumes and contact surfaces shared with the substrate (see curves in Fig. 3.14 in Sec. 3.3.4). This means that not only  $\Delta T$  between the wire ends but also the temperature gradient along the wire (see Eq. 2.22) is nearly the same. Especially for the differential expressions (as for instance  $\Delta S/\Delta T$ ) small deviations in the temperature calibration can be neglected (also see the characteristic curves in Sec. 3.4.2).

All magneto-thermoelectric measurements are conducted at a heating power of  $P_{\text{h}} = 15 \text{ mW}$  as this operating point turned out to be the best compromise between a sufficiently high thermovoltage and measuring in the linear regime of the  $S(\Delta T)$  curve (see Fig. 3.18 in Sec. 3.4.2). This corresponds to a temperature difference of  $\Delta T \approx 49 \text{ K}$ . If the measurements are performed at much smaller temperature differences the uncertainty in the determination of the Seebeck coefficient rises and if going to much higher heating powers ( $P_{\text{h}} > 20 \text{ mW}$ ) the relative increase of  $S$  with  $P_{\text{h}}$  decreases. The latter is very likely due to an enhanced heating-up of the substrate at the cold end of the wire (compared to the hot end) which reduces the efficiency of achieved  $\Delta T$  per applied heating power.

As can be seen in Fig. 3.8(b) the cold end of the Co/Pt wire also slightly heats up when applying the heating current. Thus, some of the contacting pads, especially pads 2 and 5 (see Fig. 3.2), heat up, too, as they are located within the same distance from the heater like the cold wire end. Due to this circumstance an additional thermovoltage is introduced because of the different temperatures at the transitions from the Pt pad to the Al bond for a measurement of the longitudinal voltage. This leads to a small offset voltage in the magneto-thermoelectric measurements. To minimize this preferably only the outer pads 1 and 6 at the hot wire end are used to measure  $U_{\text{th}}$ . In order to study the magnitude of the offset voltage a sample without the cobalt layer ( $t_{\text{Co}} = 0 \text{ nm}$ ) but otherwise the same specifications like the other samples was prepared. The results for the investigation of  $U_{\text{th}}(\Delta T)$  and  $S(\Delta T)$  obtained from the measurement along the inner and outer pads, respectively, are shown in Fig. 3.9.

Interestingly, when using the outer pads the thermopower is not constantly zero which could be expected as according to the temperature calibration curve of the cold wire end these remote pads do not heat up or at least only for high heating powers. Instead, a thermovoltage is already detectable for very small temperature differences where the temperature of all pads still equals the base temperature. The explanation for this finding is the fact that the absolute thermopowers of the platinum of the contacting structure ( $60 \text{ nm}$ ) and the thinner platinum of the wire ( $8 \text{ nm}$ ) are different [86] (also see Sec. 3.4.2) so that this combination

### 3 Experimental details

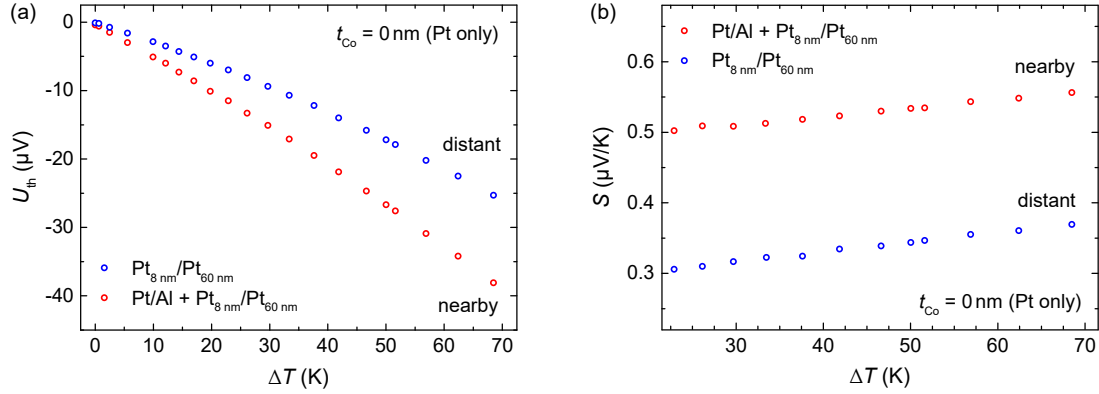


**Figure 3.9:** (a) Thermovoltage  $U_{th}$  and (b) thermopower  $S$  in dependence on the temperature difference  $\Delta T$  for a wire without a Co layer ( $t_{Co} = 0\text{ nm}$ ) but otherwise the same properties like the other samples. The different curves are obtained for the contacting of the nearby (2, 5) and distant (1, 6) Pt pads with Al bonds, see also Fig. 3.2. The signal for the use of the distant pads is due to the different (thickness dependent) absolute thermopowers of the Pt in the wire (8 nm) and contacting structure (60 nm) resulting in a relative thermopower unequal zero. In case of using the pads closer to the heating wire the Pt/Al transition slightly heats up which causes an additional contribution to the thermopower.

of thick and thin Pt acts as a thermocouple providing a relative thermovoltage. The thermopower obtained from measuring along the inner pads is different and represents the superposition of the described effect and the mentioned additional contribution of the heated Al/Pt transition closer to the heating wire. To address, amongst other things, this design flaw a new sample layout was designed, see Sec 3.1.2.

Further information, e.g., regarding the temperature profile/gradient along the Co/Pt wire, are discussed in the section on Nernst effects (3.3.4).

### 3.3 Field-dependent measurements

In this section exemplary investigations of the longitudinal resistivity and thermopower depending on the variation of an external magnetic field, i.e., field sweep measurements (3.3.1), and depending on the orientation of the magnetization in a saturating field, i.e., rotation measurements (3.3.2), are presented. For the rotation measurements a preliminary comparison of MR and MTEP effects is conducted, see Sec. 3.3.3. Furthermore, the transverse Hall and Nernst effects are described qualitatively (3.3.4), whereat the focus lies on the additional information on the sample system that can be derived from the Nernst effects.

### 3.3.1 Field sweep measurements

The field sweep measurements (see Sec. 3.2.2) were conducted for all samples of the series ranging from  $t_{\text{Co}} = 0.8$  nm to  $t_{\text{Co}} = 50$  nm. Exemplary, here the results for two samples are discussed, namely one sample ( $t_{\text{Co}} = 2$  nm) with an easy plane of magnetization ( $xy$ -plane), and one sample ( $t_{\text{Co}} = 0.8$  nm) with an easy axis of magnetization pointing out of the sample plane along the  $z$ -axis. The curves for the MR and MTEP sweeps are shown in Fig. 3.10.

In Fig. 3.10(a) the longitudinal resistivity versus the magnetic field strength is plotted for the three generic field orientations (3.2.2) obtained from the sample Pt (5 nm)/Co (2 nm)/Pt (3 nm). As in the case of  $\rho(H_{\text{trans}})$  and  $\rho(H_{\text{long}})$  the field  $\mathbf{H}$  is oriented in the easy plane of magnetization the curves represent a fast reversal of  $\mathbf{M}$  near 0 T. For the hard-axis curve  $\rho(H_{\text{polar}})$  a parabola-like behavior is visible between approximately +1 T and -1 T. This is due to the angle dependence of the AMR and AIMR effects combined with the circumstance of a coherent rotation of  $\mathbf{M}$  in this range. The steep resistivity changes at small fields between  $\pm 100$  mT are observable for all field sweep directions because of the magnetization reversal via domain wall movement. Here, the direction of the magnetization within the magnetic domains influences the resistivity due to the AMR effect. At technical saturation all curves merge into the same linear behavior, i.e., a decrease of resistivity on increase of field strength caused by the magnon MR [48, 87]. As a consequence of the isotropic high field behavior, the differences  $\Delta\rho_{\text{ip}} = \rho_{\text{long}} - \rho_{\text{trans}}$  (AMR) and  $\Delta\rho_{\text{op}} = \rho_{\text{polar}} - \rho_{\text{trans}}$  (AIMR) [17, 19] are constant above saturation and are equal to the differences in  $\rho$  extrapolated from high field behavior to zero field.

For the sample with  $t_{\text{Co}} = 0.8$  nm the transverse<sup>3</sup> and longitudinal measurements are hard axis/plane field sweeps while in the polar direction  $\mathbf{H}$  is parallel to the easy axis. The same characteristics as described above for  $t_{\text{Co}} = 2$  nm are visible (Fig. 3.10(c)), in this case with the coherent rotation behavior in  $\rho(H_{\text{trans}})$  and  $\rho(H_{\text{long}})$ . The creation of magnetic domains near zero field does not show in the curves as the magnetization in the domains is parallel to the  $z$ -axis so that the resistivity due to the AIMR effect is the same regardless of whether  $\mathbf{M}$  is pointing out of or into the sample plane. This is due to the circumstance of the AIMR being a longitudinal MR effect with an even functional behavior of  $\rho_x(\mathbf{M}, \mathbf{H})$  (2.1.1).

During the MR field sweep measurements which can take up to two hours (see Sec. 3.2.1) there may occur a change of the ambient temperature. If present, this temperature drift and hence the temperature-driven change of resistivity normally is linear in good approximation and smaller than 1 K so that a correction

---

<sup>3</sup>Note that for small Co thicknesses the slope of  $\rho(H_{\text{trans}})$  slightly differs from the other curves in the high field regime so that the behavior for the three generic field orientations is only approximately isotropic. This so-called anisotropic high field magnetoresistance (AHMR) was found by M. Hille and is described in Ref. [88].

### 3 Experimental details

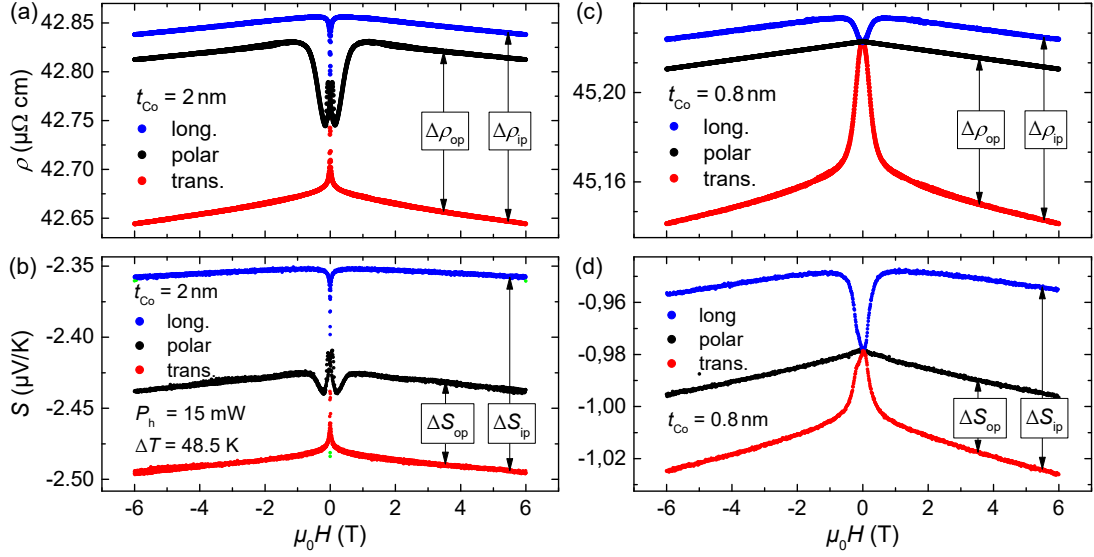


**Figure 3.10:** Field sweep measurements for (a), (b)  $t_{\text{Co}} = 2 \text{ nm}$  and (c), (d)  $t_{\text{Co}} = 0.8 \text{ nm}$ . (a), (c) Electrical resistivity  $\rho$  in dependence on the external magnetic field  $\mu_0 H$  aligned along the three principle directions transverse, longitudinal and polar, respectively, see Sec. 3.2.2. The results for the influence of the field on the thermopower  $S$  are plotted in (b), (d). The differences in resistivity and thermopower above technical saturation are labeled as  $\Delta\rho_{\text{ip}} = \rho_{\text{long}} - \rho_{\text{trans}}$  (AMR) and  $\Delta\rho_{\text{op}} = \rho_{\text{polar}} - \rho_{\text{trans}}$  (AIMR), and  $\Delta S_{\text{ip}} = |S_{\text{trans}}| - |S_{\text{long}}|$  (anisotropic MTEP or AMTEP) and  $\Delta S_{\text{op}} = |S_{\text{trans}}| - |S_{\text{polar}}|$  (interface AMTEP).

is straightforward. A temperature difference of 1 K corresponds to a change of resistivity of approximately  $0.04 \mu\Omega \text{ cm}$  [40, 89] for the measurement shown in Fig. 3.10(a).

Also in Fig. 3.10, the corresponding magneto-thermoelectric measurements of the very same samples with (b)  $t_{\text{Co}} = 2 \text{ nm}$  and (d)  $0.8 \text{ nm}$  are depicted. Qualitatively, each individual plot of Seebeck coefficient  $S = -U_{\text{th}}/\Delta T$  versus field strength resembles the corresponding  $\rho(\mathbf{H})$  curve which indicates that  $S(\mathbf{M})$  is inversely proportional to  $\rho(\mathbf{M})$  (see Eq. 2.17). Here, the thermovoltage  $U_{\text{th}}$  is the direct measurement parameter while the temperature difference  $\Delta T$  is obtained from the temperature calibration, see Sec. 3.2.3, to calculate the thermopower.

Above technical saturation, the absolute values of the three MTEP curves exhibit the following relation of Seebeck coefficients:  $|S_{\text{trans}}| > |S_{\text{polar}}| > |S_{\text{long}}|$ . Due to the isotropic high field behavior, the differences between the curves are again constant above saturation. The magneto-thermoelectric power caused by the AMR of Co is given by  $\Delta S_{\text{ip}} = |S_{\text{trans}}| - |S_{\text{long}}|$  (anisotropic MTEP or AMTEP) while the difference  $\Delta S_{\text{op}} = |S_{\text{trans}}| - |S_{\text{polar}}|$  is also distinctly larger than zero revealing the existence of the magneto-thermoelectric equivalent of the AIMR [90].

### 3.3 Field-dependent measurements

Note that the depicted MTEP curves, especially in the polar measurement geometry, were adjusted regarding some so-called parasitic effects which occur in the magneto-thermoelectric measurements. A detailed discussion of these complex contributions which are superimposed on the actual functional dependence of interest can be found in Sec. 3.4.4.

A possible small drift of temperature already mentioned in the context with the MR measurements does not have a significant impact in the MTEP experiments. While in the case of the resistivity slight changes of the base temperature are visible, the temperature difference  $\Delta T$  in the magneto-thermoelectric measurements will not be considerably affected by this. However, the temperature dependence of  $S$  could be an issue for a varying base temperature but this is not visible in the measurements. For a more detailed discussion see Sec. 3.4.1.

#### 3.3.2 Rotation measurements

Like the field sweep measurements (3.3.1), the rotation measurements, i.e., the angle dependence of resistivity or thermopower on magnetization (see Sec. 3.2.2), were conducted for all samples. Here, the results for the same two cobalt thicknesses that were already discussed in the section on the field dependence,  $t_{\text{Co}} = 0.8 \text{ nm}$  and  $2 \text{ nm}$ , are presented exemplary.

The field sweep curves  $\rho(\mathbf{H})$  and  $S(\mathbf{H})$  reveal an isotropic high field behavior of both the resistivity and Seebeck coefficient (Fig. 3.10) meaning that independent of the field orientation in this regime the here linear curves show the same slopes in  $\rho$  and  $S$ , respectively. This allows for the determination of  $\rho(\mathbf{M})$  and  $S(\mathbf{M})$  by simply rotating the samples in a field at which the magnetization  $\mathbf{M}$  is fully saturated without that any field-dependent effects distort the measurement. The here used field of  $\mu_0|H| = 6 \text{ T}$  is high enough to keep  $\mathbf{M}$  aligned with any direction of the field<sup>4</sup>.

In Fig. 3.11(a) and (c) the resistivity as a function of the orientation of  $\mathbf{M}$  is depicted for  $t_{\text{Co}} = 2 \text{ nm}$  and  $0.8 \text{ nm}$ , respectively. For the in-plane rotation  $\rho(\varphi)$  where  $\mathbf{M}$  is varied within the sample plane the characteristic  $\cos^2 \varphi$ -dependence (see Eq. 2.2) of the AMR effect is revealed for both samples. The lowest resistivity is reached for the transverse orientation of the magnetization while the highest value is present for  $\mathbf{M}$  aligned along the longitudinal (current) direction. The difference  $\Delta\rho_{\text{ip}} = \rho_{\text{long}} - \rho_{\text{trans}}$  describes the maximum change of resistivity due to the AMR (see also Sec. 3.3.1 on field sweeps). The out-of-plane variation of the magnetization  $\rho(\theta)$ , in the plane perpendicular to the electric current direction, shows the same functional behavior of resistivity (see Eq. 2.3) where the minimum

---

<sup>4</sup>This is especially valid for field orientations along the longitudinal, transverse and polar direction which is essential to correctly determine the investigated effect sizes. In some cases it is observed that at other orientations even for 6 T the Zeeman energy is not sufficient to fully overcome the magnetic anisotropy energy which leads to small deviations from  $\mathbf{M} \parallel \mathbf{H}$ .

### 3 Experimental details

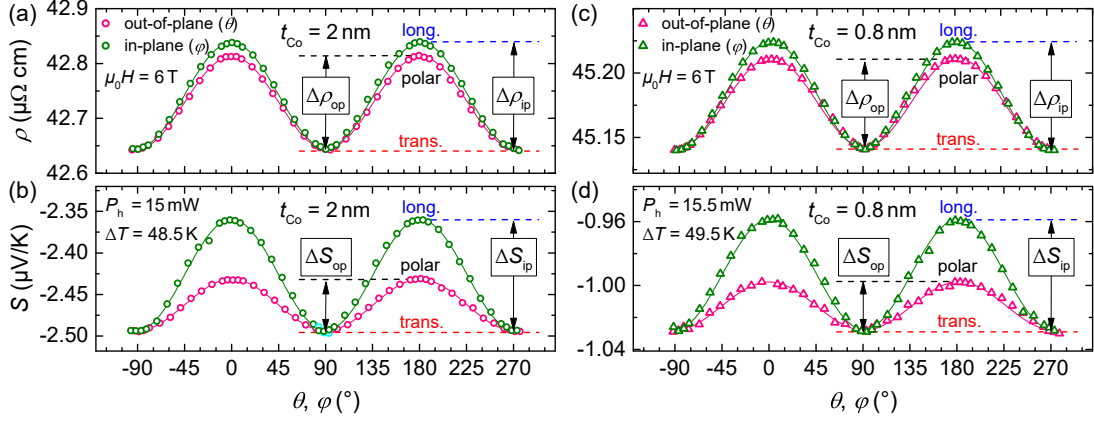


**Figure 3.11:** Rotation measurements for (a), (b)  $t_{\text{Co}} = 2$  nm and (c), (d)  $t_{\text{Co}} = 0.8$  nm. (a), (c) Electrical resistivity  $\rho$  as a function of the magnetization orientation for an in-plane ( $\varphi$ ) and out-of-plane ( $\theta$ ) angle variation, see Sec. 3.2.2. The results for the influence of the magnetization orientation on the thermopower  $S$  are plotted in (b), (d). The solid lines represent  $\cos^2$  fits to the data. The maximum differences (amplitudes) in resistivity and thermopower are labeled as  $\Delta\rho_{\text{ip}} = \rho_{\text{long}} - \rho_{\text{trans}}$  (AMR) and  $\Delta\rho_{\text{op}} = \rho_{\text{polar}} - \rho_{\text{trans}}$  (AIMR), and  $\Delta S_{\text{ip}} = |S_{\text{trans}}| - |S_{\text{long}}|$  (AMTEP) and  $\Delta S_{\text{op}} = |S_{\text{trans}}| - |S_{\text{polar}}|$  (interface AMTEP).

resistivity  $\rho_{\text{trans}}$  naturally is the same as for the in-plane effect. With  $\rho_{\text{polar}}$  as maximum, the out-of-plane effect size is denoted as  $\Delta\rho_{\text{op}} = \rho_{\text{polar}} - \rho_{\text{trans}}$  and is mainly caused by the AIMR for the depicted curves. If present, the geometrical size effect (GSE, see Sec. 2.1.1) of the investigated Co/Pt systems is only relevant for higher Co thickness where the impact of the AIMR effect to the measured signal is reduced due to the thickness dependence of the latter effect (2.1.1).

The corresponding MTEP measurements to the beforehand discussed MR curves are plotted in Fig. 3.11(b) and (d). Qualitatively, the  $S(\varphi)$  and  $S(\theta)$  curves match the angle dependence of the AMR and AIMR effect, respectively. This confirms the validity of the relation  $S \propto -1/\rho$  according to the Mott formula (see Eq. 2.17) for both rotational geometries. The Seebeck coefficient in dependence on the in-plane variation of the magnetization  $S(\varphi)$  reveals the conventional bulk anisotropic magneto-thermoelectric power (AMTEP) effect [66] with an amplitude of  $\Delta S_{\text{ip}} = |S_{\text{trans}}| - |S_{\text{long}}|$  (see Sec. 2.2.2). The out-of-plane rotation curve  $S(\theta)$  is characterized by

$$S(\theta) = S_{\text{trans}} + \Delta S_{\text{op}} \cos^2 \theta \quad (3.5)$$

with  $\Delta S_{\text{op}} = |S_{\text{trans}}| - |S_{\text{polar}}| > 0$  and represents the magneto-thermoelectric counterpart of the AIMR effect. It was named interface AMTEP and firstly reported in the course of this work, see Ref. [90]. Consequently, the dependence of the thermopower on  $\mathbf{M}$  for any orientation can be summarized as

$$S(\varphi, \theta) = S_{\text{trans}} + \Delta S_{\text{ip}} \cos^2 \varphi \sin^2 \theta + \Delta S_{\text{op}} \cos^2 \theta . \quad (3.6)$$

### 3.3 Field-dependent measurements

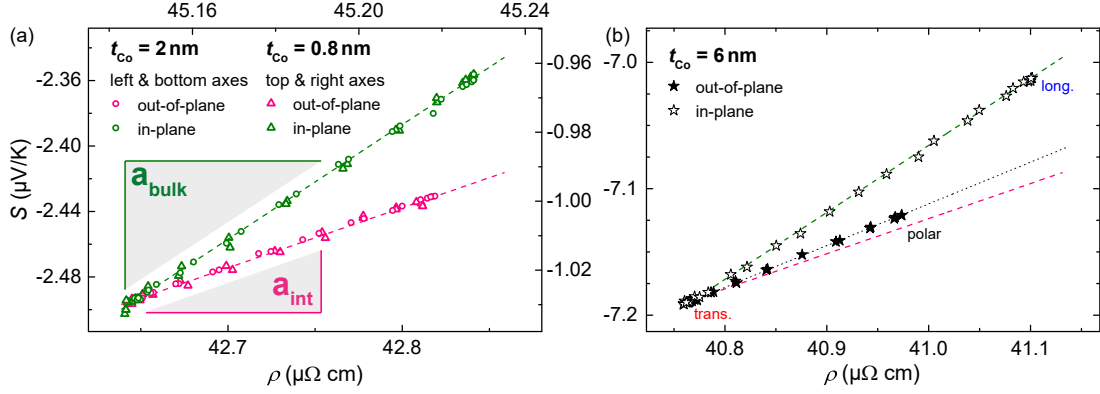


**Figure 3.12:** Thermopower  $S$  plotted over the electrical resistivity  $\rho$  for (a)  $t_{\text{Co}} = 0.8\text{ nm}$  and  $t_{\text{Co}} = 2\text{ nm}$  (data from Fig. 3.11), and for (b)  $t_{\text{Co}} = 6\text{ nm}$ . The curves represent the in-plane and out-of-plane variation of the magnetization, respectively. The slopes indicating the relative scaling of the bulk and interface effects in the MR and MTEP measurements are labeled as  $a_{\text{bulk}} = \Delta S_{\text{ip}}/\Delta\rho_{\text{ip}}$  and  $a_{\text{int}} = \Delta S_{\text{op}}/\Delta\rho_{\text{op}}$ . The ratio  $a_{\text{int}}/a_{\text{bulk}} \approx 0.52$  is obtained for the two thin films while for  $t_{\text{Co}} = 6\text{ nm}$  it is approx. 0.63. In (b) the slope  $a_{\text{bulk}}$  from (a) is scaled to match the data (in-plane) emphasizing the difference in ratios as  $a_{\text{int}}$  does not match the out-of-plane data.

As already mentioned in context with the field sweep measurements, parasitic effects may occur in the magneto-thermoelectric measurements due to the nature of the applied temperature gradient. Naturally, this also concerns the rotation curves depicted in Fig. 3.11 where these contributions were removed. For more details, see Sec. 3.4.4. Because of the layered structure of the Pt/Co/Pt samples the magnitudes of the MR and MTEP effects which only originate from the Co layer (and interfaces) are masked to a certain extent depending on the Co thickness due to the shunting influence of the Pt layers. To determine the genuine effect sizes and also to disentangle possibly occurring bulk effects (e.g., the GSE) from the AIMR / interface MTEP, which locally probe the Co/Pt interface region, the Co thickness dependence is evaluated, see Ch. 4.

Finally, when taking a closer look on the curves in Fig. 3.11 it is striking that the interface effect with respect to the bulk effect is larger in the MR than in the MTEP, meaning  $\Delta\rho_{\text{op}}/\Delta\rho_{\text{ip}} > \Delta S_{\text{op}}/\Delta S_{\text{ip}}$ , for both samples. This finding will be discussed in the following section.

#### 3.3.3 Electrical resistivity vs thermopower

In the previous section it was pointed out that, while the functional dependencies are the same, the relation of the in-plane and out-of-plane MR effect sizes  $\Delta\rho_{\text{op}}/\Delta\rho_{\text{ip}}$  compared to the MTEP effect sizes  $\Delta S_{\text{op}}/\Delta S_{\text{ip}}$  is distinctly different for each of the two discussed samples with  $t_{\text{Co}} = 0.8\text{ nm}$  and  $2\text{ nm}$ . For the sake of better comparison, for the bulk effects (AMR and AMTEP) the thermopower  $S(\varphi)$

### 3 Experimental details

is mapped onto the resistivity curve  $\rho(\varphi)$ , and for the interface effects (AIMR and interface AMTEP),  $S(\theta)$  is plotted over  $\rho(\theta)$  as can be seen in Fig. 3.12(a). Because of the  $\cos^2$ -dependence of all the single measurements the two resulting curves are, of course, linear what visualizes the validity of the Mott formula in the form of  $S = a \cdot \rho$  (see Eq. 2.18) whereby the offset shall be disregarded. In case of the bulk contributions the slope is determined by  $a_{\text{bulk}} = \Delta S_{\text{ip}} / \Delta \rho_{\text{ip}}$  and for the interface effects by  $a_{\text{int}} = \Delta S_{\text{op}} / \Delta \rho_{\text{op}}$ . As a consequence of the mentioned different relative scaling of the single measurements the two curves  $S(\rho(\varphi))$  and  $S(\rho(\theta))$  exhibit different slopes with the smaller one for the interface effects. Quantitatively, as ratio for the slopes,  $a_{\text{int}}/a_{\text{bulk}} = 0.52 \pm 0.02$  is obtained for  $t_{\text{Co}} = 0.8$  nm and  $a_{\text{int}}/a_{\text{bulk}} = 0.53 \pm 0.02$  is obtained for  $t_{\text{Co}} = 2$  nm which are the same within the error margins. In other words, the scaling of the magnetization dependent contributions to the thermopower depending on the resistivity is different for bulk and interface. As the same magnitude of this scaling was found for two samples with different Co thickness and, thus, different shunting influence of the Pt, it is reasonable to assume the generality of this finding. Especially, because the impact of the layered structure in the regime of relatively thin Co layers, here 0.8 nm and 2 nm, cancels out in a first approximation when looking at the ratios of bulk and interface effect (not to be confused with the overall shunting influence), see Ch. 4.

As an example for higher Co thicknesses, the in-plane and out-of-plane  $S(\rho)$  curves for  $t_{\text{Co}} = 6$  nm are given in Fig. 3.12(b). The found slope ratio for this sample  $a_{\text{int}}/a_{\text{bulk}} = 0.63 \pm 0.02$  differs not negligible from the values obtained before. Hence, to properly classify this result in comparison to the ones for thin Co layers a consideration of the shunting influence is essential, especially, to rule out that the assumption of generality is violated. A modeling presented in Sec. 4.2.

Furthermore, for even larger Co thicknesses it has to be considered that the impact of bulk effects like the GSE (2.1.1) in the out-of-plane measurements may show up and become dominant. In addition, for decreasing values of  $|\Delta S_{\text{op}}|$  a proper correction for the parasitic effects occurring in the MTEP investigations (3.4.4) becomes challenging, see also Sec. 4.2.

#### 3.3.4 Hall and Nernst effects

The transverse MR and MTEP effects (see Ch. 2) are not in the main scope of this work but as they provide some helpful information about the investigated samples (for example regarding the magnetic anisotropy, see Sec. 3.1.3) or occur as parasitic effects (see Sec. 3.4.4) an introduction of their character is presented in the following.

In case of the MR measurements the two<sup>5</sup> present effects are the ordinary Hall

---

<sup>5</sup>Other transverse effects are the planar Hall effect (PHE) [91, 92] / planar Nernst effect (PNE) [93, 94, 66] which describe the impact of any longitudinal effect on the transverse voltage due to the tensorial properties of the resistivity / thermopower tensor.

### 3.3 Field-dependent measurements

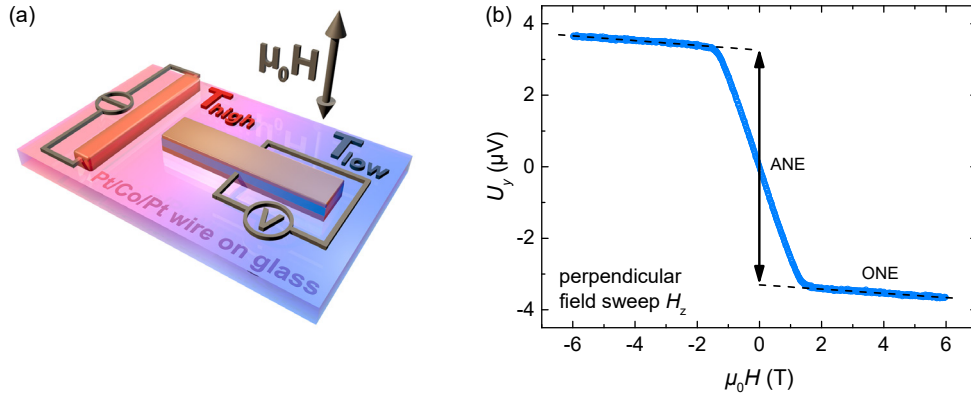


**Figure 3.13:** (a) Sketch of the Pt/Co/Pt wire and Pt heating wire on the glass substrate including the illustration of the electrical contacting to measure the transverse thermovoltage  $U_y$  when a temperature gradient is applied. The polar orientation of the external magnetic field  $H_z$  utilized to investigate the Nernst effects is indicated. (b) Transverse thermovoltage  $U_y$  in dependence on the magnetic field strength  $\mu_0 H_z$  for  $t_{\text{Co}} = 6$  nm. The curve shows the impact of the linear ONE arising from the Co and Pt, and the superimposed ANE originating from the Co layer. The signal due to the ANE is constant when the technical saturation of magnetization is reached.

effect (OHE) and the anomalous Hall effect (AHE). Their analogs in the MTEP investigations are the ordinary Nernst effect (ONE) and the anomalous Nernst effect (ANE). All the named effects are characterized by a cross product (see Sec. 2.1.2 and 2.2.2), meaning that the generated electric field is perpendicular to the direction of current (Hall) or temperature gradient (Nernst), and the magnetization or magnetic field. As the nature of the Hall and Nernst effects are qualitatively the same, exemplarily only the Nernst effects are discussed.

The Figure 3.13(a) depicts a sketch of the typical experimental setup to determine the Nernst effects. The heating wire creates a temperature gradient  $\partial T/\partial x$  along the Co/Pt wire while the external magnetic field  $H_z$  is oriented in polar direction. The resulting transverse voltage  $U_y$  in dependence on the field strength is plotted in Fig. 3.13(b) for a sample with  $t_{\text{Co}} = 6$  nm. The curve represents a superposition of the ONE arising from the Pt and Co layers, and the ANE that originates from the ferromagnetic Co. The ONE is linearly depending on  $H_z$  whereas the ANE, an effect sensitive to the magnetization  $M_z$ , only causes a change of voltage until the saturation magnetization is reached and then levels off to a constant contribution. Due to this nature the ordinary and anomalous Nernst effects can be easily separated. When looking at the qualitative behavior of the effects it is striking that they exhibit the same sign. This is an interesting finding as the constant of the ordinary Hall effect for both Co and Pt is negative [95, 96, 97, 98] while the anomalous Hall constant of Co is positive [99, 52] which means that in the transverse MR measurements the OHE and AHE show opposite

### 3 Experimental details

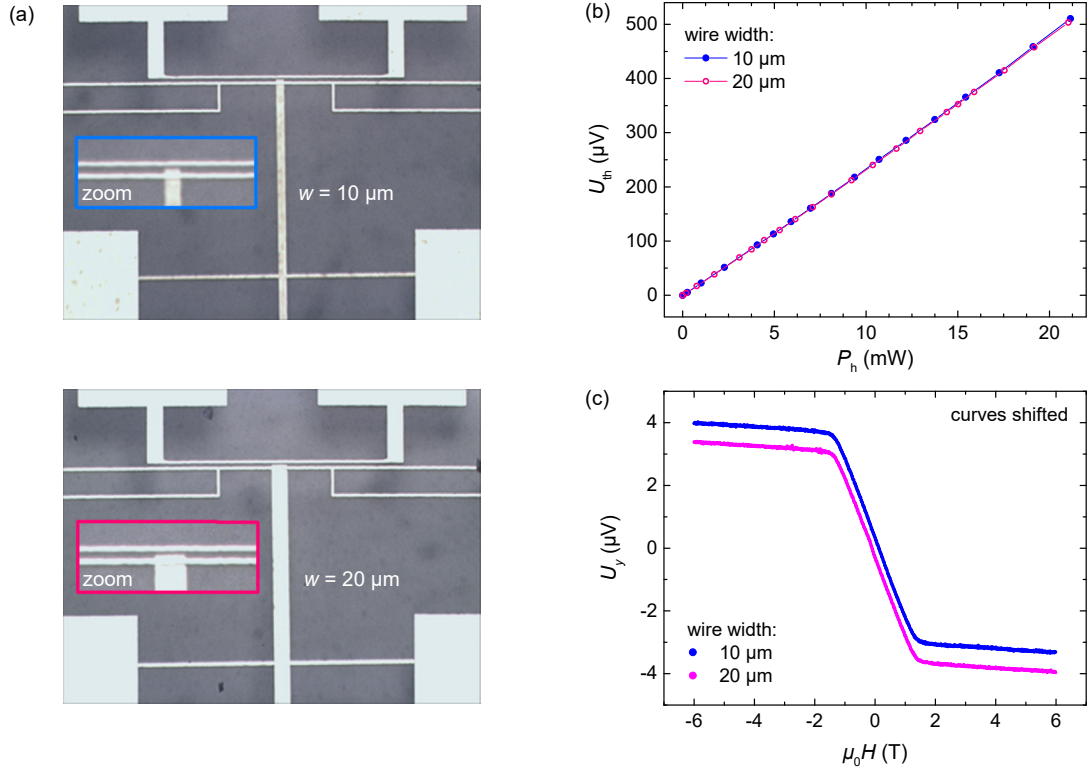


**Figure 3.14:** (a) Microscope photographs (zoom; for complete layout see Fig. 3.2) of two samples with  $t_{\text{Co}} = 6 \text{ nm}$  but different wire widths of  $10 \mu\text{m}$  and  $20 \mu\text{m}$ . (b) Longitudinal thermovoltage in dependence on the heating power for both samples. As a consequence to the good match of the single curves the temperature difference between the wire ends must be the same for both samples. (c) Transverse thermovoltage  $U_{\text{y}}$  as a function of the external field strength  $\mu_0 H$  for the  $10 \mu\text{m}$  and  $20 \mu\text{m}$  wide Co/Pt wire. The signals do not show significant deviations which means that not only the temperature differences but also the gradients along the wires are the same.

slopes. If the observed discrepancy is due to an intrinsic effect meaning that the relation  $S \propto \rho$  following the Mott formula (Eq. 2.18) has an opposite sign for one of the effects is still under investigation.

After describing the main features of the transverse effects, in the following some interesting findings on how to utilize the effects to learn about the behavior of the sample system (Co/Pt wire and glass substrate) in presence of a temperature gradient are discussed.

Like the Hall effects, the Nernst effects do not depend on the wire width if a constant current  $I_x$  or temperature gradient  $\partial T/\partial x$ , respectively, is maintained [100, 51]. This fact provides an experimental approach to check how the different thermal conductance of substrate and Co/Pt wire influence the heat distribution in the system. For this purpose two samples with the same  $t_{\text{Co}} = 6 \text{ nm}$  but different

### 3.3 Field-dependent measurements

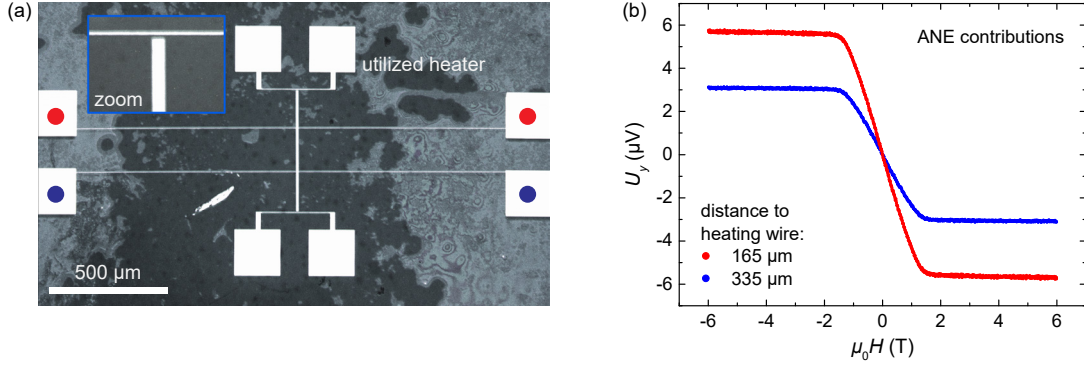


**Figure 3.15:** (a) Microscope photograph of a sample ( $t_{\text{Co}} = 6$  nm) with two Nernst bars to measure the transverse thermovoltage  $U_y$  at different distances from the heating wire. The Co/Pt wire has no contacting structures to measure the longitudinal voltage or temperatures at the wire ends but otherwise possesses the same properties as in the standard layout. (b) The transverse voltage  $U_y$  as a function of the polar magnetic field  $H_z$  measured at the two transverse bars for the use of the upper heating wire. The signal of the ONE was removed. The impact of the ANE is of different magnitude, higher for the (upper) bar in closer distance to the heating wire, what indicates a non-linear change of temperature along the Co/Pt wire.

widths of 10 μm and 20 μm and therefore different volumes and contact surfaces shared with the substrate were fabricated (see also Sec. 3.2.3). Alongside with the longitudinal thermovoltage dependence on the heating power, the  $U_y(H_z)$  curves for both samples, obtained for the same heating powers, are shown in Fig. 3.14. As they do not show any significant deviations and, consequently, the temperature gradient is the same, it is clearly revealed that the vast majority of heat transfer is carried by the substrate and the metal structures on the surface have no impact in this regard.

To roughly estimate how the temperature profile along the Co/Pt wire looks like another sample with two bars for measuring  $U_y$  was fabricated, see Fig. 3.15(a). The depicted sample features a Co/Pt wire with  $t_{\text{Co}} = 6$  nm and the same length of 510 μm as in the standard layout. It does not possess the contacting structures for longitudinal voltage measurements or temperature calibration but, as pointed out in Sec. 3.2.3 and above in this section, the temperature difference between the two ends of the wire can satisfactorily be obtained via interpolation from the temperature calibration curve for the applied heating power. At approx. one and two thirds of the total wire length the transverse voltage was measured. The resulting  $U_y$  curves obtained from the two transverse bars in dependence on the polar field  $H_z$  are depicted in Fig. 3.15(b). Note that the impact of the ONE was removed, only leaving the ANE signal.

Correctly, the generated transverse electric field  $E_y$  due to the Nernst effects is proportional to the temperature gradient  $\partial T/\partial x$  (2.2.2). In the case of the

### 3 Experimental details

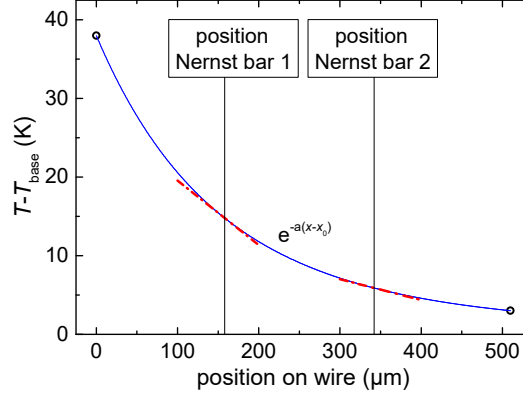


**Figure 3.16:** Temperature  $T$  of the wire with respect to the base temperature in dependence on the  $x$ -position along the wire depicted in Fig. 3.15(a). The hot end is located at  $x = 0$ . The  $T$  at the hot and cold wire end are obtained from the temperature calibration. The positions of the two Nernst bars are indicated. The curve shows a  $T(x) = e^{-a(x-x_0)}$  fit to the data and is an example how to estimate the temperature profile by the use of the slope ratio at the Nernst bar positions. This ratio is deduced from the ANE signals given in Fig. 3.15(b).

presented curves where the ANE is measured along the, compared to the overall wire length, slim transverse bars with  $\Delta x = 5 \mu\text{m}$  the following approximation is valid:  $\partial T / \partial x \approx \Delta T / \Delta x$ . This leads to  $E_y \propto \Delta T / \Delta x \propto U_y / \Delta x$  and with the given equal width of the two bars to  $U_y \propto \Delta T$ . When labeling the maximum voltage change due to the ANE as  $\Delta U_{\text{ANE}}$  this can be rewritten as  $\Delta U_{\text{ANE}} \propto \Delta T$ . The curves in Fig. 3.15(b) reveal that the Nernst bar closer to the used heating wire provides a larger effect size  $\Delta U_{\text{ANE}}$  than the second bar with a ratio of 1.83:1 between the two. Consequently, it can be concluded that the change of temperature along the Co/Pt wire is not linear but is increased in proximity to the heating source, which is a plausible finding for a volume substrate.

Additional to the change of temperature at the first transverse bar relative to the second one the absolute temperatures at the ends of the wire are deducible from the temperature calibration. For the here used power of 11 mW they are determined to be 38 K and 3 K above the base temperature of 290 K, causing a temperature difference of  $\Delta T = 35$  K. These two data points are plotted in Fig. 3.16 in dependence on the  $x$ -position on the Co/Pt wire with  $x = 0$  for the hot wire end. To estimate the temperature profile along the wire, in a first step a simple model that seems reasonable for a volume substrate is fitted to the  $T(x)$  plot, namely, an exponential decrease function  $T(x) = e^{-a(x-x_0)}$  is used, where  $a$  is the only scaling parameter and  $x_0$  serves as an offset parameter. In a second step, the slopes  $\Delta T / \Delta x$  at the Nernst bar position are determined for the model. The change of temperature at the first position is  $-0.0862$  K/ $\mu\text{m}$  and at the second  $-0.0348$  K/ $\mu\text{m}$  which leads to a ratio of 2.48:1. Compared to the ratio

### 3.4 Supplementary investigations

of the relative temperature change obtained from the ANE measurement this is a deviation of only 35 % meaning that the exponential model seems to describe the true temperature profile of the wire in good approximation. However, be advised that the assumption of an exponential decrease is not based on the claim of being the correct solution for the heat equation. In fact, it cannot account for the position of maximum temperature (heating wire at  $x = -10 \mu\text{m}$ ) like a Gaussian-like function would do, which in turn was found to not reasonably describe the measurement data at all (not shown). Consequently, the simple assumption rather serves the purpose of presenting an approach to verify a certain solution or to experimentally determine the temperature profile. For the latter more data points (via various Nernst bars) should be considered. Solving the heat equation for the system is probably rather complex as numerous boundary conditions, e.g., the shape of the heating wire, convection of the air, thermal interface resistances [101], etc., have to be accounted for.

Likewise by utilizing the ANE it could be shown that in the course of the magneto-thermoelectric measurements no polar temperature gradient  $\partial T/\partial z$  is induced in the Co/Pt wire within the experimental uncertainty which is addressed in more detail in Sec. 3.4.4.

It is worth mentioning that another sample with the same layout without the contacting structures like the one depicted in Fig. 3.15(a) was investigated. Here, a Co layer of 30 nm was directly deposited on the substrate without any Pt layers. The measurement of the the transverse voltage clearly reveals the impact of the ANE (not shown; similar to the results in Fig. 3.15(b)). Due to the lack of contacting structures and the Pt layers, which could establish a locally closed circuit, this obviously points to the presence of a net spin current in the Co whereat no net electrical current is present. Such structures could be used to study pure spin currents generated by temperature gradients.

## 3.4 Supplementary investigations

This section is concerned with some additional investigations that provide helpful information on the Co/Pt samples to be able to correctly interpret the results of the MTEP measurements.

In Sec. 3.4.1 the dependence of the thermovoltage on the base temperature for the investigated samples is briefly presented. It follows a look at the dependence of the thermopower on the present temperature difference along the Co/Pt wires and the heating-up behavior of the system after the heating power is applied (3.4.2). Furthermore, it is investigated if the tensorial properties of the electrical resistivity/conductivity are of any significant impact for the utilized sample system, see Sec. 3.4.3, especially regarding the relation  $S \propto -1/\rho$  taken for the Mott formula. In Sec. 3.4.4 the very important identification and treatment of occurring parasitic effects in the magneto-thermoelectric measurements are discussed, as

### 3 Experimental details

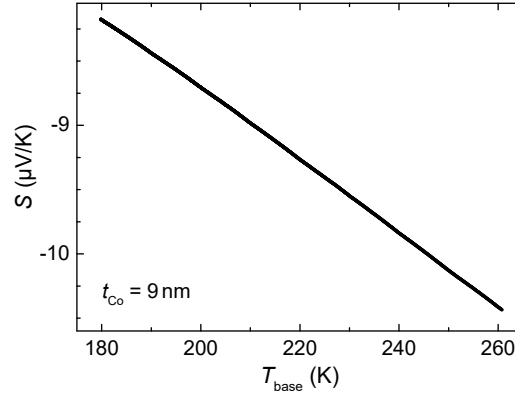


**Figure 3.17:** Seebeck coefficient  $S$  in dependence on the base temperature  $T$  for a sample with  $t_{\text{Co}} = 9$  nm from 180 K to 260 K at an applied heating power of 15 mW. The thermopower changes linearly with raising temperature at a rate of  $-0.03 \mu\text{V}/\text{K}^2$ .

without this the correct quantification of longitudinal MTEP effects cannot be accomplished.

#### 3.4.1 Temperature dependence of thermopower

In general, the absolute and thus also the relative Seebeck coefficient depends on the base temperature at which the measurement is performed. As in the case of the Pt/Co/Pt samples it is dealt with a system where the thickness dependence of  $S$ , as well as the shunting effects between the layers (see Sec. 4.2) are of importance, but no data for this specific system can be found in literature, a measurement of  $S(T)$  for one sample was conducted. This helps to gain knowledge of how a temperature drift during the measurements impacts on the result and also serves as a preliminary investigation for possible future magneto-thermoelectric measurements at different temperatures.

The Fig. 3.17 depicts the  $S(T)$  curve for a sample with  $t_{\text{Co}} = 9$  nm from 180 K to 260 K at an applied heating power of 15 mW. It was recorded by means of a *Spectromag* measurement setup. In the shown range the Seebeck coefficient decreases linearly with rising temperature at  $-0.03 \mu\text{V}/\text{K}^2$ . This equals a change of  $S$  per 1 K of 0.3%. With this finding one can estimate how a possible temperature drift (see Sec. 3.3.1) influences the magneto-thermoelectric measurements for other samples. In the example for the MTEP sweep measurement shown in Fig. 3.10(b) for  $t_{\text{Co}} = 2$  nm the maximum drift of 1 K sometimes observed for the MR sweeps would equal a change of  $S$  in the magnitude of  $0.007 \mu\text{V}/\text{K}^2$ . In comparison with the magneto-thermoelectric effects this would be a very small but still visible impact. However, most of the times no drift of  $T$  is observed at all. Thus, it can be assumed that the constant heating power supply stabilizes the system in the form of a continuous convection of the air in the direct vicinity of the sample.

### 3.4 Supplementary investigations

As mentioned above, the preliminary measurements on  $S(T)$  also provide insights for future temperature dependent MTEP investigations which are not part of this thesis. The main issue that was observed in the course of the experiments is the correct determination of the temperature difference between the hot and cold wire end which is essential to calculate the correct magnitude of the Seebeck coefficient. If, for example, the current for the desired heating power of 15 mW ( $\Delta T \approx 49$  K) is determined at room temperature, it is found that at  $T = 5$  K the heating power  $P_h$  is decreased by approximately 25 % for a constant current which is, of course, due to the lower resistivity of the Pt heating wire at lower temperatures. As a consequence, the heating current must be adapted for every temperature to maintain a constant  $P_h$ . Additionally, if the investigations are intended to cover a broad range of temperature, also the thermal conductivity of the substrate has to be taken into account so that the desired  $\Delta T$  can be kept at a constant value. This would make temperature calibrations at different base temperatures necessary. A different approach could be an alternating measurement of  $U_{th}$  and the thermometer resistance (or a new sample design with separate wire thermometers) to determine and adapt the temperature difference during the measurements by comparing with existing calibration curves (3.2.3).

Other experimental challenges of the temperature dependent investigations, especially for low temperatures are the strongly increasing Helium consumption due to the impressed heating power and, depending on the used measurement setup, the additional temperature gradient in the sample system a punctual cooling system would introduce.

#### 3.4.2 Dependence of thermopower on temperature difference

The thermopower  $S$  is formally defined for the limiting case of  $\Delta T \rightarrow 0$  as

$$S = \lim_{\Delta T \rightarrow 0} \left( \frac{-U_{th}}{\Delta T} \right) \quad (3.7)$$

where  $U_{th}$  is the measured thermovoltage over a temperature difference  $\Delta T$  at a certain base temperature  $T_{base}$ . Naturally, with no applied temperature difference no thermovoltage will be obtained so that the value for  $S$  has to be extrapolated from values at  $\Delta T \neq 0$ . While this provides information on the correct relative Seebeck coefficient at  $T_{base}$ , more importantly for the performed magneto-thermoelectric investigations, it can be checked if the magnetization orientation in the sample has any varying influence on  $S(\Delta T)$  which would make a correction of the measured values  $\Delta S_{ip}$  and  $\Delta S_{op}$  necessary.

The exemplary results for a measurement of the thermovoltage at varying temperature differences / heating powers are depicted in Fig. 3.18(a) for a sample with  $t_{Co} = 2$  nm. The curves were recorded for the three generic orientations of the applied magnetic field with a saturating strength of  $\mu_0 |H| = 6$  T in the range from zero up to approximately 65 K or 20 mW, respectively. The calculated

### 3 Experimental details

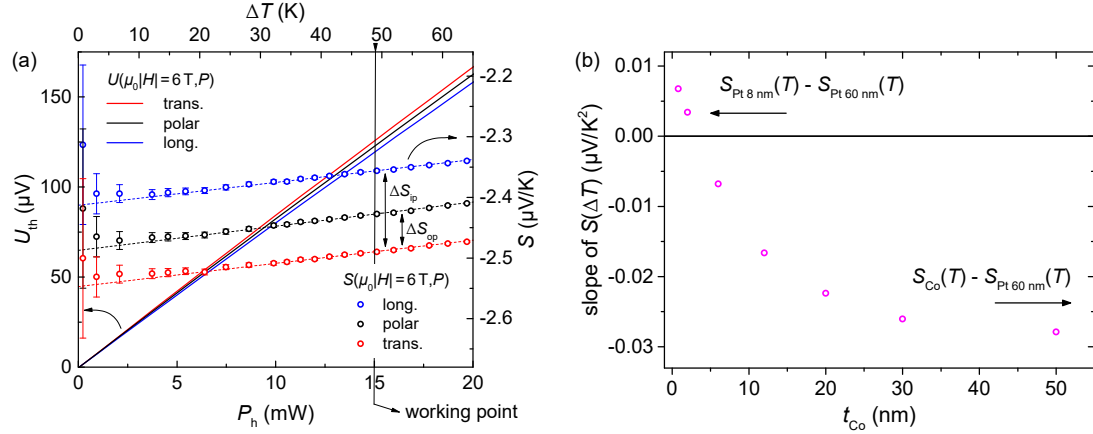


**Figure 3.18:** (a) Thermovoltage  $U_{th}$  for the three generic orientations of the applied magnetic field ( $\mu_0|H| = 6$  T) in dependence on the temperature difference  $\Delta T$  / heating power  $P_h$  (solid lines) for a sample with  $t_{Co} = 2$  nm. The also plotted thermopower is calculated via  $S = -U_{th}/\Delta T$  (circles). The dashed lines are linear fits to the curves for  $P > 7$  mW. The MTEP effect sizes  $\Delta S_{ip} = (U_{trans} - U_{long})/\Delta T$  and  $\Delta S_{op} = (U_{trans} - U_{polar})/\Delta T$  which are constant for the fitted regime are indicated. (b) Slope of the  $S(\Delta T)$  curves as a function of the Co thickness  $t_{Co}$ . The general shape of the curve is mainly determined by the different shunting and weighting of  $S_{Co}$  and  $S_{Pt}$  for different sample compositions. The unexpected positive slope in the regime of thin  $t_{Co}$  is assumed to be due to a different temperature dependence of  $S_{Pt}$  for the varying Pt thickness in the Pt/Co/Pt wire ( $t_{Pt} = 8$  nm) and the contacting structure ( $t_{Pt} = 60$  nm).

corresponding thermopowers  $S$  are also shown in the figure. It can be observed that the Seebeck coefficient describes the same qualitative behavior for the three field orientations, merging into a linear dependency for  $P_h \gtrsim 7$  mW illustrated by linear fits. In the range  $\lesssim 7$  mW the relatively large errors originate from deviations regarding the linearity between  $\Delta T$  and  $P_h$  as well as existing small offset voltages to  $U_{th}$  in the measurement setup. The most important observations are the constant slopes that are the same for all three curves and, therefore, the constant differences  $\Delta S_{ip} = (U_{trans} - U_{long})/\Delta T$  and  $\Delta S_{op} = (U_{trans} - U_{polar})/\Delta T$  between the curves in the linear regime. This implies that the MTEP results obtained for the standard working point of 15 mW are valid for a wide range of temperature differences, especially for the limiting case of  $\Delta T \rightarrow 0$  defining the Seebeck coefficient (Eq. 3.7).

It was found that the slopes of  $S(\Delta T)$  are different for varying cobalt thicknesses including a sign reversal, i.e., a negative slope, for higher  $t_{Co}$  as can be seen in Fig. 3.18(b). As the measurements are performed at the same base temperature and the platinum thickness is constant between samples the general shape of the depicted curve strongly indicates that the slope mainly is determined by the different shunting and weighting of  $S_{Co}$  and  $S_{Pt}$  for different sample compositions

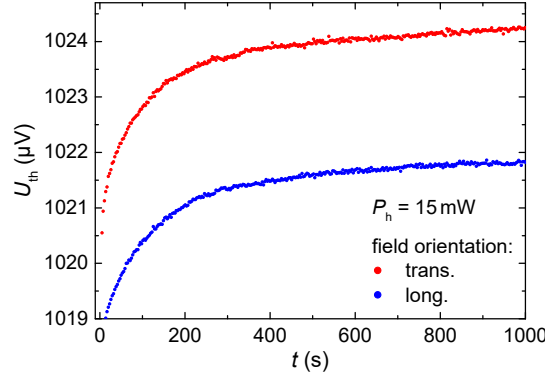


**Figure 3.19:** Time evolution of the thermovoltage  $U_{\text{th}}$  after applying a constant heating power of  $P_{\text{h}} = 15 \text{ mW}$  for the external field ( $\mu_0 H = 6 \text{ T}$ ) oriented in longitudinal and transverse direction, respectively ( $t_{\text{Co}} = 50 \text{ nm}$ ). After 5 min the system has almost reached a thermally stable state with a change rate  $< 0.1 \%$  for the following 10 min.

(for details see Sec. 4.2). For higher Co thicknesses where the impact of the Pt layers is reduced the evolution of the slope levels off to a constant negative value. This is consistent with literature [1, 102, 103] as, in the regime of the present  $T_{\text{base}}$  in the experiments, a decreasing  $S_{\text{Co}}$  is reported for a rise of the base temperature and, thus, also follows for an increasing temperature difference as the average temperature of the sample rises. In the case of  $S_{\text{Pt}}$  a negative slope of  $S(\Delta T)$  is expected, too [1, 102, 104], which consequently should be observed for samples with low  $t_{\text{Co}}$  where the impact of the Pt dominates the overall measured Seebeck coefficient. However, the results in the plot (Fig. 3.18(b)) contradict this statement. Three samples, namely, the ones with  $t_{\text{Co}} = 0.8 \text{ nm}$  and  $2 \text{ nm}$ , as well as the one with no Co layer at all (not plotted; see Fig. 3.9), show a positive slope. The latter sample possesses, apart from the missing Co, the same specifications like the other samples regarding the Pt layers and the Pt contacting structure, see also Sec. 3.2.3. The fact that despite  $t_{\text{Co}} = 0 \text{ nm}$  this sample where Pt is measured against Pt provides a thermopower at all is caused by the different thickness of the Pt in the wire ( $t_{\text{Pt}} = 8 \text{ nm}$ ) and the contacting structure ( $t_{\text{Pt}} = 60 \text{ nm}$ ) as for thin films the Seebeck coefficient is thickness dependent [86]. Coming back to the sign of the slope it is reasonable to assume that, while in general  $S_{\text{Pt}}$  decreases with temperature, the temperature dependence of  $S_{\text{Pt}}$  is slightly different for varying Pt thickness. If this assumption is valid, it would imply that  $S_{\text{Pt } 60 \text{ nm}}$  decreases stronger with temperature than  $S_{\text{Pt } 8 \text{ nm}}$  causing the observed positive slope of  $S(\Delta T)$  in the regime of thin  $t_{\text{Co}}$ .

As already mentioned in context with the sweep and rotational measurements there are parasitic contributions present in the measurements, especially for polar field orientations (see Sec. 3.4.4). These effects are eliminated in the shown curves

### 3 Experimental details

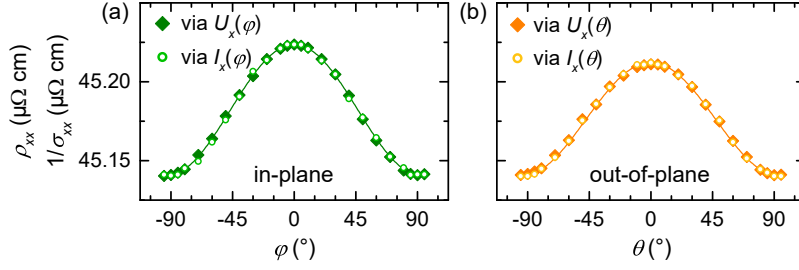


**Figure 3.20:** Resistivity  $\rho_{xx}$  and inverse conductivity  $1/\sigma_{xx}$  for Pt/Co(0.8 nm)/Pt as a function of angle of magnetization orientation. (a) and (b) show the results for rotating the magnetization in plane ( $\varphi$ ) and out of plane ( $\theta$ ), respectively. The angles are defined in Sec. 3.2.2.

by performing the measurements for both magnetic field polarities and calculating the average of the results. In consequence, the comparison of the  $S(\Delta T)$  curves from a certain sample allows to easily determine the magnitude of the bulk and interface AMTEP effects without conducting the rotational measurements. The values for  $\Delta S_{ip}$  and  $\Delta S_{op}$  from Fig. 3.11 are the same as the ones obtained from Fig. 3.18(a) within the error margins.

When investigating the dependence of the thermopower on the temperature difference the heating power needs to be gradually raised. To gain knowledge on the heating up behavior of the samples (here shown for  $t_{Co} = 50$  nm) the thermovoltage was recorded over time after applying a constant heating power of 15 mW, see Fig. 3.19. It is visible that after 5 min the system has almost reached a thermally stable state and the change of  $U_{th}$  becomes very small ( $< 0.1\%$  for the following 10 min). This and the fact that during the  $S(\Delta T)$  measurements  $P_h$  is only gradually raised show that the used waiting time of 5 min between data points in Fig. 3.18(a) is more than sufficient.

#### 3.4.3 Relation between electrical conductivity and resistivity

*This section closely follows the written elaboration in the Supplemental Material of my own publication, i.e., Ref. [90].*

As the Mott formula is originally derived in terms of electrical conductivity  $\sigma$  it was examined if the utilization of the reciprocal value of the measured electrical resistivity  $\rho$  is justified for the investigated polycrystalline Co/Pt samples.

In experiments on electrical transport the resistivity  $\overleftarrow{\rho}$  (or resistance  $R_{ij}$ ) is in general the quantity of choice. The electric field  $\mathbf{E}$  (or voltage drop  $U_i$ ) is determined under the application of a constant current density  $\mathbf{j}$  (current  $I_j$ ):  $\mathbf{E} = \overleftarrow{\rho} \cdot \mathbf{j}$  ( $U_i = R_{ij} \cdot I_j$ ). To obtain the conductivity  $\overleftarrow{\sigma}$  from the resistivity  $\overleftarrow{\rho}$  the tensorial character of both quantities has to be taken into consideration

which means that the longitudinal resistivity contains both longitudinal and transverse conductivity contributions and vice versa. Commonly, the impact of these contributions strongly depends on the system under investigation.

The longitudinal resistivity  $\rho_{xx}$  and conductivity  $\sigma_{xx}$  has been measured independently in four point geometry as a function of magnetization orientation  $\mathbf{M}$  (see Sec. 3.3.2). The longitudinal conductivity  $\sigma_{xx}$  (i.e. electric current) was determined applying a fixed voltage:  $j_x = \sigma_{xx} \cdot E_x$ . For a Pt/Co/Pt wire with  $t_{\text{Co}} = 0.8$  nm both,  $\rho_{xx}$  and  $1/\sigma_{xx}$ , are plotted in Fig. 3.20. As both curves are the same within the uncertainty of the experiment for in-plane as well as out-of-plane rotation of  $\mathbf{M}$  it is obvious that the two quantities  $\rho_{xx}$  and  $\sigma_{xx}$  have a scalar character, thus  $\rho_{xx} = 1/\sigma_{xx}$ .

#### 3.4.4 Separation of Nernst contributions from the longitudinal magneto-thermopower

*Apart from some extensions this section closely follows the written elaboration in the Supplemental Material of my own publication, i.e., Ref. [90].*

In any kind of transport measurement transverse effects are generally superimposed on longitudinal effects and vice versa. This is due to slight deviations from the ideal sample geometry and a finite resistivity of the contacting leads that results in non-vanishing potential differences in the transition area of sample and contact leads. In case of MTEP measurements the superposition is more complex than for MR measurements. While in the latter case a constant current / voltage can easily be realized, a three dimensional temperature gradient  $\nabla T(\mathbf{r})$  has to be expected in any kind of experimental MTEP investigation. As a consequence, contributions of anomalous and ordinary Nernst effect (ANE and ONE) [14] (see Sec. 2.2.2)

$$\mathbf{E}_N = \underbrace{-N_0\mu_0\mathbf{H} \times \nabla T}_{\text{ONE}} - \underbrace{N_S\mu_0\mathbf{M} \times \nabla T}_{\text{ANE}} \quad (3.8)$$

show up in the signal of longitudinal MTEP.  $N_0$  and  $N_S$  are material-dependent Nernst coefficients. The Nernst effects can be easily separated from the longitudinal MTEP utilizing symmetry considerations. According to Onsager's reciprocal theorem the longitudinal MTEP (and MR) effects and the leading terms of the transverse effects, i.e., the Nernst (and Hall) effects, exhibit axial- and point-symmetry, respectively, as a function of field/magnetization [33, 34, 32]. Hence, the longitudinal MTEP signal corrected by Nernst effects can be simply determined by  $U_x^{\text{corrected}}(\mathbf{H}, \mathbf{M}) = (U_x(\mathbf{H}, \mathbf{M}) + U_x(-\mathbf{H}, -\mathbf{M}))/2$ . Moreover, the transverse voltage contributions  $U_x^{\text{parasitic}}(\mathbf{H}, \mathbf{M}) = (U_x(\mathbf{H}, \mathbf{M}) - U_x(-\mathbf{H}, -\mathbf{M}))/2$  allow for conclusions about the existing temperature gradient  $\nabla T(\mathbf{r})$  as shown in the following for the Pt/Co(2 nm)/Pt sample.

### 3 Experimental details

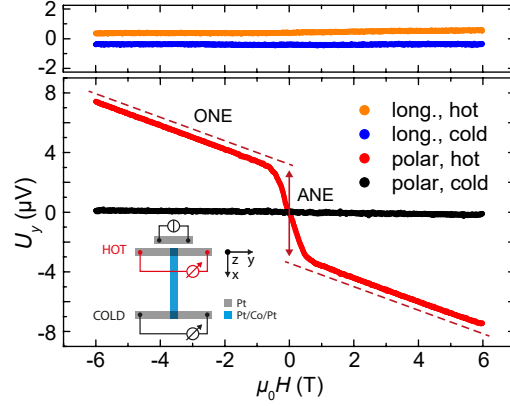


**Figure 3.21:** Transverse MTEP versus field. In the upper graph  $U_y$ , measured at the cold (blue) and hot (orange) end of the wire, is plotted versus the longitudinal field ( $\mathbf{H} \parallel x$ ). In the lower panel the same measurements (black/red) are shown for polar fields ( $\mathbf{H} \parallel z$ ). For the sake of clarity the orange and blue curves are shifted up- and downwards, respectively. A sketch of the experimental setup is given as inset.

#### Detailed investigation of the parasitic Nernst effects in the longitudinal magneto-thermopower

In this section the investigation on the parasitic Nernst contributions in the longitudinal MTEP is presented. Beforehand, the transverse MTEP behavior is discussed to reveal information about the existing temperature gradients. In order to qualitatively check for the (average) temperature gradient  $\frac{\partial T}{\partial x}(x)$  the transverse voltage  $U_y$  is measured simultaneously at both the hot and cold contacting area. In Fig. 3.21  $U_y$  for hot/cold contacts are plotted versus field applied along the film normal ( $\mathbf{H} \parallel z$ ). The transverse voltage  $U_{y,\text{hot}}(H_{\text{polar}})$  shows the features of a hard-axis magnetization curve generated by ANE (see Sec. 3.3.4). As an ANE effect that originates from the Co layer is observed, it follows that the Pt leads (thickness = 60 nm) do not act as short-circuit between the edges of the wire (left/right). Plotted on the same scale,  $U_{y,\text{cold}}$  appears constant which implies that  $\frac{\partial T}{\partial x}(x)$  is much smaller in larger distances from the heater, as expected for a bulk substrate (see Sec. 3.3.4). In a longitudinal field sweep ( $\mathbf{H} \parallel x$ ),  $U_{y,\text{hot}}$  as well as  $U_{y,\text{cold}}$  are almost equal and constant (see blue and orange curve in Fig. 3.21) meaning that the change of temperature in the Pt/Co/Pt stacking direction  $\frac{\partial T}{\partial z}$  is negligibly small.

Fig. 3.22(a) shows the measured longitudinal voltage  $U_x$  versus polar field  $H_{\text{polar}}$  taken simultaneously from the right- and left-hand edge of the wire (black and red curve). Considering point-symmetry, the parasitic Nernst contributions are determined as  $U_{x,i}^{\text{parasitic}}(H_{\text{polar}}) = (U_{x,i}(H_{\text{polar}}) - U_{x,i}(-H_{\text{polar}}))/2$ ,  $i = (\text{left}, \text{right})$  (see black and red curve in Fig. 3.22(b)). The curve in Fig. 3.22(c) depicts the longitudinal MTEP signal that is corrected by the Nernst contributions. The

### 3.4 Supplementary investigations

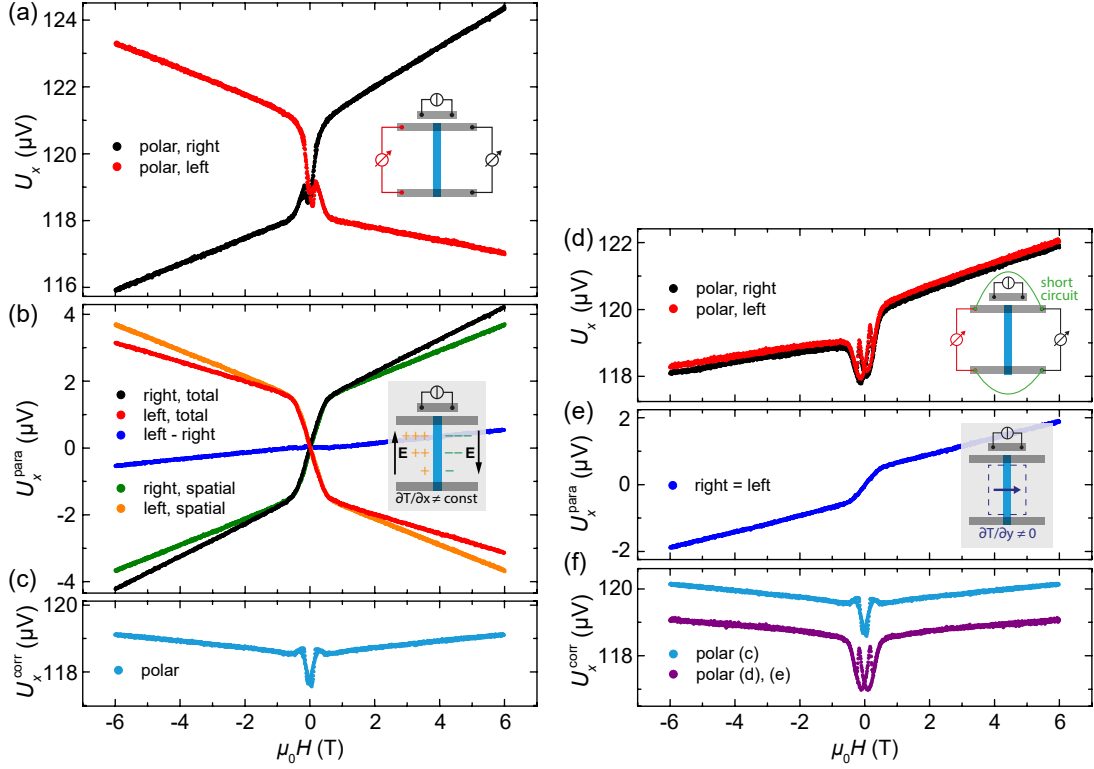


**Figure 3.22:** (a) - (c) Longitudinal MTEP vs polar field ( $\mathbf{H} \parallel z$ ). (a)  $U_x(H_{\text{polar}})$  taken at the left (black) and right side (red) of the Co/Pt wire. The inset shows the experimental setup. (b) The black and the red curve show the Nernst contributions in  $U_x(H_{\text{polar}})$  determined from the measurements in (a) according to  $(U_{x,i}(H_{\text{polar}}) - U_{x,i}(-H_{\text{polar}}))/2$ ,  $i = (\text{left}, \text{right})$ . The green and orange curves show the Nernst contributions which are opposite at the left and right side as a consequence of the spatial-dependent Nernst effect in the Co/Pt wire (see 1. in the text). The sketch depicts the spatial dependent Nernst effects with the resulting electric fields  $\mathbf{E}$  along the wire edges. The blue curve resembles the parasitic Nernst contributions that are the same at the left and the right side of the Co/Pt wire (see 2. and 3. in the text). (c) Corrected longitudinal MTEP  $U_{x,\text{corrected}}(H_{\text{polar}}) = (U_x(H_{\text{polar}}) + U_x(-H_{\text{polar}}))/2$  for the data of plot (a) after removing the Nernst contributions.

(d) - (f) Longitudinal MTEP vs polar field ( $\mathbf{H} \parallel z$ ) with short-circuited left and right side of the Co/Pt wire, including a sketch of the experimental arrangement. (d)  $U_x(H_{\text{polar}})$  taken at the left (black) and the right side (red) of the Co/Pt wire. (e) Calculated Nernst contributions  $(U_x(H_{\text{polar}}) - U_x(-H_{\text{polar}}))/2$  to  $U_x(H_{\text{polar}})$  utilizing the data shown in (d). The sketch emphasizes the fact that this contributions arises from a temperature gradient  $\frac{\partial T}{\partial y}(y)$  between the contacting leads (dashed box). (f) The purple curve shows the corrected longitudinal MTEP  $U_{x,\text{corrected}}(H_{\text{polar}}) = (U_x(H_{\text{polar}}) + U_x(-H_{\text{polar}}))/2$  for the data of plot (d) after removing the Nernst contributions. For comparison the corrected signal obtained from the measurements without short-circuiting is shown (cyan curve; data from (c)). For the sake of clarity the cyan curve is shifted by 1  $\mu\text{V}$ .

### 3 Experimental details

corrected signal is obtained from the data of Fig. 3.22(a) by  $U_x^{\text{corrected}}(H_{\text{polar}}) = (U_{x,i}(H_{\text{polar}}) + U_{x,i}(-H_{\text{polar}}))/2$ ,  $i = (\text{left}, \text{right})$ .

The parasitic signals  $U_{x,i}^{\text{parasitic}}(H_{\text{polar}})$  consist of the following three contributions:

1. The fact that  $\frac{\partial T}{\partial x}(x)$  is not constant (see above) causes spatial-dependent Nernst contributions, i.e., a varying transverse voltage along the Co/Pt wire that yields a longitudinal potential difference (see electric field vectors  $\mathbf{E}$  in the sketch of Fig. 3.22(b)). In case of a positive magnetic field this gradient of negative/positive charge density at the left/right side of the wire causes a corresponding parasitic contribution to the measured longitudinal MTEP. Thus, the parasitic Nernst signal is of opposite sign for both longitudinal voltages  $U_{x,\text{right}}(H_{\text{polar}})$  and  $U_{x,\text{left}}(H_{\text{polar}})$ . These parasitic contributions  $U_{x,\text{right}}^{\text{parasitic}}(H_{\text{polar}})$  and  $U_{x,\text{left}}^{\text{parasitic}}(H_{\text{polar}}) = -U_{x,\text{right}}^{\text{parasitic}}(H_{\text{polar}})$  are plotted as green and orange curve in Fig. 3.22(b), respectively.

Further parasitic contributions to the longitudinal voltage  $U_x(H_{\text{polar}})$  exist (blue curve in Fig. 3.22(b)), which are the same on both sides ( $U_{x,\text{right}}(H_{\text{polar}})$  and  $U_{x,\text{left}}(H_{\text{polar}})$ ). The latter signal is due to:

2. The fact that  $\frac{\partial T}{\partial x}(x)$  is not constant results in further spatial-dependent Nernst effects in the contacting leads as well as from the transition areas between leads and Co/Pt wire. Thus, a complex superposition of ONE and ANE contributions occurs in the measured longitudinal MTEP.
3. A temperature gradient along the  $y$ -direction  $\frac{\partial T}{\partial y}(y)$  exists, which comes from some symmetry breaking of the setup, i.e., a misalignment of heater with respect to the symmetry axis defined by the Pt/Co/Pt wire.

The latter two contributions can be separated by a shunting of the right and left edges of the Pt/Co/Pt wire. The short-circuit eliminates the contributions that are connected with a varying  $\frac{\partial T}{\partial x}(x)$  (1. and 2.). Experimentally, the short-circuit is realized by means of 25  $\mu\text{m}$  thick Al wires (see sketch in Fig. 3.22(d)). In other words, the Al wire eliminates the voltage drop in  $U_{y,\text{hot}}(H_{\text{polar}})$  (not shown) that showed up in Fig. 3.21 (discussed above). The  $U_{x,\text{right/left}}(H_{\text{polar}})$  curves for a polar field sweep are shown in Fig. 3.22(d). It is obvious that both curves are equal, which proves the elimination of the spatial-dependent Nernst signals in the measured longitudinal MTEP signal. The still present small parasitic transverse MTEP signal  $(U_{x,i}(H_{\text{polar}}) - U_{x,i}(-H_{\text{polar}}))/2$ ,  $i = (\text{left}, \text{right})$  (Fig. 3.22(e)) arises from the temperature gradient along the  $y$ -direction  $\frac{\partial T}{\partial y}(y)$  in the region of the Pt/Co/Pt wire between the contacting leads (see dashed box in the sketch of Fig. 3.22(e)).

The longitudinal MTEP signal corrected by Nernst effects ( $U_x^{\text{corrected}}(H_{\text{polar}}) = (U_{x,i}(H_{\text{polar}}) + U_{x,i}(-H_{\text{polar}}))/2$ ) is depicted in Fig. 3.22(f) (purple curve) and is very similar to the plot in Fig. 3.22(c). Note that the deviation between both

### 3.4 Supplementary investigations

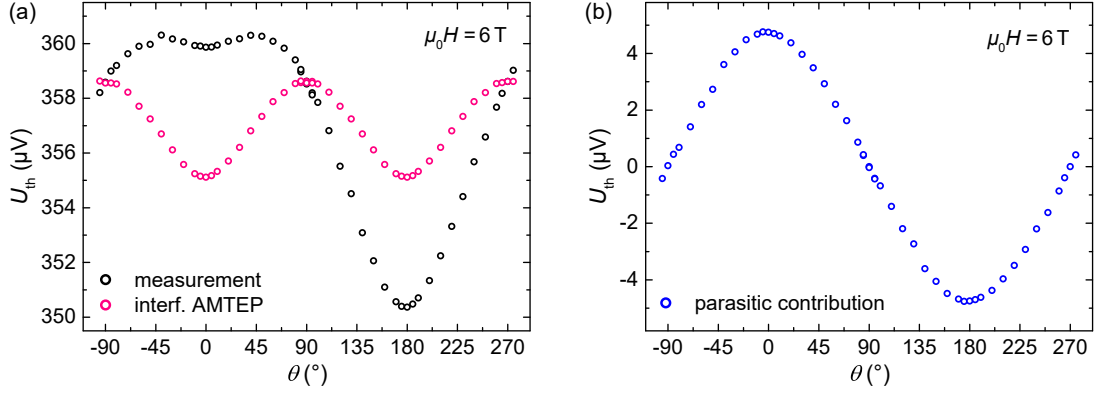


**Figure 3.23:** Longitudinal thermovoltage in dependence on the out-of-plane orientation of magnetization (see Sec. 3.2.2) for  $t_{\text{Co}} = 6$  nm. The directly measured signal  $U_x(\theta)$  and the corrected  $\cos^2 \theta$  signal of the interface AMTEP are plotted in (a). The parasitic  $\cos \theta$  contribution extracted from the directly measured curve is given in (b).

$U_x^{\text{corrected}}(H_{\text{polar}})$  curves around 0 T is due to a slightly different alignment of the sample with respect to the external magnetic field.

Certainly, the parasitic Nernst signals are also present in the out-of-plane magnetization rotation  $U_x(\theta)$  in the form of a superimposed  $\cos \theta$  dependence, which can be distinguished straight forwardly from the  $\cos^2 \theta$  signal of the longitudinal interface AMTEP. Exemplary for  $t_{\text{Co}} = 6$  nm, the directly measured signal for a rotation measurement as well as the disentangled interface AMTEP are depicted in Fig. 3.23(a) while (b) shows the effective parasitic Nernst contribution.

In contrast to the above problems with polar orientation of field the experiments with in-plane orientation of the field do not show any parasitic Nernst contributions within the uncertainty of the experiment of  $0.1 \mu\text{V}$  ( $2 \text{ nV/K}$ ).



## 4 Longitudinal magnetoresistance & magneto-thermoelectric power

In this chapter the in-plane and out-of-plane effects in the longitudinal MR and MTEP measurements are discussed in dependence on the Co thickness of the Pt/Co/Pt samples. This particularly serves the purpose of disentangling and characterizing the various effects.

The Sec. 4.1 is concerned with the thickness dependence of the directly measured magnitudes of the difference resistivities  $\Delta\rho_{\text{ip}}$  and  $\Delta\rho_{\text{op}}$ , followed by the correction of the effects for the influence of the current shunting (4.1.1) which occurs due to the nature of the layered structure of the samples. This is essential to be able to evaluate the pure MR effects sizes originating from the Co and Co/Pt interfaces.

In Sec. 4.2 the in-plane and out-of-plane MTEP effects  $\Delta S_{\text{ip}}$  and  $\Delta S_{\text{op}}$  directly obtained from the rotation measurements in dependence on the Co thickness  $t_{\text{Co}}$  are presented. Similar to the MR investigations, the layer composition of the samples strongly influences the overall measured thermopower, too. The developed model to account for this behavior of different shunting and weighting of the Seebeck coefficients in dependence on the thickness of Pt and Co is given in Sec. 4.2.1. Again, this yields the acquisition of the genuine effect sizes which are presented in Sec. 4.2.2. After the shunt correction the MR and MTEP results are compared, especially regarding the relative scaling of the interface and bulk effects.

In the last section (4.3) of this chapter a look is taken on the preliminary investigation on the spin-disorder MR and its thermoelectric analog.

### 4.1 Thickness dependence of magnetoresistance effects

The thickness dependence of the MR effects in Co/Pt layered systems, especially the AMR and AIMR effects, have been thoroughly investigated over the last years [40, 82, 17, 20]. For the sake of completeness the results of the investigated samples for this thesis are briefly summarized in this section.

The magnitudes of the in-plane MR effect  $\Delta\rho_{\text{ip}}$  and the out-of-plane MR effect  $\Delta\rho_{\text{op}}$ , i.e., the difference resistivities, are determined from the rotation measurements (see Sec. 3.3.2) for all samples with varying cobalt thickness  $t_{\text{Co}}$ . The results are depicted in Fig. 4.1(a). Note that the difference resistivities are calculated as  $\Delta\rho = \Delta R \cdot t_{\text{Co}} \cdot w/l$  where only the Co thickness instead of the overall

## 4 Longitudinal magnetoresistance & magneto-thermoelectric power

thickness  $t = t_{\text{Co}} + t_{\text{Pt}}$  of the wire is considered. This is a first approximation tracing back to the work of Kobs *et al.* [40, 82] to account for the fact that the MR effects originate from the ferromagnetic cobalt layer and is used here to maintain the comparability to earlier works. A full model also considering the changing current flow with changing  $t_{\text{Co}}$  will be addressed later.

The curve  $\Delta\rho_{\text{ip}}(t_{\text{Co}})$  characterizes the evolution of the AMR effect with rising Co thickness. Up to  $t_{\text{Co}} \approx 20$  nm this in-plane difference resistivity performs a gradual increase and then levels off to a more or less constant value (with a slight decrease for high  $t_{\text{Co}}$ ). The initial rising is mostly caused by the current shunting due to the Pt layers of the Co/Pt wire as for small  $t_{\text{Co}}$  the probe for the impact of the magnetization orientation, i.e., the current flowing through the Co, is noticeably reduced. For higher Co thicknesses this shunting is diminished and becomes almost insignificant so that the magnitude of the AMR effect merges into the constant bulk value.

For the curve  $\Delta\rho_{\text{op}}(t_{\text{Co}})$  where  $\mathbf{M}$  is altered in the plane perpendicular to the current flow direction the same reasoning regarding the current shunting applies but a qualitatively different behavior is observed. After a similar increase like in the AMR effect up to  $t_{\text{Co}} \approx 5$  nm the out-of-plane effect dependence on the thickness blends into a  $1/t_{\text{Co}}$  decline at  $t_{\text{Co}} \approx 10$  nm, reaching zero for high Co thicknesses. Kobs *et al.* argued that this functional dependence clearly implies that the underlying effect is connected to the interface-to-bulk ratio and, as it is still observable in the regime where current shunting plays a minor role, thus, reveals an interfacial effect, the anisotropic interface magnetoresistance (AIMR). Of course, this effect is always present if the properties of the interface do not change but is difficult to detect for high  $t_{\text{Co}}$  due to the decreasing fraction of electric current at the interfaces.

The investigations of the samples prepared in the course of this thesis do not show any hints in the  $\Delta\rho_{\text{op}}(t_{\text{Co}})$  curve for the presence of the geometrical size effect (GSE), a crystalline texture related effect. It was identified in Ref. [40], where the same Co/Pt system grown on  $\text{SiO}_2$  was used, as a constant negative offset with opposite sign compared to the AIMR effect. Although the substrate is similar to the here used glass it can be argued that the texture is less pronounced so that the GSE does not occur or is of smaller magnitude as  $\Delta\rho_{\text{op}}(t_{\text{Co}})$  does not show a sign reversal in the investigated range.

A different and probable assumption is that the GSE is present for the samples with  $t_{\text{Co}} \leq 30$  nm but cannot be distinguished from the AIMR effect as in this range the interface effect is of higher magnitude than the GSE. As a consequence, only for  $t_{\text{Co}} = 50$  nm the GSE would be absent. A hint to support this assumption may be found in the presumably changed crystalline growth for this sample deduced from the deviation of magnetic anisotropy compared to the other samples, see Sec. 3.1.3. A further indication of the change of the sample properties for  $t_{\text{Co}} = 50$  nm could be the rather distinct drop of the AMR effect size of this sample.

## 4.1 Thickness dependence of magnetoresistance effects

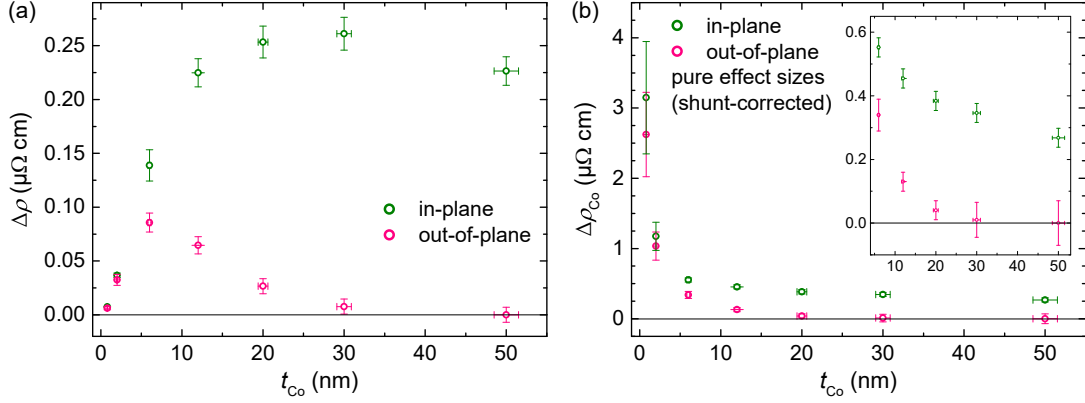


**Figure 4.1:** (a) Difference resistivities  $\Delta\rho_{\text{ip}}$  and  $\Delta\rho_{\text{op}}$  as a function of the cobalt thickness  $t_{\text{Co}}$ . The values are obtained from the in-plane and out-of-plane rotation measurements, see Sec. 3.3.2. (b) Pure thickness-dependent in-plane and out-of-plane effect sizes  $\Delta\rho_{\text{Co,ip}}(t_{\text{Co}})$  and  $\Delta\rho_{\text{Co,op}}(t_{\text{Co}})$  calculated (see Sec. 4.1.1) from the data plotted in (a), the inset shows the data for high  $t_{\text{Co}}$ . The curves reveal the existence of interface contributions to both the AMR and AIMR effect. Data from Ref. [89].

However, as the growth for  $t_{\text{Co}} = 50$  nm is argued to tend towards *hcp* this would mean an even higher effect size of the GSE (2.1.1) which in turn would mean a less pronounced texture for this sample to explain the observed behavior.

### 4.1.1 Correction for shunting (MR)

The results presented above are the difference resistivities directly determined from the measurements. As the fraction of the current flowing through the Co layer varies with  $t_{\text{Co}}$  when a constant current is impressed in the sample, the magnitude of the MR effects in the cobalt are not accessible via a direct measurement. However, it is possible to calculate the genuine effect sizes by the use of a parallel current model describing the current in the Pt and Co layers in combination with a Fuchs-Sondheimer modeling to account for the scattering at the Co/Pt interfaces. More details can be found in Refs. [20, 89]. The intrinsic effect sizes  $\Delta\rho_{\text{Co,ip}}(t_{\text{Co}})$  and  $\Delta\rho_{\text{Co,op}}(t_{\text{Co}})$  are plotted in Fig. 4.1(b). Both curves for the pure in-plane and out-of-plane MR effects show the functional dependence of  $1/t_{\text{Co}}$ . In the case of the AIMR effect this is expected following the reasoning given above and emphasizes that the effect originates from the Co/Pt interfaces.

That the pure AMR effect qualitatively exhibits the same behavior was not foreseeable from the directly measured values (see Fig. 4.1(a)) and obviously reveals that the AMR in Pt/Co/Pt does not solely occur as a bulk effect of a constant magnitude. More precisely, the  $1/t_{\text{Co}}$  dependence of  $\Delta\rho_{\text{Co,ip}}(t_{\text{Co}})$  provides evidence of interfacial contributions to the AMR as well due to inversion symmetry

## 4 Longitudinal magnetoresistance & magneto-thermoelectric power

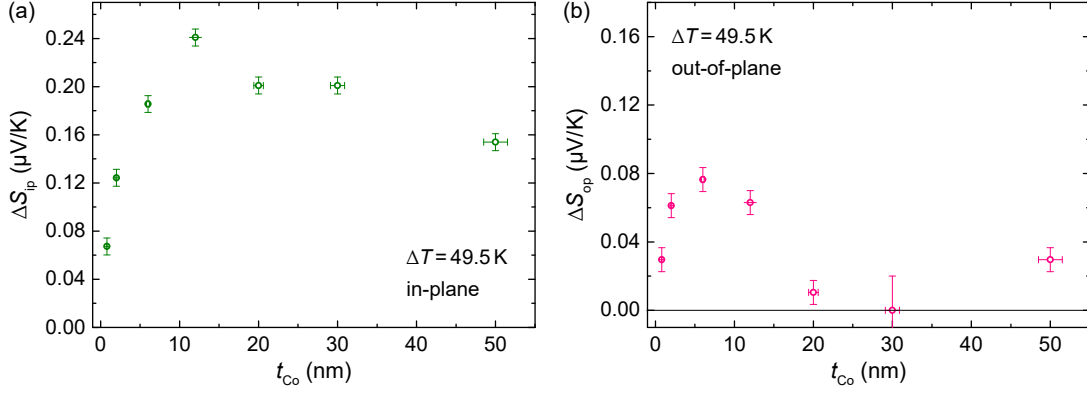


**Figure 4.2:** Difference thermopower in dependence on the Co thickness for the (a) in-plane,  $\Delta S_{\text{ip}}$ , and (b) out-of-plane,  $\Delta S_{\text{op}}$ , variation of  $\mathbf{M}$ . The data is directly obtained from the rotation measurements presented in Sec. 3.3.2. The general resemblance to the MR results stands out. The deviation at  $t_{\text{Co}} = 50$  nm (also visible in MR) may be due to the sample properties and a superposition of large parasitic effects in the original measurement, respectively. Data from Ref. [89].

breaking at the interfaces<sup>1</sup>, as stated by Kobs *et al.* in Ref. [20]. Another reasoning assumes AMR contributions from the CoPt interdiffusion areas at the interfaces of different magnitude than from the bulk-like Co area. This would lead to a non-constant  $\Delta\rho_{\text{Co,ip}}(t_{\text{Co}})$ , even after the shunt correction, as the current density at the interdiffusion zones would change with  $t_{\text{Co}}$ .

Additionally, the decrease of the pure AMR effect sizes with rising Co thickness could point to changing structural properties of the cobalt which impact would be superimposed to the above described effects. These changes could for example concern the interfaces, the crystalline strain [106, 107] or static defects of the system [40]. However, the latter, strongly influencing the absolute AMR effect size, is unlikely to change between samples for a consistent preparation procedure, although it could explain the rather distinct drop of  $\Delta\rho_{\text{ip}}$  for the wire with  $t_{\text{Co}} = 50$  nm.

### 4.2 Thickness dependence of magneto-thermoelectric effects

Similar to the presentation of the MR results in Sec. 4.1 this section deals with the thickness dependence of the MTEP effects which were determined from the amplitudes  $\Delta S_{\text{ip}}$  and  $\Delta S_{\text{op}}$  of the rotation measurements for different Co thicknesses  $t_{\text{Co}}$ , see Sec. 3.3.2. The curves for both the (a) in-plane and (b) out-of-plane variation of  $\mathbf{M}$  are depicted in Fig. 4.2.

<sup>1</sup>These contributions were modeled with a semi-classical Boltzmann approach taking (interfacial) Bychkov-Rashba spin-orbit interaction into account [105].

## 4.2 Thickness dependence of magneto-thermoelectric effects

As the thermopower  $S$  is proportionally related with the electrical resistivity  $\rho$  (see Eq. 2.18) the clear resemblance of the MTEP effect curves  $\Delta S_{\text{ip}}(t_{\text{Co}})$  and  $\Delta S_{\text{op}}(t_{\text{Co}})$  with the ones obtained from the MR investigations does not surprise. The anisotropic magneto-thermoelectric power (AMTEP; see Fig. 4.2(a)) also gradually rises with increasing  $t_{\text{Co}}$  and then, after a slight decrease, levels off to a constant value at higher thicknesses. Again, shunting effects are superimposed on the curve dominating its general shape. This is a consequence of the Pt layers of the Pt/Co/Pt wire which, beside the Co, act as additional sources of thermovoltage and have a varying influence on the overall thermopower when the Co thermovoltage changes for a variation of the magnetization. The impact of the shunting and weighting of the Seebeck coefficients is discussed in Sec. 4.2.1. The drop of  $\Delta S_{\text{ip}}$  at  $t_{\text{Co}} = 50$  nm is very likely to be caused by deviations of the sample properties as already discussed in the context of the MR results.

The  $\Delta S_{\text{op}}(t_{\text{Co}})$  curve mainly represents the evolution of the interface AMTEP with Co thickness, see Fig. 4.2(b). The increasing values for low  $t_{\text{Co}}$  followed by a  $1/t_{\text{Co}}$  decay for higher  $t_{\text{Co}}$  are comparable to the AIMR whereby the curve underlies the same shunting effects like for the in-plane measurements. However, the data for  $t_{\text{Co}} \geq 20$  nm is not as convincing as for the MR measurements. This is due to the large parasitic effects (see Sec. 3.4.4) in the out-of-plane rotations for high Co thicknesses which distinctly exceed the effect signal. While for  $t_{\text{Co}} = 20$  nm and 30 nm the values of  $\Delta S_{\text{op}}$  are still reasonable, there is no evident explanation why the value at 50 nm is distinctly larger than zero, especially, as in the MR rotation no effect was detectable. This is dissatisfying, nevertheless not of great importance because these results are rather caused by the uncertainty of the experiment or structural influences than point to general deviations of the AIMR behavior in the thermopower at large thicknesses. It is more significant that the reliable results for lower Co thicknesses do not present doubts for the assumption that the finding of a different scaling of interface and bulk effects in the MR and MTEP (see Sec. 3.3.3) is valid. For the further discussion see Sec. 4.2.2.

### 4.2.1 Modeling of magneto-thermoelectric effects

In Section 3.3.3 it was pointed out that the layered structure of the Pt/Co/Pt system is very likely to disguise the magnitude of the MTEP effects that originate from the Co layer. This would lead to deviations between the directly measured values for  $\Delta S_{\text{ip}}$  and  $\Delta S_{\text{op}}$ , and the genuine effect sizes. In order to rule out that the finding of the distinctly different slopes of the  $S(\rho)$  curves for the in-plane and out-of-plane magnetization effects are only artificial due to the composition of the samples, a modeling taking the layered nature into account is presented in the following.

The Figure 4.3 shows a simplified circuit diagram for the MTEP measurements. When a temperature difference is present in the setup each involved material acts

#### 4 Longitudinal magnetoresistance & magneto-thermoelectric power

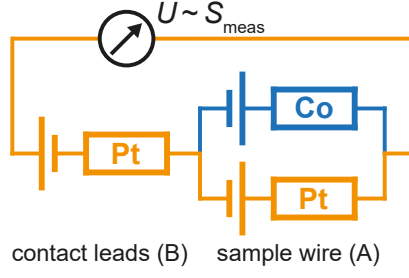


**Figure 4.3:** Simplified circuit diagram of the MTEP measurements. When a temperature difference is present each involved material acts like a voltage source with a certain internal resistance defining its *absolute* thermopower. The difference of the absolute thermopowers of the Pt contacting structure (B) and the Co/Pt wire (A) is the relative thermopower  $S_{\text{meas}}$  calculated from the measured thermovoltage  $U_{\text{th}}$ . If the same material is used for A and B the generated voltage drops in A and B will be of opposite sign (measured thermovoltage is zero).

like a voltage source with a certain internal resistance which defines its *absolute* thermopower. The difference of the absolute thermopowers of this so-called thermocouple consisting of the sample material A and contacting / reference material B is the measured thermopower  $S_{\text{meas}}$ , defined as [54, 1, 55]

$$S_{\text{meas}} = \lim_{\Delta T \rightarrow 0} \left( \frac{-U_{\text{th}}}{\Delta T} \right) = S_A - S_B . \quad (4.1)$$

In the case of a Pt/Co/Pt wire (material A) contacted by Pt leads (material B) the thermopower  $S_{\text{meas}} \equiv S$  is given by the difference of the Seebeck coefficient of the wire  $S_{\text{Pt/Co/Pt}}$  and the leads  $S_{\text{Pt}}$ :

$$\begin{aligned} S &= S_{\text{Pt/Co/Pt}} - S_{\text{Pt}} \\ &= \frac{\sum_i S_i \sigma_i t_i}{\sum_i \sigma_i t_i} - S_{\text{Pt}} \\ &= \frac{S_{\text{Pt}} \sigma_{\text{Co}} t_{\text{Co}} - S_{\text{Co}} \sigma_{\text{Co}} t_{\text{Co}}}{\sigma_{\text{Pt}} t_{\text{Pt}} + \sigma_{\text{Co}} t_{\text{Co}}} \\ &= \underbrace{\frac{\sigma_{\text{Co}}(\mathbf{M}, t_{\text{Co}}) t_{\text{Co}}}{\sigma_{\text{Pt}} t_{\text{Pt}} + \sigma_{\text{Co}}(\mathbf{M}, t_{\text{Co}}) t_{\text{Co}}}}_{f(\mathbf{M}, t_{\text{Co}})} (S_{\text{Co}}(\mathbf{M}, t_{\text{Co}}) - S_{\text{Pt}}) \end{aligned} \quad (4.2)$$

with  $i = (\text{Co}, \text{Pt})$  and the electrical conductivities  $\sigma$ . The last three lines of this equation result from the consideration that the Co and Pt layers of the wire are connected in parallel whereat the seed and cap layer are combined as one Pt layer. As the lateral extent of the single layers is constant only a thickness dependence on  $t_{\text{Pt}} (= \text{const.})$  and  $t_{\text{Co}}$  occurs, regarding the dimensions of the system. The

## 4.2 Thickness dependence of magneto-thermoelectric effects

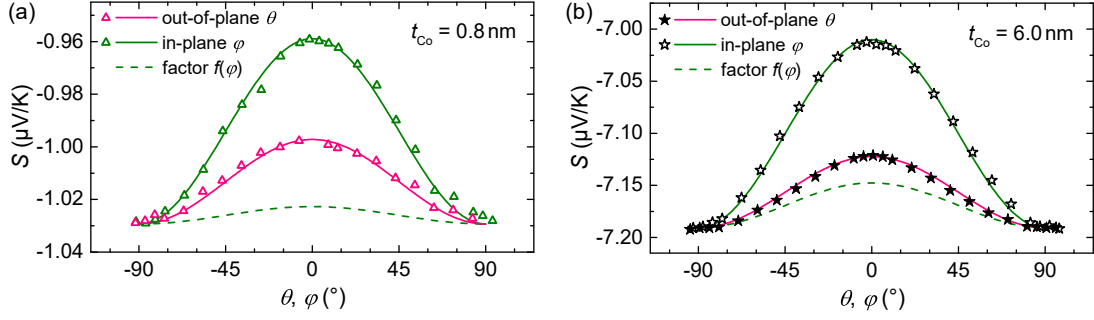


**Figure 4.4:** The measured thermopower  $S$  as a function of the in-plane and out-of-plane magnetization orientation for (a)  $t_{\text{Co}} = 0.8 \text{ nm}$  and (b)  $t_{\text{Co}} = 6 \text{ nm}$ , see also Sec. 3.3.2. The dashed green curve  $S(\varphi) = f(\varphi) \cdot A$  (with  $A = S_{\text{Co}} - S_{\text{Pt}} = \text{const.}$ ) reveals the angle dependence of the shunting and weighting impact of  $f$  when setting the thermopower for Co and Pt as independent of  $\mathbf{M}$ . The green and orange solid lines represent the fitting of Eq. 4.7 to the in-plane and out-of-plane data, respectively, revealing the parameters  $C_{\text{bulk}}$  and  $C_{\text{interf.}}$ , which ratio represents the relative scaling of the bulk and interface effects in the MR and MTEP. While the measured ratios  $a_{\text{int}}/a_{\text{bulk}} = 0.52 \pm 0.02$  ( $t_{\text{Co}} = 0.8 \text{ nm}$ ) and  $a_{\text{int}}/a_{\text{bulk}} = 0.63 \pm 0.02$  ( $t_{\text{Co}} = 6 \text{ nm}$ ), see Sec. 3.3.3, are distinctly different, the obtained shunt corrected values  $C_{\text{interf.}}/C_{\text{bulk}} = 0.47 \pm 0.04$  and  $0.51 \pm 0.03$  are similar within the error margins.

given expression holds for the assumption that the lateral temperature difference does not differ among the single layers, which is a good approximation as no traces of a perpendicular temperature gradient were found, see Fig. 3.21.

The magnetization dependence of the measured thermopower  $S$  is revealed by the fourth line of Eq. 4.2 and determined by the intrinsic  $\mathbf{M}$ -dependence of  $S_{\text{Co}}(\mathbf{M}, t_{\text{Co}})$  and the defined factor  $f(\mathbf{M}, t_{\text{Co}})$ , respectively. The latter describes the  $t_{\text{Co}}$ -dependent shunting of the thermovoltage in Co by the Pt layers as well as the  $\mathbf{M}$ -dependent weighting of electronic heat flow within the Pt/Co/Pt stack due to  $\sigma_{\text{Co}}(\mathbf{M})$ .

Note that the equalization of  $S_{\text{Pt}}$  in Eq. 4.2 only has an approximative character as the thermopower for the thin Pt of the wire and thick Pt of the contacting structure have different magnitudes, see Sec. 3.4.2. However, this has no influence on the correct determination of the difference thermopowers.

To describe and eliminate the impact of the magnetization and thickness dependent shunting and weighting effect on the MTEP measurements a correction model was developed, as presented in the following. At first, the attention is focused on the factor  $f(\mathbf{M}, t_{\text{Co}})$  of Eq. 4.2 to evaluate its influence.

The thicknesses  $t_{\text{Co}}$  and  $t_{\text{Pt}}$  are known from the sample preparation. The Pt conductivity  $\sigma_{\text{Pt}}$  (the same for all investigated wires) is obtained from the MR shunt modeling (4.1.1). Remembering that  $S = f \cdot A$  with  $A = (S_{\text{Co}} - S_{\text{Pt}})$  represents the modeling of the measured thermopower (Fig. 4.5(a)), in a temporary approximation  $A$  is set constant via the use of the bulk values  $S_{\text{Co}} = -20 \mu\text{V/K}$

#### 4 Longitudinal magnetoresistance & magneto-thermoelectric power

and  $S_{Pt} = -5 \mu\text{V}/\text{K}$  [1] which is motivated in the paper published in the course of this work [90] as the relative change of  $S$  with thickness is at least one order of magnitude smaller than for  $\sigma(t)$  [63]. By now, a more sophisticated modeling is used [89] that takes the thickness dependence of the thermopowers into account, see Fig. 4.5(b). In a next step  $\sigma_{Co}(\varphi = 0^\circ)$ , also obtained from the MR shunt modeling, is adjusted within its error margins to match the modeling  $f \cdot A$  to the actual measured  $S$  for the transverse orientation of the magnetization. To recapitulate, at this point the base value (transverse) of the MTEP rotation measurement fits the one of  $f \cdot A$ .

To account for the magnetization dependence of  $f(\mathbf{M}, t_{Co})$  the influence of the angle of magnetization on  $\sigma_{Co}(t_{Co})$  has to be considered. This is done by introducing the relations of the in-plane and out-of-plane MR rotations which are given by the following equation, whereat the indices for in-plane and out-of-plane rotation, and their corresponding angles are jointly written for simplicity.

$$\sigma_{Co}(\varphi, \theta) = \sigma_{Co,trans} - \Delta\sigma_{Co,ip,op} \cdot \cos^2(\varphi, \theta) . \quad (4.3)$$

As in the rotation measurements the difference resistivity is determined, not the difference conductivity, note  $\Delta\rho \neq (\Delta\sigma)^{-1}$ , the quantity  $\Delta\sigma_{Co,ip,op}$  in Eq. 4.3 has to be rewritten with this approximation [32]:

$$\Delta\sigma_{Co,ip,op} \approx \frac{\Delta\rho_{Co,ip,op}}{\rho_{Co}^2} = \Delta\rho_{Co,ip,op} \cdot \sigma_{Co}^2 . \quad (4.4)$$

The last step to accomplish the description of  $f(\mathbf{M}, t_{Co})$  in accordance with the measurements the shunt corrected (pure) magnitude  $\Delta\rho_{Co,ip,op}$  has to be inserted in Eq. 4.4 which is easily realized as these values are known from the MR shunt correction, see Fig. 4.1(b). The plot of  $S = f(\mathbf{M}, t_{Co}) \cdot A$  with  $A = \text{const.}$  is depicted in Fig. 4.4, exemplary revealing the impact of the shunting and weighting factor for  $t_{Co} = 0.8 \text{ nm}$  and  $6 \text{ nm}$ . It is obvious that  $f(\mathbf{M}, t_{Co})$  is of much smaller relative influence for the lower Co thickness.

In order to receive a full description of the measurement data the expression  $A = S_{Co}(\mathbf{M}, t_{Co}) - S_{Pt}$  which has been set constant so far is now characterized as magnetization dependent by

$$S_{Co}(\mathbf{M}, t_{Co}) = S_{Co,trans} + \Delta S_{Co,ip,op} \cdot \cos^2(\varphi, \theta) \quad (4.5)$$

representing the pure ( $S_{Co}$ ) impact of the angle dependence of the in-plane and out-of-plane rotations whereat  $\Delta S_{Co,ip,op}$  is still unknown. This term is substituted in Eq. 4.5 via the use of the Mott formula (Eq. 2.18) by

$$\Delta S_{Co,ip,op} = \underbrace{\frac{\pi^2 k_B^2 T}{3 e} \left[ \frac{\partial \sigma(E)}{\partial E} \right]_{E=E_F}}_{C_{\text{bulk,interf.}}^{\text{bulk,interf.}}} \cdot \Delta\rho_{Co,ip,op} \quad (4.6)$$

## 4.2 Thickness dependence of magneto-thermoelectric effects

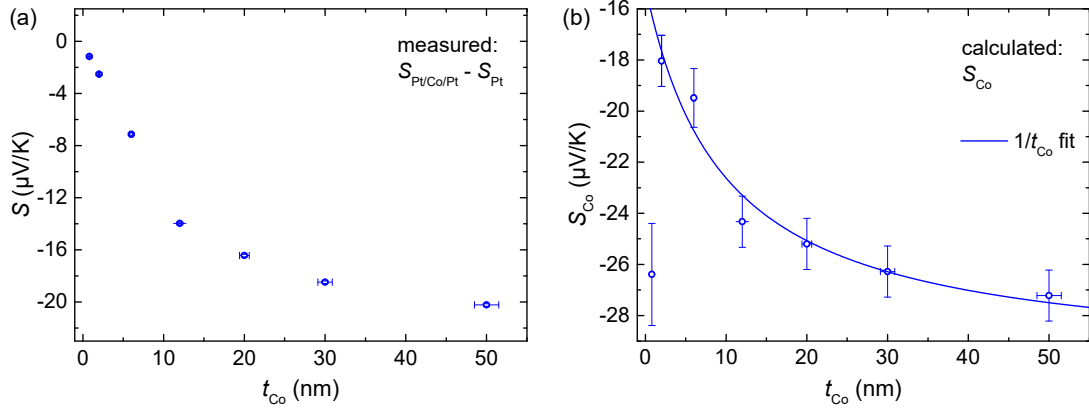


**Figure 4.5:** (a) The measured relative Seebeck coefficient  $S = S_{\text{Pt/Co/Pt}} - S_{\text{Pt}}$  in dependence on the Co thickness  $t_{\text{Co}}$ . The general shape is caused by the shunting effect of the Pt layer but also includes the impact of a non-constant  $S_{\text{Co}}(t_{\text{Co}})$ . For high Co thicknesses these effects decrease in their influence. (b) The absolute Seebeck coefficient  $S_{\text{Co}}$  as a function of  $t_{\text{Co}}$ . The values were calculated based on the data from (a) in course of the modeling of the MTEP measurements, see Sec. 4.2.1, by C. Erdmann [89]. The strong deviation for  $t_{\text{Co}} = 0.8$  nm are of acceptable impact on the determination of the pure effect MTEP sizes, see Fig. 4.6. It may be caused by the circumstance that for very thin films no complete bulk-like Co layer is developed for which the modeling does not account. Data from Ref. [89].

with  $C_{\text{interf.},\text{bulk}}$  including a constant prefactor and the specified derivative. With this last step the starting Eq. 4.2 describing the layered nature of the Co/Pt wires can be translated in

$$S(\varphi, \theta) = f(\varphi, \theta) \cdot \left( S_{\text{Co,trans}} + C_{\text{bulk,interf.}} \cdot \Delta\rho_{\text{Co,ip,op}} \cdot \cos^2(\varphi, \theta) - S_{\text{Pt}} \right) \quad (4.7)$$

where  $C_{\text{bulk}}$  and  $C_{\text{interf.}}$  are the fit parameters to model the in-plane and out-of-plane MTEP rotations, delivering the pure MTEP effect sizes  $\Delta S_{\text{Co,ip}}$  and  $\Delta S_{\text{Co,op}}$ . Additionally, the ratio of  $C_{\text{bulk}}$  and  $C_{\text{interf.}}$  indicates the scaling of the investigated bulk and interface effects between MR and MTEP, see Eq. 4.6. For  $t_{\text{Co}} = 0.8$  nm and 6 nm the full modeling of the MTEP rotation measurements is depicted in Fig. 4.4.

### 4.2.2 Correction for shunting (MTEP)

In the following the shunt corrected effect sizes of the AMTEP  $\Delta S_{\text{Co,ip}}$  and interface AMTEP  $\Delta S_{\text{Co,op}}$  are discussed. Beforehand, it was shown how these values were calculated and thus revealing their proportionality to the AMR effect via  $\Delta S_{\text{Co,ip}} = C_{\text{bulk}} \cdot \Delta\rho_{\text{Co,ip}}$  and likewise for the interface effect (Eq. 4.6).

The Figure 4.6(a) shows the results for  $\Delta S_{\text{Co,ip}}$  in dependence on the cobalt thickness  $t_{\text{Co}}$ . The qualitative behavior is very similar to the pure AMR effect,

#### 4 Longitudinal magnetoresistance & magneto-thermoelectric power

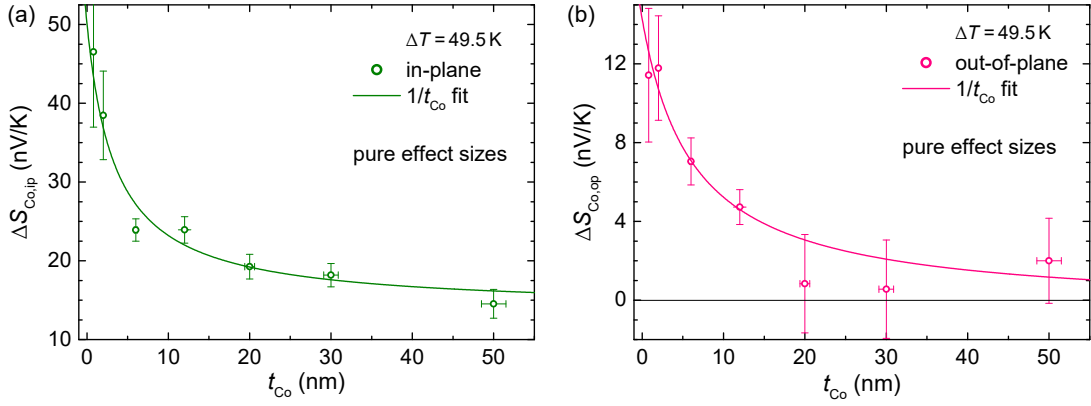


**Figure 4.6:** The pure difference thermopowers (a)  $\Delta S_{\text{Co,ip}}$  and (b)  $\Delta S_{\text{Co,op}}$  in dependence on the Co thickness  $t_{\text{Co}}$ . The values are calculated via the modeling (4.2.1) of the in-plane and out-of-plane MTEP rotation measurements and represent the shunt corrected values of the data in Fig. 4.2. The curves mainly reveal the genuine effect sizes of the (a) AMTEP and (b) interface AMTEP which can be fitted by a  $1/t_{\text{Co}}$ -decline. Thus, not only the interface effect but also the AMTEP shows contributions originating from the interfaces. For  $t_{\text{Co}} \geq 20$  nm the  $\Delta S_{\text{Co,op}}$  possess large error margins due to the small effect sizes combined with large parasitic Nernst contributions in the measured curves. Data from Ref. [89].

showing a  $1/t_{\text{Co}}$  functional dependence. The shape of the curve reveals that the AMTEP effect does not only occur as a constant bulk effect but also contains interface contributions which are especially visible for the thin film regime. Here, the same reasoning applies as in the case of the shunt corrected AMR results.

The out-of-plane difference thermopower  $\Delta S_{\text{Co,op}}$  as a function of  $t_{\text{Co}}$  is given in Fig. 4.6(b). A  $1/t_{\text{Co}}$ -dependence can describe the data, again, pointing to the proportionality of this effect to the out-of-plane MR effect  $\Delta\rho_{\text{Co,op}}(t_{\text{Co}})$ , see Fig. 4.1(b), and identifying it as an interface effect. The magnitude of the interface AMTEP for the sample with  $t_{\text{Co}} = 0.8$  nm tends towards a relatively low value compared to the fitted curve. This is very likely to be a consequence of the absolute thermopower  $S_{\text{Co}}$  for this sample what shows a clear deviation from the  $S_{\text{Co}}(t_{\text{Co}})$  curve (Fig. 4.5(b)) which was used for the modeling procedure. It can be argued that for very thin films no complete bulk-like Co layer is developed, not accounted for in the model. However, as the effect size is still of a reasonable magnitude it is evident that errors in the determination of the thickness dependence of  $S_{\text{Co}}$  are of small influence for the determination of the difference thermopowers. This was already mentioned in Sec. 4.2.1 where the approximative use of bulk values for  $S_{\text{Co}}$  and  $S_{\text{Pt}}$  in a previous modeling procedure was motivated.

The results of the out-of-plane difference thermopower in the regime  $t_{\text{Co}} \geq 20$  nm are not particularly convincing. While for  $t_{\text{Co}} = 30$  nm the value seems appropriate,  $\Delta S_{\text{Co,op}}$  appears to be too low at 20 nm and too high at 50 nm. The main

## 4.2 Thickness dependence of magneto-thermoelectric effects

reason for the uncertainty of this data showing large error margins originates from the superimposed contribution of parasitic Nernst effects in the original measurements (Sec. 3.4.4) gaining impact with  $t_{\text{Co}}$  in relation to  $\Delta S_{\text{Co,op}}$ . Moreover, at  $t_{\text{Co}} = 50 \text{ nm}$  there is no evidence for the presence of the GSE in the MR measurements, see Sec. 4.1, which was speculated to be caused by a differing crystalline growth compared to the other samples. In the out-of-plane difference thermopower, however, an effect size distinctly larger than zero was observed, which consequently translates into a signal visible in  $\Delta S_{\text{Co,op}}$ , too. Without any more data covering this range it is idle to give speculations on the behavior, e.g., a different impact of the GSE in the thermopower.

### 4.2.3 Comparison of shunt-corrected anisotropic MR & MTEP effects

In this section the pure difference resistivities  $\Delta\rho_{\text{Co,ip}}(t_{\text{Co}})$  and  $\Delta\rho_{\text{Co,op}}(t_{\text{Co}})$  and pure difference thermopowers  $\Delta S_{\text{Co,ip}}(t_{\text{Co}})$  and  $\Delta S_{\text{Co,op}}(t_{\text{Co}})$  are compared. According to the Mott formula (Eq. 2.16) the effects are predicted to show a proportional dependence. This was verified for the AMR and AIMR because the AMTEP and interface AMTEP exhibit the same qualitative behavior in the magnetic field dependent (3.3.1) and magnetization orientation dependent (3.3.2) measurements. As the prefactor  $\pi^2/3 \cdot k_{\text{B}}^2 T/e$  of the Mott equation is constant for all measurements, a first conclusion is that the derivative  $[\partial\sigma(E)/\partial E]_{E=E_{\text{F}}}$  is constant, too. From the uncorrected rotation measurements, however, and still after applying the correction model it was discovered that the derivative has to be different for the interface and bulk effects. In other words, the proportionality parameter  $C$ , containing this derivative, in  $\Delta S_{\text{Co}} = C \cdot \Delta\rho_{\text{Co}}$  is varying between bulk and interface and describes the different relative scaling of the effects originating there. This scaling is discussed in dependence on the Co thickness by evaluating the following expression for all samples:

$$\frac{C_{\text{interf.}}}{C_{\text{bulk}}} = \left[ \frac{\partial\sigma}{\partial E} \right]_{E=E_{\text{F}}}^{\text{interf.}} / \left[ \frac{\partial\sigma}{\partial E} \right]_{E=E_{\text{F}}}^{\text{bulk}} = \frac{\Delta S_{\text{Co,op}}}{\Delta\rho_{\text{Co,op}}} / \frac{\Delta S_{\text{Co,ip}}}{\Delta\rho_{\text{Co,ip}}} . \quad (4.8)$$

In the context with the rotation measurements the ratio of in-plane and out-of-plane effect sizes, i.e., the uncorrected  $C$ -ratio labeled with the slopes  $a$ , was already mentioned, exemplary, for the first three samples. For  $t_{\text{Co}} = 0.8 \text{ nm}$  the ratio is  $a_{\text{int}}/a_{\text{bulk}} = 0.52 \pm 0.02$ , while for the others  $0.53 \pm 0.02$  (2 nm) and  $0.63 \pm 0.02$  (6 nm) is obtained whereat the latter was argued to deviate because of shunting effects. To verify this assumption the ratios of the corrected  $C$ -values are compared. In case of  $t_{\text{Co}} = 0.8 \text{ nm}$  it is  $C_{\text{interf.}}/C_{\text{bulk}} = 0.47 \pm 0.04$ , for the other samples  $0.47 \pm 0.03$  (2 nm),  $0.51 \pm 0.03$  (6 nm), and  $0.52 \pm 0.03$  (12 nm). They are the same within the error margin and point to the general validity<sup>2</sup> of the finding.

<sup>2</sup>This is only valid for the assumption of  $\Delta\rho_{\text{Co,ip}} = \text{const.}$  (used in Ref. [90]) in the shunt modeling of MTEP effects. For details see the erratum.

#### 4 Longitudinal magnetoresistance & magneto-thermoelectric power

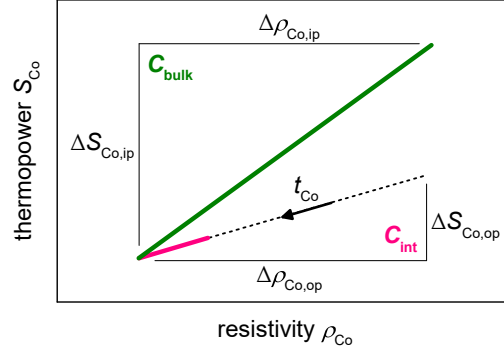


**Figure 4.7:** Sketch of thermopower  $S_{Co}$  over resistivity  $\rho_{Co}$  referring to Sec. 3.3.3. The linear curves (Mott formula) for the bulk effect (slope  $C_{\text{bulk}} \propto \Delta S_{Co,ip}/\Delta\rho_{Co,ip}$ ) and interface effect (slope  $C_{\text{interf.}} \propto \Delta S_{Co,op}/\Delta\rho_{Co,op}$ ) are depicted. The representation visualizes the difficulty to accurately determine the ratio  $C_{\text{interf.}}/C_{\text{bulk}}$  for high Co thicknesses  $t_{Co}$  where the interface effect tends to zero.

The results for the higher Co thicknesses  $t_{Co} = 20$  nm, 30 nm and 50 nm are 0.50, 0.50 and 0.51, respectively, but shall be disregarded as the errors exceed the values by at least the double magnitude of the values itself. A visual clarification why it is difficult to accurately determine the ratio for high  $t_{Co}$  is given in Fig. 4.7 where (similar to the representation in Sec. 3.3.3) the magnitudes of the bulk and interface effect characterize the slopes of the linear  $S_{Co,ip,op}(\rho_{Co,ip,op})$  curves. It is evident that the small signals of the interface effect for thick Co layers prevent to extract  $C_{\text{interf.}}/C_{\text{bulk}}$  within reasonable error margins.

Note that the dismissal of data for high Co thicknesses has no consequences regarding the claim of the general validity (thickness independent) of finding a different value of  $[\partial\sigma(E)/\partial E]_{E=E_F}$  for bulk and interface effects. This is due to the fact that the high thickness regime may not deliver reliable data but particularly does not contradict the finding. In addition, already in context with the directly measured results of  $a_{\text{int}}/a_{\text{bulk}}$  for the two lowest Co thicknesses, see Sec. 3.3.3, where no deviation between the ratios was found, a generality of the finding was assumed. This was motivated by receiving the same result for samples with different compositions of the layered structure in a regime where shunting is of little influence (see Sec. 4.2.1).

When thinking of the AMR and AMTEP, and the AIMR and interface AMTEP as localized probes for the properties of the areas where they originate, i.e., the Co bulk and the Co/Pt interface, respectively, then it can be concluded that the difference of  $C_{\text{bulk}} \propto [\partial\sigma(E)/\partial E]_{E=E_F}^{\text{bulk}}$  and  $C_{\text{interf.}} \propto [\partial\sigma(E)/\partial E]_{E=E_F}^{\text{interf.}}$  reveals the presence of different electronic (band) structures (see also Sec. 2.2.1) in the bulk and interface region.

### 4.3 Spin-disorder effects in MR & MTEP

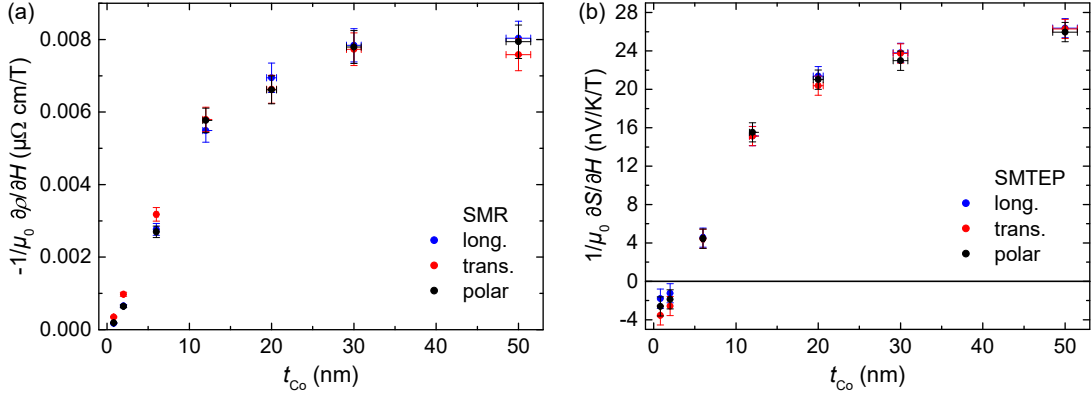


**Figure 4.8:** Effect sizes of the (a) SMR and (b) SMTEP in dependence on the Co thickness  $t_{Co}$ . The data is obtained as slopes from the field sweep measurements (3.3.1) in the regime of  $\mu_0|H| \gtrsim 2$  T, i.e.,  $-1/\mu_0 \cdot \partial\rho/\partial H$  (MR) and  $1/\mu_0 \cdot \partial S/\partial H$  (MTEP), for the three principle directions of the magnetic field orientation. The SMTEP effect performs a sign reversal between  $t_{Co} = 2$  nm and 6 nm.

## 4.3 Spin-disorder effects in MR & MTEP

In this section the preliminary results of the investigation on the spin-disorder MR (SMR), see Sec. 2.1.1, and its thermoelectric analog, the spin-disorder MTEP (SMTEP), are presented.

In simple terms, the SMR effect describes the field-dependent impact of the magnon spectrum of a ferromagnetic system on the longitudinal resistivity  $\rho$ . If an external magnetic field is applied the magnons (quasiparticles of the spin waves) are reduced in number which leads to a reduced resistivity as the number of scattering events of magnons and electrons decreases. The same reasoning applies for the influence on the thermopower  $S$ .

The SMR and SMTEP have an influence whenever an external field  $\mathbf{H}$  is present but the easiest way to determine the impact of the effects is to focus on the regime above technical saturation of the magnetization as other longitudinal magnetization effects are constant here. The magnitudes of the SMR and SMTEP are obtained from the field sweep measurements (Sec. 3.3.1) via the slopes of the curves for  $\mu_0|H| \gtrsim 2$  T. In dependence on the Co thickness the plots of  $-1/\mu_0 \cdot \partial\rho/\partial H$  (MR) and  $1/\mu_0 \cdot \partial S/\partial H$  (MTEP) are given in Fig. 4.8 for the three principle directions of the magnetic field orientation. The general shape of the two curves is very similar which again indicates the direct relation of the thermopower and the electrical resistivity as described by the Mott formula (Eq. 2.17). The qualitative behavior of an increase of the effect size with thickness whereas the rise is reduced for high  $t_{Co}$  to merge into a constant value is clearly dominated by the shunting effect of the Pt layers, as described before. While the shunt correction for the SMTEP has not been accomplished yet, the one for

#### 4 Longitudinal magnetoresistance & magneto-thermoelectric power

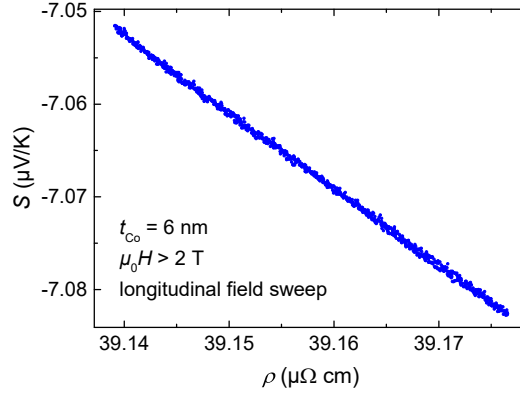


**Figure 4.9:** Electrical resistivity  $\rho$  plotted over the thermopower  $S$  at  $\mu_0|H| \gtrsim 2$  T (longitudinal field orientation) for a sample with  $t_{\text{Co}} = 6$  nm. The data is obtained from the field sweep measurements, see Sec. 3.3.1. The linear curve reveals the validity of the Mott formula for the relation between SMR and SMTEP effect.

the SMR can be found in Refs. [89, 108] which stand in context with this work. However, the here depicted results alone point to some interesting features when comparing the MR and MTEP.

It is very striking that the  $1/\mu_0 \cdot \partial S/\partial H$  curve performs a sign reversal between  $t_{\text{Co}} = 2$  nm and 6 nm which is not observed for the MR measurements. For the assumption that all the effects in  $\rho$  translate into the same behavior in  $S$  like can be seen for example for the field sweep measurements in Fig. 3.10 ( $t_{\text{Co}} = 0.8$  nm and 2 nm) the sign of the SMTEP for higher Co thicknesses is unexpected. A comparison to other works that are concerned with the thermopower of systems including Co in dependence on the magnetic field [74, 8], describing the anticipated behavior, endorses the odd nature of discovering a sign reversal. The shunting due to the Pt layers in the wire cannot be the reason for this behavior because a correction would only affect the magnitude of the effect size but not the sign. As pointed out in Ref. [89], although a violation of the Mott formula has been observed before, e.g., for a graphene systems at temperatures near the Dirac point [109, 110] this is very unlikely to provide insights for the described finding regarding the measurements on Co/Pt at room temperature. Another speculation [108] that the magnon drag effect [111, 1, 112] might offer a possible explanation by being suppressed for low  $t_{\text{Co}}$  and unfolding its impact for higher Co thicknesses is also questionable as the investigations are performed at high fields and room temperature [63, 22, 113, 114]. To hopefully establish more insights on this interesting finding the sign reversal of the SMTEP is under ongoing investigation.

In context with the field dependence (3.3.1) of the resistivity and thermopower, respectively, the isotropic high field behavior, meaning the independence of the SMR and SMTEP impact regarding the field orientation, was pointed out. It was also mentioned that this is an approximation, especially, in the case of the MR field

### 4.3 Spin-disorder effects in MR & MTEP

sweeps for low Co thicknesses where the anisotropic high field magnetoresistance (AHMR) [88] causes a slightly larger change of  $\rho$  with field for the transverse field orientation compared to the polar and longitudinal geometries. In the MTEP sweeps this effect only has been observed for  $t_{\text{Co}} = 0.8$  nm. However, when taking a look at the  $S(H)$  curve for  $t_{\text{Co}} = 2$  nm in Fig. 3.10 it is apparent that the slopes  $1/\mu_0 \cdot \partial S/\partial H$  are equal for polar and transverse orientation but here a deviation is found for the longitudinal curve. As a consequence, the plot of  $S$  over  $\rho$  in the high field regime, exemplary shown for one orientation and  $t_{\text{Co}} = 6$  nm in Fig. 4.9, exhibits a different slope for each the longitudinal, transverse and polar orientation of the magnetic field. As the  $S(\rho)$  representation illustrates the functional dependence of the Mott formula it follows the conclusion that the proportionality or scaling of the SMR and SMTEP effects is different depending on the field orientation, similar to the finding regarding the bulk (AMR and AMTEP) and interface (AIMR and interface AMTEP) effects discussed before. This topic is still under investigation, especially, regarding the evolution of the finding with the Co thickness. The data is already acquired, see Fig. 4.8, but for a reliable evaluation it would be desirable to reduce the errors and possibly extend the measurements to higher fields. Moreover, the accurate correction for parasitic (ordinary) Nernst effects in the MTEP measurements has to be minded.



## 5 Conclusion and outlook

The magnetoresistance (MR) and magneto-thermoelectric power (MTEP) effects of Pt/Co/Pt layered systems deposited on glass substrate were investigated in dependence on the cobalt thickness  $t_{\text{Co}}$ . The variation of  $t_{\text{Co}}$  for the wire shaped samples in the range of 0.8 nm to 50 nm had the main purpose to disentangle different effects from the measurements and to be able to evaluate and correct the shunting influence of the Pt layers on the electrical current (MR) and thermovoltage (MTEP) in the Co layer. For a quantitative analysis this is important in order to obtain the genuine magnetization dependent effect sizes that only originate from the ferromagnetic Co and Co/Pt interfaces.

In the course of the magnetoresistance investigations the known results on the anisotropic MR (AMR) and anisotropic interface MR (AIMR) [17, 18, 40, 20] effects were reproduced. The magneto-thermoelectric power measurements revealed the corresponding effects, namely, the AMTEP and interface AMTEP whereat the latter was firstly reported in literature as part of this work [90]. Due to Mott's description (Eq. 2.16) of the proportionality between the thermopower  $S$  and the electrical conductivity  $\sigma$  in the form of  $S = C \cdot 1/\sigma$  with  $C \propto [\partial\sigma/\partial E]_{E=E_{\text{F}}}$ , the energy derivative of the conductivity at the Fermi energy, the existence of these effects were anticipated.

The results of the in-plane (AMR) and out-of-plane (AIMR) magnetization variations were corrected regarding the shunting with the model presented in Ref. [20] yielding the pure effect sizes  $\Delta\rho_{\text{Co}}$ . For the MTEP measurements another model, considering the layered sample structure and partially deploying results from the MR model, was developed in the framework of this thesis to calculate the genuine effect sizes  $\Delta S_{\text{Co}}$  for the AMTEP and interface AMTEP. The comparison to the MR analogs via  $\Delta S_{\text{Co}} = C \cdot \Delta\rho_{\text{Co}}$  revealed a different scaling in thermopower and resistivity between the bulk and interface effect as  $C_{\text{bulk}} \neq C_{\text{interf.}}$ . This led to the conclusion that  $C_{\text{bulk}}$  and  $C_{\text{interf.}}$  reflect certain properties of the areas where the corresponding effects originate, namely the Co bulk and the Co/Pt interface. As  $C$  is proportional to  $[\partial\sigma/\partial E]_{E=E_{\text{F}}}$  which then is non-equal for interface and bulk, a difference in the band structure in these regions can be assumed. The combination of MR and MTEP measurements as localized probe for a certain magnetization dependent effect can be instrumentalized for other than the here presented effects, too, to gain knowledge on the electronic states. In order to evaluate if this is a realistic approach layer resolved first principal calculations of the electronic states (here, in the Co/Pt system) in dependence of magnetization

## 5 Conclusion and outlook

orientation would be helpful [115, 116]. Moreover, like stated in Ref. [90], a further contribution to the different values of  $C$  may arise from different strengths and types of the spin-orbit coupling effects causing the AMR and AIMR [117]. For a deeper understanding of the presented finding it could also be helpful to investigate other layered systems where the AIMR effect has been identified [41, 42, 43].

The confidence that the above discussed findings are robust is based on a number of additional measurements characterizing various properties of the investigated system that were performed to check for potential sources of errors. In the investigation on the thermopower  $S$  in dependence on the temperature difference  $\Delta T$  for different orientations of the magnetic field it was shown that the results of the AMTEP and interface AMTEP effect sizes are valid for a wide<sup>1</sup> range of  $\Delta T$ . This means that despite the temperature dependence of the Seebeck coefficients these values do not need any correction regarding the temperature difference applied to the system. Moreover, it has been found that the magnetization dependent  $S(\Delta T)$  curves present an accurate method to determine the MTEP effect sizes without the need of field sweep or rotation measurements.

While, experimentally, the MR investigations are rather simple, the fact that in the MTEP measurements the sample is exposed to locally varying temperatures adds a certain complexity. In the sample layout, for example, it has to be carefully considered if any material transitions act as unwanted sources of additional thermovoltages. More importantly, the three dimensional temperature gradient in the Co/Pt wire was qualitatively investigated and evaluated regarding its impact on the measurements. The gradient was identified as source of several parasitic contributions to the longitudinal thermopower due to the Nernst effects which were eliminated from the measurement data. In turn, just these Nernst effects could be utilized to determine the magnetic anisotropy of the samples.

Apart from the findings summarized above there are still some interesting observation that seem worth to be investigated further on. In context with the Nernst effect measurements it was pointed out that the ONE and ANE exhibit the same sign among each other whereas their corresponding MR effects are of opposite sign. This could indicate a varying translation of one of the Hall effects into its corresponding Nernst effect regarding the Mott formula. As a quantitative analysis of the  $\nabla T$ -dependent Nernst effects would certainly not hurt in resolving this matter, the temperature profile along the Co/Pt wire should be determined. For this purpose a special sample layout was designed. Another approach, though more challenging, would be the sample preparation onto a membrane which generally provides a spatially linear change of temperature (constant temperature gradient) so that a simple two-point calibration of  $T$  would suffice. This would also reduce the presence of the mentioned parasitic Nernst contributions to the longitudinal thermopower.

---

<sup>1</sup>Valid for a reasonable range of applied heating power with regard to the heat dissipation capabilities of the substrate.

Also yet without explanation is the observed sign reversal of the spin-disorder MTEP when changing the Co thickness, not existing in the MR. Here, a variation of the base temperature of the Co/Pt system and the application of higher magnetic fields, respectively, could be useful in order to check for the possible influence of drag effects on this finding. Although, the fact that the sign reversal occurred at room temperature makes an explanation by means of drag effects, normally present near  $T = 0$  K only, very unlikely.



# Erratum

Proof reading the manuscript of my thesis I noticed an inconsistency in the results of the shunt model for the magneto-thermoelectric measurements. This concerns the  $\Delta S_{\text{Co,ip}}(t_{\text{Co}})$  and  $\Delta S_{\text{Co,op}}(t_{\text{Co}})$  data in Fig. 4.6 provided by C. Erdmann in context with his master thesis [89]. Due to the erroneous fitting of the MTEP shunt model, in which wrong results of the MR shunt correction (see Sec. 4.1.1 and Refs. [20, 89]) were entered, the plotted effect sizes of the pure in-plane and out-of-plane MTEP do not yield a thickness independent ratio  $C_{\text{interf.}}/C_{\text{bulk}} \approx 0.5$  (Eq. 4.8) in combination with the pure MR effect data  $\Delta\rho_{\text{Co,ip}}(t_{\text{Co}})$  and  $\Delta\rho_{\text{Co,op}}(t_{\text{Co}})$  (Fig. 4.1(b)). In Sec. 4.2.3 the latter is wrongly stated. The resultant constant ratio is found to be only accurate for the assumption of  $\Delta\rho_{\text{Co,ip}} = \text{const.}$  (used in Ref. [90]). The recently developed modeling of the impact of shunting on MR effects [20], which distinctly reveals interface contributions to the AMR (not to be confused with the AIMR), seems to yield smaller  $C_{\text{interf.}}/C_{\text{bulk}}$  ratios. Due to time limitations I could manage to check the results for the smallest thicknesses only. The sample with a Co thickness of  $t_{\text{Co}} = 0.8 \text{ nm}$  turns out to produce meaningless values regarding the uncertainty due to the steep rise of the  $\Delta\rho_{\text{Co}}$  curves. For  $t_{\text{Co}} = 2 \text{ nm}$  the result is  $C_{\text{interf.}}/C_{\text{bulk}} \approx 0.2$ . In consequence of the smaller ratio, the shunting effect of the layered structure in the MTEP is larger for thin films than previously assumed. Moreover, the results of a preliminary fitting for other thicknesses reveal that  $C_{\text{interf.}}/C_{\text{bulk}} \neq \text{const.}$  and that the ratio increases with  $t_{\text{Co}}$ . The thickness dependence can be attributed to the fact that in  $C_{\text{bulk}}$  not only the bulk-like AMR is effective but the newly found interface contributions to the AMR are included via  $\Delta\rho_{\text{Co,ip}}$ , too.

Note that the considerations given above have no impact on the statement that the scaling of interface and bulk effects are different, meaning different magnitudes of the derivative  $[\partial\sigma(E)/\partial E]_{E=E_{\text{F}}}$  in the Mott formula. This in turn points to different electronic states in the Co bulk, Co/Pt interface and Co/Pt interdiffusion regions.



# Bibliography

- [1] F. J. Blatt, P. A. Schroeder, C. L. Foiles, and D. Greig, *Thermoelectric Power of Metals* (Plenum, New York, 1976) (cit. on pp. 1, 7, 8, 9, 43, 56, 58, 64).
- [2] D. K. C. MacDonald, *Thermoelectricity – An Introduction to the Principles* (Dover, New York, 2006) (cit. on pp. 1, 8).
- [3] W. Thomson, «On the Electro-Dynamic Qualities of Metals:–Effects of Magnetization on the Electric Conductivity of Nickel and of Iron», *Proc. R. Soc. London* **8**, 546 (1856) (cit. on pp. 1, 3).
- [4] W. Thomson, «The Bakerian Lecture. – On the Electro-dynamic Qualities of Metals», *Philos. Trans. R. Soc. London* **146**, 649 (1856) (cit. on pp. 1, 3, 11).
- [5] L. L. Campbell, *Galvanomagnetic and Thermomagnetic Effects – The Hall and Allied Phenomena* (Longmans, Green and Co., London, 1923) (cit. on p. 1).
- [6] T. R. McGuire and R. I. Potter, «Anisotropic Magnetoresistance in Ferromagnetic 3d Alloys», *IEEE Trans. Magn.* **11**, 1018 (1975) (cit. on pp. 1, 4).
- [7] G. Binasch, P. Grünberg, F. Saurenbach, and W. Zinn, «Enhanced magnetoresistance in layered magnetic structures with antiferromagnetic interlayer exchange», *Phys. Rev. B* **39**, 4828 (1989) (cit. on p. 1).
- [8] J. Shi, K. Pettit, E. Kita, S. S. P. Parkin, R. Nakatani, and M. B. Salamon, «Field-dependent thermoelectric power and thermal conductivity in multilayered and granular giant magnetoresistive systems», *Phys. Rev. B* **54**, 15273 (1996) (cit. on pp. 1, 10, 11, 64).
- [9] K. Uchida, S. Takahashi, K. Harii, J. Ieda, W. Koshibae, K. Ando, S. Maekawa, and E. Saitoh, «Observation of the spin Seebeck effect», *Nature* **455**, 778 (2008) (cit. on p. 1).
- [10] A. Slachter, F. L. Bakker, J.-P. Adam, and B. J. van Wees, «Thermally driven spin injection from a ferromagnet into a non-magnetic metal», *Nat. Phys.* **6**, 879 (2010) (cit. on p. 1).

## Bibliography

- [11] G. E. W. Bauer, E. Saitoh, and B. J. van Wees, «Spin caloritronics», *Nat. Mater.* **11**, 391 (2012) (cit. on p. 1).
- [12] H. Adachi, K.-i. Uchida, E. Saitoh, and S. Maekawa, «Theory of the spin Seebeck effect», *Rep. Prog. Phys.* **76**, 036501 (2013) (cit. on p. 1).
- [13] E. H. Hall, «XVIII. On the “Rotational Coefficient” in nickel and cobalt», *Philos. Mag.* **12**, 157 (1881) (cit. on pp. 1, 6).
- [14] W. Nernst, «Ueber die electromotorischen Kräfte, welche durch den Magnetismus in von einem Wärmestrome durchflossenen Metallplatten geweckt werden», *Ann. Phys.* **267**, 760 (1887) (cit. on pp. 1, 11, 45).
- [15] S. R. Boona, R. C. Myers, and J. P. Heremans, «Spin caloritronics», *Energy Environ. Sci.* **7**, 885 (2014) (cit. on p. 1).
- [16] B. Carvello, C. Ducruet, B. Rodmacq, S. Auffret, E. Gautier, G. Gaudin, and B. Dieny, «Sizable room-temperature magnetoresistance in cobalt based magnetic tunnel junctions with out-of-plane anisotropy», *Appl. Phys. Lett.* **92**, 102508 (2008) (cit. on p. 2).
- [17] A. Kobs, S. Heße, W. Kreuzpaintner, G. Winkler, D. Lott, P. Weinberger, A. Schreyer, and H. P. Oepen, «Anisotropic Interface Magnetoresistance in Pt/Co/Pt Sandwiches», *Phys. Rev. Lett.* **106**, 217207 (2011) (cit. on pp. 2, 4, 29, 51, 67).
- [18] A. Kobs, S. Heße, H. P. Oepen, and P. Weinberger, «Anisotropic interface magnetoresistances in Pt(111)/Co<sub>n</sub>/Pt(111)», *Philos. Mag.* **92**, 2835 (2012) (cit. on pp. 2, 4, 67).
- [19] A. Kobs, A. Frauen, and H. P. Oepen, «Comment on ‘Hybrid magnetoresistance in the proximity of a ferromagnet’», *Phys. Rev. B* **90**, 016401 (2014) (cit. on pp. 2, 4, 29).
- [20] A. Kobs and H. P. Oepen, «Disentangling interface and bulk contributions to the anisotropic magnetoresistance in Pt/Co/Pt sandwiches», *Phys. Rev. B* **93**, 014426 (2016) (cit. on pp. 2, 4, 51, 53, 54, 67, 71).
- [21] N. F. Mott, «The Resistance and Thermoelectric Properties of the Transition Metals», *Proc. R. Soc. London, Ser. A* **156**, 368 (1936) (cit. on pp. 2, 8, 9).
- [22] G. N. Grannemann and L. Berger, «Magnon-drag Peltier effect in a Ni-Cu alloy», *Phys. Rev. B* **13**, 2072 (1976) (cit. on pp. 2, 10, 64).
- [23] F. Tsui, B. Chen, D. Barlett, R. Clarke, and C. Uher, «Scaling Behavior of Giant Magnetotransport Effects in Co/Cu Superlattices», *Phys. Rev. Lett.* **72**, 740 (1994) (cit. on pp. 2, 10).

- [24] J.-E. Wegrowe, Q. A. Nguyen, M. Al-Barki, J.-F. Dayen, T. L. Wade, and H.-J. Drouhin, «Anisotropic magnetothermopower: Contribution of interband relaxation», *Phys. Rev. B* **73**, 134422 (2006) (cit. on pp. 2, 10).
- [25] N. Liebing, S. Serrano-Guisan, K. Rott, G. Reiss, J. Langer, B. Ocker, and H. W. Schumacher, «Tunneling Magnetothermopower in Magnetic Tunnel Junction Nanopillars», *Phys. Rev. Lett.* **107**, 177201 (2011) (cit. on pp. 2, 10).
- [26] S. Blundell, *Magnetism in Condensed Matter* (Oxford University Press, Oxford, New York, 2012) (cit. on p. 3).
- [27] R. C. O’Handley, *Modern Magnetic Materials – Principles and Applications* (John Wiley, New York, 2000) (cit. on pp. 3, 19).
- [28] S. Chikazumi and C. D. Graham, *Physics of Ferromagnetism* (Oxford University Press, Oxford, New York, 2010) (cit. on p. 3).
- [29] A. Aharoni, *Introduction to the Theory of Ferromagnetism* (Oxford University Press, Oxford, New York, 2008) (cit. on p. 3).
- [30] M. Getzlaff, *Fundamentals of Magnetism* (Springer, Berlin, 2010) (cit. on p. 3).
- [31] J. Stöhr and H. C. Siegmann, *Magnetism – From Fundamentals to Nanoscale Dynamics* (Springer, Berlin, 2006) (cit. on p. 3).
- [32] C. M. Hurd, «Galvanomagnetic effects in anisotropic metals», *Adv. Phys.* **23**, 315 (1974) (cit. on pp. 3, 45, 58).
- [33] L. Onsager, «Reciprocal Relations in Irreversible Processes. I.», *Phys. Rev.* **37**, 405 (1931) (cit. on pp. 3, 5, 45).
- [34] L. Onsager, «Reciprocal Relations in Irreversible Processes. II.», *Phys. Rev.* **38**, 2265 (1931) (cit. on pp. 3, 5, 45).
- [35] J. Smit, «Magnetoresistance of ferromagnetic metals and alloys at low temperatures», *Physica* **17**, 612 (1951) (cit. on p. 4).
- [36] L. Berger, «Influence of spin-orbit interaction on the transport processes in ferromagnetic nickel alloys, in the presence of a degeneracy of the 3d band», *Physica* **30**, 1141 (1964) (cit. on p. 4).
- [37] R. I. Potter, «Magnetoresistance anisotropy in ferromagnetic NiCu alloys», *Phys. Rev. B* **10**, 4626 (1974) (cit. on p. 4).

## Bibliography

- [38] E. N. Mitchell, H. B. Haukaas, H. D. Bale, and J. B. Streeper, «Compositional and Thickness Dependence of the Ferromagnetic Anisotropy in Resistance of Iron-Nickel Films», *J. Appl. Phys.* **35**, 2604 (1964) (cit. on p. 4).
- [39] T. Miyazaki, T. Ajima, and F. Sato, «Dependence of magnetoresistance on thickness and substrate temperature for 82Ni-Fe alloy film», *J. Magn. Magn. Mater.* **81**, 86 (1989) (cit. on p. 4).
- [40] A. Kobs, *Magnetogalvanic effects in ferromagnets of reduced dimensions*, Ph.D. thesis, Universität Hamburg (2013) (cit. on pp. 4, 14, 15, 19, 20, 22, 23, 30, 51, 52, 54, 67).
- [41] J.-C. Lee, C.-H. Hsieh, C.-C. Chang, L.-W. Huang, L.-K. Lin, and S.-F. Lee, «Comparison of anisotropic interface magnetoresistance in Co/Pt and Co/Pd multilayers», *J. Appl. Phys.* **113**, 17C714 (2013) (cit. on pp. 4, 68).
- [42] Y. M. Lu, J. W. Cai, S. Y. Huang, D. Qu, B. F. Miao, and C. L. Chien, «Hybrid magnetoresistance in the proximity of a ferromagnet», *Phys. Rev. B* **87**, 220409 (2013) (cit. on pp. 4, 68).
- [43] Y. Kachlon, N. Kurzweil, and A. Sharoni, «Extracting magnetic anisotropy energies in Co/Pd multilayers via refinement analysis of the full magnetoresistance curves», *J. Appl. Phys.* **115**, 173911 (2014) (cit. on pp. 4, 68).
- [44] W. Gil, D. Görlitz, M. Horisberger, and J. Kötzler, «Magnetoresistance anisotropy of polycrystalline cobalt films: Geometrical-size and domain effects», *Phys. Rev. B* **72**, 134401 (2005) (cit. on p. 5).
- [45] T. T. Chen and V. A. Marsocci, «Transverse Magnetoresistivity Anisotropy Measurements and the Geometrical Size Effect in Nickel Thin Films», *J. Appl. Phys.* **43**, 1554 (1972) (cit. on p. 5).
- [46] B. Dieny, M. Li, S. H. Liao, C. Horng, and K. Ju, «Effect of interfacial specular electron reflection on the anisotropic magnetoresistance of magnetic thin films», *J. Appl. Phys.* **88**, 4140 (2000) (cit. on p. 5).
- [47] W. Döring, «Die Abhängigkeit des Widerstandes von Nickelkristallen von der Richtung der spontanen Magnetisierung», *Ann. Phys.* **424**, 259 (1938) (cit. on p. 5).
- [48] B. Raquet, M. Viret, E. Sondergard, O. Cespedes, and R. Mamy, «Electron-magnon scattering and magnetic resistivity in 3d ferromagnets», *Phys. Rev. B* **66**, 024433 (2002) (cit. on pp. 5, 29).
- [49] B. Raquet, M. Viret, P. Warin, E. Sondergard, and R. Mamy, «Negative high field magnetoresistance in 3d ferromagnets», *Physica B* **294**, 102 (2001) (cit. on p. 5).

- [50] E. H. Hall, «On a New Action of the Magnet on Electric Currents», *Amer. J. Math.* **2**, 287 (1879) (cit. on p. 5).
- [51] N. Nagaosa, J. Sinova, S. Onoda, A. H. MacDonald, and N. P. Ong, «Anomalous Hall effect», *Rev. Mod. Phys.* **82**, 1539 (2010) (cit. on pp. 6, 36).
- [52] J. Kötztler and W. Gil, «Anomalous Hall resistivity of cobalt films: Evidence for the intrinsic spin-orbit effect», *Phys. Rev. B* **72**, 060412 (2005) (cit. on pp. 6, 35).
- [53] A. C. Smith, J. F. Janak, and R. B. Adler, *Electronic conduction in solids* (McGraw-Hill, New York, 1967) (cit. on p. 7).
- [54] C. L. Foiles, «Thermopower of pure metals and dilute alloys», in *Landolt-Börnstein, New Series, Group III Condensed Matter – Metals: Electronic Transport Phenomena*, Vol. 15b, edited by K.-H. Hellwege and J. L. Olsen (Springer, Berlin, 1985) (cit. on pp. 7, 56).
- [55] R. D. Barnard, *Thermoelectricity in Metals and Alloys* (Taylor & Francis, London, 1972) (cit. on pp. 7, 56).
- [56] R. Pelster, R. Pieper, and I. Hüttl, «Thermospannungen – viel genutzt und fast immer falsch erklärt!», *PhyDid A* **1**, 10 (2005) (cit. on p. 8).
- [57] S. Heinze, *Thermoelectric properties of oxide heterostructures*, Ph.D. thesis, Universität Stuttgart (2013) (cit. on p. 8).
- [58] N. F. Mott and H. Jones, *The Theory of the properties of metals and alloys* (Dover, New York, 1958) (cit. on p. 8).
- [59] M. Jonson and G. D. Mahan, «Mott’s formula for the thermopower and the Wiedemann-Franz law», *Phys. Rev. B* **21**, 4223 (1980) (cit. on p. 8).
- [60] A. V. Gold, D. K. C. Macdonald, W. B. Pearson, and I. M. Templeton, «The Thermoelectric Power of Pure Copper», *Philos. Mag.* **5**, 765 (1960) (cit. on p. 9).
- [61] J. P. Small, K. M. Perez, and P. Kim, «Modulation of Thermoelectric Power of Individual Carbon Nanotubes», *Phys. Rev. Lett.* **91**, 256801 (2003) (cit. on p. 9).
- [62] Y. M. Zuev, W. Chang, and P. Kim, «Thermoelectric and Magnetothermoelectric Transport Measurements of Graphene», *Phys. Rev. Lett.* **102**, 096807 (2009) (cit. on p. 9).

## Bibliography

- [63] A. D. Avery, R. Sultan, D. Bassett, D. Wei, and B. L. Zink, «Thermopower and resistivity in ferromagnetic thin films near room temperature», *Phys. Rev. B* **83**, 100401 (2011) (cit. on pp. 9, 58, 64).
- [64] M. Cutler and N. F. Mott, «Observation of Anderson Localization in an Electron Gas», *Phys. Rev.* **181**, 1336 (1969) (cit. on p. 9).
- [65] M. Stearns, «Fe, Co, Ni», in *Landolt-Börnstein, New Series, Group III Condensed Matter – Magnetic Properties of Metals*, Vol. 19a, edited by H. P. J. Wijn (Springer, Berlin, 1986) (cit. on p. 9).
- [66] A. D. Avery, M. R. Pufall, and B. L. Zink, «Determining the planar Nernst effect from magnetic-field-dependent thermopower and resistance in nickel and permalloy thin films», *Phys. Rev. B* **86**, 184408 (2012) (cit. on pp. 10, 32, 34).
- [67] T. Böhnert, V. Vega, A.-K. Michel, V. M. Prida, and K. Nielsch, «Magnetothermopower and magnetoresistance of single Co-Ni alloy nanowires», *Appl. Phys. Lett.* **103**, 092407 (2013) (cit. on p. 10).
- [68] M. V. Costache, G. Bridoux, I. Neumann, and S. O. Valenzuela, «Magnon-drag thermopile», *Nat. Mater.* **11**, 199 (2012) (cit. on p. 10).
- [69] H. Sato, H. Henmi, Y. Kobayashi, Y. Aoki, H. Yamamoto, T. Shinjo, and V. Sechovsky, «Giant magnetoresistance related transport properties in multilayers and bulk materials (invited)», *J. Appl. Phys.* **76**, 6919 (1994) (cit. on p. 10).
- [70] S. Serrano-Guisan, G. di Domenicantonio, M. Abid, J.-P. Abid, M. Hillenkamp, L. Gravier, J.-P. Ansermet, and C. Félix, «Enhanced magnetic field sensitivity of spin-dependent transport in cluster-assembled metallic nanostructures», *Nat. Mater.* **5**, 730 (2006) (cit. on p. 10).
- [71] T. Miyasato, N. Abe, T. Fujii, A. Asamitsu, S. Onoda, Y. Onose, N. Nagaosa, and Y. Tokura, «Crossover Behavior of the Anomalous Hall Effect and Anomalous Nernst Effect in Itinerant Ferromagnets», *Phys. Rev. Lett.* **99**, 086602 (2007) (cit. on p. 11).
- [72] Y. Pu, D. Chiba, F. Matsukura, H. Ohno, and J. Shi, «Mott Relation for Anomalous Hall and Nernst Effects in  $\text{Ga}_{1-x}\text{Mn}_x\text{As}$  Ferromagnetic Semiconductors», *Phys. Rev. Lett.* **101**, 117208 (2008) (cit. on p. 11).
- [73] R. Ramos, M. H. Aguirre, A. Anadón, J. Blasco, I. Lucas, K. Uchida, P. A. Algarabel, L. Morellón, E. Saitoh, and M. R. Ibarra, «Anomalous Nernst effect of  $\text{Fe}_3\text{O}_4$  single crystal», *Phys. Rev. B* **90**, 054422 (2014) (cit. on p. 11).

- [74] J. Shi, E. Kita, L. Xing, and M. B. Salamon, «Magnetothermopower of a  $\text{Ag}_{80}\text{Co}_{20}$  granular system», *Phys. Rev. B* **48**, 16119 (1993) (cit. on pp. 11, 64).
- [75] L. van der Tempel, G. P. Melis, and T. C. Brandsma, «Thermal Conductivity of a Glass: I. Measurement by the Glass-Metal Contact», *Glass Phys. Chem.* **26**, 606 (2000) (cit. on p. 14).
- [76] H. Stillrich, C. Menk, R. Frömter, and H. P. Oepen, «Magnetic anisotropy and spin reorientation in Co/Pt multilayers: Influence of preparation», *J. Magn. Magn. Mater.* **322**, 1353 (2010) (cit. on p. 14).
- [77] G. Winkler, A. Kobs, A. Chuvilin, D. Lott, A. Schreyer, and H. P. Oepen, «On the variation of magnetic anisotropy in Co/Pt(111) on silicon oxide», *J. Appl. Phys.* **117**, 105306 (2015) (cit. on p. 14).
- [78] H. Stillrich, *Magnetische Nanostrukturen basierend auf Co/Pt-Multilagen, hergestellt mittels selbstorganisierter Masken aus Blockcopolymer-Micellen*, Ph.D. thesis, Universität Hamburg (2008) (cit. on p. 14).
- [79] G. Winkler, *Korrelation zwischen strukturellen und magnetogalvanischen Eigenschaften von Pt/Co/Pt- und Pd/Co/Pd-Schichtsystemen*, Ph.D. thesis, Universität Hamburg (2015) (cit. on pp. 14, 19).
- [80] C. Kittel, *Einführung in die Festkörperphysik* (Oldenbourg, München, 1996) (cit. on p. 19).
- [81] L. Néel, «Anisotropie magnétique superficielle et surstructures d'orientation», *J. Phys. Radium* **15**, 225 (1954) (cit. on p. 19).
- [82] S. Heße, *Magnetotransport in Co/Pt-Schichtsystemen und Charakterisierung einzelner Co/Pt-Nanoteilchen*, Ph.D. thesis, Universität Hamburg (2014) (cit. on pp. 19, 51, 52).
- [83] J. H. Van Der Merwe, «Crystal Interfaces. Part II. Finite Overgrowths», *J. Appl. Phys.* **34**, 123 (1963) (cit. on p. 22).
- [84] D. Sander, «The correlation between mechanical stress and magnetic anisotropy in ultrathin films», *Rep. Prog. Phys.* **62**, 809 (1999) (cit. on p. 22).
- [85] D. Sander, «The magnetic anisotropy and spin reorientation of nanostructures and nanoscale films», *J. Phys.: Condens. Matter* **16**, R603 (2004) (cit. on p. 22).

## Bibliography

- [86] C. Reale, «Thickness dependence of the thermoelectric power in palladium and platinum films», *J. Less Common Met.* **18**, 167 (1969) (cit. on pp. 27, 43).
- [87] V. D. Nguyen, L. Vila, P. Laczkowski, A. Marty, T. Faivre, and J. P. Attané, «Detection of Domain-Wall Position and Magnetization Reversal in Nanostructures Using the Magnon Contribution to the Resistivity», *Phys. Rev. Lett.* **107**, 136605 (2011) (cit. on p. 29).
- [88] M. Hille, *Magnetotransport-Untersuchungen in Co/Pt-Drähten unter Berücksichtigung der Domänenstruktur*, Ph.D. thesis, Universität Hamburg (2013) (cit. on pp. 29, 65).
- [89] C. Erdmann, *Magnetoresistance and magnetothermoelectric power of Pt/Co/Pt layered structures with different Co thicknesses*, Master's thesis, Universität Hamburg (2017) (cit. on pp. 30, 53, 54, 58, 59, 60, 64, 71).
- [90] A. Frauen, A. Kobs, T. Böhnert, A.-K. Michel, G. Winkler, K. Nielsch, and H. P. Oepen, «Magnetothermoelectric power in Co/Pt layered structures: Interface versus bulk contributions», *Phys. Rev. B* **92**, 140402(R) (2015) (cit. on pp. 30, 32, 44, 45, 58, 61, 67, 68, 71).
- [91] C. Goldberg and R. E. Davis, «New Galvanomagnetic Effect», *Phys. Rev.* **94**, 1121 (1954) (cit. on p. 34).
- [92] M. K. Koch, «Zum Problem der galvanomagnetischen Effekte in Ferromagneticis», *Z. Naturforschg. A* **10**, 496 (1955) (cit. on p. 34).
- [93] V. D. Ky, «Planar Hall and Nernst Effect in Ferromagnetic Metals», *Phys. Stat. Sol. B* **22**, 729 (1967) (cit. on p. 34).
- [94] Y. Pu, E. Johnston-Halperin, D. D. Awschalom, and J. Shi, «Anisotropic Thermopower and Planar Nernst Effect in  $\text{Ga}_{1-x}\text{Mn}_x\text{As}$  Ferromagnetic Semiconductors», *Phys. Rev. Lett.* **97**, 036601 (2006) (cit. on p. 34).
- [95] S. Foner and E. M. Pugh, «Hall Effects of the Cobalt Nickel Alloys and of Armco Iron», *Phys. Rev.* **91**, 20 (1953) (cit. on p. 35).
- [96] W. Betteridge, «The properties of metallic cobalt», *Prog. Mater Sci.* **24**, 51 (1980) (cit. on p. 35).
- [97] J.-P. Jan, «Galvanomagnetic and Thermomagnetic Effects in Metals», *Solid State Phys.* **5**, 1 (1957) (cit. on p. 35).
- [98] O. A. Panchenko, P. P. Lutsishin, and Y. G. Ptushinskii, «Galvanomagnetic Effects in Thin Films of Some Transition Metals», *Sov. Phys. - JETP* **29**, 76 (1969) (cit. on p. 35).

- [99] S. Zhang, «Extraordinary Hall effect in magnetic multilayers», *Phys. Rev. B* **51**, 3632 (1995) (cit. on p. 35).
- [100] E. M. Pugh, «Hall Effect and the Magnetic Properties of Some Ferromagnetic Materials», *Phys. Rev.* **36**, 1503 (1930) (cit. on p. 36).
- [101] P. L. Kapitza, «Heat Transfer and Superfluidity of Helium II», *Phys. Rev.* **60**, 354 (1941) (cit. on p. 39).
- [102] N. Cusack and P. Kendall, «The Absolute Scale of Thermoelectric Power at High Temperature», *Proc. Phys. Soc.* **72**, 898 (1958) (cit. on p. 43).
- [103] M. J. Laubitz and T. Matsumura, «Transport Properties of the Ferromagnetic Metals. I. Cobalt», *Can. J. Phys.* **51**, 1247 (1973) (cit. on p. 43).
- [104] R. B. Roberts, «The absolute scale of thermoelectricity II», *Philos. Mag. B* **43**, 1125 (1981) (cit. on p. 43).
- [105] S. S.-L. Zhang and S. Zhang, «Angular dependence of anisotropic magnetoresistance in magnetic systems», *J. Appl. Phys.* **115**, 17C703 (2014) (cit. on p. 54).
- [106] A. Raoufi and S. Araj, «Effects of magnetic field and tensile stress on the electrical resistivity of some amorphous ferromagnets», *Phys. Stat. Sol. A* **95**, 193 (1986) (cit. on p. 54).
- [107] S. Yang, L. Feng, D. Zhang, W. Huang, S. Dong, J. Wang, L. Zou, X. Li, and C. Nan, «Magnetically correlated anisotropic resistive switching manipulated by electric field in Co/PMN-PT heterostructures», *J. Alloys Compd.* **646**, 472 (2015) (cit. on p. 54).
- [108] J. Recker, *Einfluss von Magnonen auf den spezifischen Widerstand und den Seebeck-Koeffizienten von Pt/Co/Pt-Schichtsystemen*, Master's thesis, Universität Hamburg (2016) (cit. on p. 64).
- [109] D. Wang and J. Shi, «Effect of charged impurities on the thermoelectric power of graphene near the Dirac point», *Phys. Rev. B* **83**, 113403 (2011) (cit. on p. 64).
- [110] F. Ghahari, H.-Y. Xie, T. Taniguchi, K. Watanabe, M. S. Foster, and P. Kim, «Enhanced Thermoelectric Power in Graphene: Violation of the Mott Relation by Inelastic Scattering», *Phys. Rev. Lett.* **116**, 136802 (2016) (cit. on p. 64).
- [111] M. Bailyn, «Maximum Variational Principle for Conduction Problems in a Magnetic Field, and the Theory of Magnon Drag», *Phys. Rev.* **126**, 2040 (1962) (cit. on p. 64).

## Bibliography

- [112] K. Behnia, *Fundamentals of Thermoelectricity* (Oxford University Press, Oxford, United Kingdom, 2015) (cit. on p. 64).
- [113] F. J. Blatt, D. J. Flood, V. Rowe, P. A. Schroeder, and J. E. Cox, «Magnon-Drift Thermopower in Iron», *Phys. Rev. Lett.* **18**, 395 (1967) (cit. on p. 64).
- [114] F. J. Blatt, «Magnetic Field Dependence of the Thermoelectric Power of Iron», *Can. J. Phys.* **50**, 2836 (1972) (cit. on p. 64).
- [115] B. G. Park, J. Wunderlich, D. A. Williams, S. J. Joo, K. Y. Jung, K. H. Shin, K. Olejník, A. B. Shick, and T. Jungwirth, «Tunneling Anisotropic Magnetoresistance in Multilayer-(Co/Pt)/AlO<sub>x</sub>/Pt Structures», *Phys. Rev. Lett.* **100**, 087204 (2008) (cit. on p. 68).
- [116] V. Popescu and P. Kratzer, «Large Seebeck magnetic anisotropy in thin Co films embedded in Cu determined by *ab initio* investigations», *Phys. Rev. B* **88**, 104425 (2013) (cit. on p. 68).
- [117] J. Borge, C. Gorini, and R. Raimondi, «Spin thermoelectrics in a disordered Fermi gas», *Phys. Rev. B* **87**, 085309 (2013) (cit. on p. 68).

# Publications

## Articles

A. Neumann, A. Frauen, J. Vollmers, A. Meyer, and H. P. Oepen, «Structure-induced spin reorientation in magnetic nanostructures», *Phys. Rev. B* **94**, 094430 (2016).

R. Frömter, F. Kloodt, S. Rößler, A. Frauen, P. Staeck, D. R. Cavicchia, L. Bocklage, V. Röbisch, E. Quandt, and H. P. Oepen, «Time-resolved scanning electron microscopy with polarization analysis», *Appl. Phys. Lett.* **108**, 142401 (2016).

A. Frauen, A. Kobs, T. Böhnert, A.-K. Michel, G. Winkler, K. Nielsch, and H. P. Oepen, «Magnetothermoelectric power in Co/Pt layered structures: Interface versus bulk contributions», *Phys. Rev. B* **92**, 140402(R) (2015).

A. Kobs, A. Frauen, and H. P. Oepen, «Comment on ‘Hybrid magnetoresistance in the proximity of a ferromagnet’», *Phys. Rev. B* **90**, 016401 (2014).

A. Neumann, C. Thönnißen, A. Frauen, S. Heße, A. Meyer, and H. P. Oepen, «Probing the Magnetic Behavior of Single Nanodots», *Nano Lett.* **13**, 2199 (2013).

M. Hille, A. Frauen, B. Beyersdorff, A. Kobs, S. Heße, R. Frömter, and H. P. Oepen, «Direct method for measuring the canting angle of magnetization», *J. Appl. Phys.* **113**, 023902 (2013).

## Conference Contributions

A. Frauen, A. Kobs, T. Böhnert, A.-K. Michel, G. Winkler, K. Nielsch, and H. P. Oepen, «Anisotropic interface contributions to the magnetothermoelectric power (MTEP) in Co/Pt layered structures», Talk at the 22nd International Colloquium on Magnetic Films and Surfaces (ICMFS) 2015, Cracow (Poland)

A. Kobs, A. Frauen, G. Winkler, A. Farhadi, S. Heße, and H. P. Oepen, «Anisotropic Interface Magnetoresistance (AIMR) of all-metallic layered structures», Talk at the 59th Annual Conference on Magnetism and Magnetic Materials (MMM) 2014, Honolulu (USA).

## Publications

A. Frauen, A. Kobs, T. Böhnert, A.-K. Michel, G. Winkler, K. Nielsch, and H. P. Oepen, «Anisotropic interface contributions to the magnetothermoelectric power (MTEP) in Co/Pt layered structures», Talk at the 59th Annual Conference on Magnetism and Magnetic Materials (MMM) 2014, Honolulu (USA).

A. Neumann, D. Altwein, C. Thönnißen, A. Frauen, R. Wieser, A. Berger, A. Meyer, E. Vedmedenko, and H. P. Oepen, «Probing the Magnetic Behavior of Single Nanodots», Talk at the 59th Annual Conference on Magnetism and Magnetic Materials (MMM) 2014, Honolulu (USA).

A. Neumann, A. Frauen, J. Vollmers, A. Meyer, and H. P. Oepen, «Structuring induced spin reorientation in magnetic nanostructures», Poster at the 59th Annual Conference on Magnetism and Magnetic Materials (MMM) 2014, Honolulu (USA).

A. Kobs, G. Winkler, A. Frauen, A. Farhadi, P. Staeck, S. Heße, and H. P. Oepen, «Anisotropic Interface Magnetoresistance (AIMR) of all-metallic layered structures», Talk at the IEEE International Magnetism Conference (INTERMAG) 2014, Dresden (Germany).

A. Neumann, D. Altwein, C. Thönnißen, A. Frauen, R. Wieser, A. Berger, A. Meyer, E. Vedmedenko, and H. P. Oepen, «Probing the Magnetic Behavior of Single Nanodots», Talk at the IEEE International Magnetism Conference (INTERMAG) 2014, Dresden (Germany).

A. Frauen, T. Böhnert, A. Kobs, A. Burgardt, G. Winkler, K. Nielsch, and H. P. Oepen, «Anisotropic magnetothermopower and magnetotransport effects in Pt/Co/Pt layered structures», Poster at the 58th Annual Conference on Magnetism and Magnetic Materials (MMM) 2013, Denver (USA).

A. Neumann, D. Altwein, C. Thönnißen, A. Frauen, R. Wieser, A. Berger, A. Meyer, E. Vedmedenko, and H. P. Oepen, «Probing the Magnetic Behavior of Single Nanodots», Talk at the 58th Annual Conference on Magnetism and Magnetic Materials (MMM) 2013, Denver (USA).

M. Hille, A. Frauen, B. Beyersdorff, A. Kobs, S. Heße, R. Frömter, and H. P. Oepen, «Determining the canting angle of magnetization via magnetoresistance measurements», Talk at the Spring Meeting of the German Physical Society (DPG) 2012, Berlin (Germany).

## Danksagung

Ich möchte mich herzlich bei allen Personen bedanken, die durch ihre Unterstützung die Anfertigung dieser Arbeit ermöglicht haben. Insbesondere gilt dies für den Betreuer meiner Doktorarbeit, Herrn Prof. Dr. Hans Peter Oepen, der mit seiner fachlichen Expertise und fundierten Ratschlägen bei auftretenden Herausforderungen in den letzten Jahren stets zur Seite stand. Hervorheben möchte ich auch Herrn Prof. Dr. Robert H. Blick, der freundlicherweise das Zweitgutachten dieser Arbeit übernimmt. Ganz herzlicher Dank gilt Dr. André Kobs. Ohne seine unermüdliche Unterstützung und sein großes wissenschaftliches Interesse wären viele Fragestellungen ungelöst geblieben. Außerdem konnte ich ihn als sehr angenehmen Arbeitskollegen kennenlernen. Dies gilt auch für die anderen Mitglieder der Gruppe G, bei denen ich mich für die Zusammenarbeit bedanke. Meinen Freunden aus der Studienzeit möchte ich für die schöne Zeit danken, insbesondere meinem Lieblingsmitbewohner Christoph Hübner, sowie Jens Ehlermann, Christian Heusinger, Theo Gerhardt und Cornelius Bausch. Besonderer Dank gilt meiner Familie für die Unterstützung während des Studiums.



## Eidesstattliche Versicherung / Declaration on oath

Hiermit versichere ich an Eides statt, die vorliegende Dissertationsschrift selbst verfasst und keine anderen als die angegebenen Hilfsmittel und Quellen benutzt zu haben. Die eingereichte schriftliche Fassung entspricht der auf dem elektronischen Speichermedium. Die Dissertation wurde in der vorgelegten oder einer ähnlichen Form nicht schon einmal in einem früheren Promotionsverfahren angenommen oder als ungenügend beurteilt.

Hamburg, im Juni 2017